8-2016

Investigation of cellular microenvironments and heterogeneity with biodynamic imaging

Daniel Alexander Merrill
Purdue University

PURDUE UNIVERSITY
GRADUATE SCHOOL
Thesis/Dissertation Acceptance

This is to certify that the thesis/dissertation prepared

By Daniel A. Merrill

Entitled
INVESTIGATION OF CELLULAR MICROENVIRONMENTS AND HETEROGENEITY WITH BIODYNAMIC IMAGING

For the degree of Doctor of Philosophy

Is approved by the final examining committee:

David D. Nolte
Chair

Gabor A. Csathy

Luis M. Kruczenski

Sergei Savikhin

To the best of my knowledge and as understood by the student in the Thesis/Dissertation Agreement, Publication Delay, and Certification Disclaimer (Graduate School Form 32), this thesis/dissertation adheres to the provisions of Purdue University's "Policy of Integrity in Research" and the use of copyright material.

Approved by Major Professor(s): David D. Nolte

Approved by: John P. Finley   7/25/2016
             Head of the Departmental Graduate Program   Date

INVESTIGATION OF CELLULAR MICROENVIRONMENTS AND

HETEROGENEITY WITH BIODYNAMIC IMAGING

A Dissertation

Submitted to the Faculty

of

Purdue University

by

Daniel A. Merrill

In Partial Fulfillment of the

Requirements for the Degree

of

Doctor of Philosophy

August 2016

Purdue University

West Lafayette, Indiana

To my wife, Lilon,

and to my daughters, Janae, Cora, Ingrid, Brenna, and Sylvia.

They believed I could be a scientist.

ACKNOWLEDGEMENTS

reminded me to eat when I had forgotten; who assured me I could finish when I was too tired to continue. Without her continual and unconditional love, I would not be the man I am today. She is the gift I will always cherish.

TABLE OF CONTENTS

LIST OF TABLES

LIST OF FIGURES

ABSTRACT

Merrill, Daniel A. Ph.D., Purdue University, August 2016. Investigation of Cellular Microenvironments and Heterogeneity with Biodynamic Imaging. Major Professor: David D. Nolte.

Imaging of biological tissue in a relevant environment is critical to accurately assessing the effectiveness of chemotherapeutic agents in combatting cancer. Though many three-dimensional (3D) culture models exist, conventional *in vitro* assays continue to use two-dimensional (2D) cultures because of the difficulty in imaging through deep tissue. 3D tomographic imaging techniques exist and are being used in the development of 3D efficacy assays. However, most of these assays look at therapy endpoint (dead or living cancer cell count) and do not capture the dynamics of tissue response.

Biodynamic imaging (BDI) is a 3D tomographic imaging and assay technique that uses the dynamics of scattered coherent light, or speckle, to measure dynamic response of tissue to perturbations. Dynamic measurements allow BDI to not only assess overall efficacy, but to also measure phenotypic changes in cancer tissue as it responds to therapy. Because BDI captures the phenotypic response of tissue, it naturally accounts for genetic and microenvironmetal factors, and shows promise as an accurate predictor of *in vivo* chemotherapeutic response.

This thesis presents the development of BDI into a predictive assay for assisting in chemotherapy selection. It shows how microenvironmental factors alter BDI response measurements. It reports how different BDI biomarkers can accurately assess sensitivity to platinum treatment in xenograpft models of ovarian cancer. Changes in sensitivity during metastasis are observed, and a method for addressing sample variability and heterogeneity is presented. A predictive model for chemotherapeutic selection is developed and applied retrospectively to primary esophageal cancer. Finally, a new imaging modality called tissue dynamic spectroscopic imaging (TDSI) is presented, which is capable of directly assessing spatial functional patterns in patient samples.

CHAPTER 1. BYODYNAMIC IMAGING (BDI)

1.1   Introduction

Biodynamic imaging is a full-frame, coherent imaging and drug response assay technique that uses biological motion as both contrast agent and information source. It achieves a high imaging rate without the need for biological stains or other labels, preserving the natural chemical and physiological state of imaged tissue. Biodynamic imaging has been used to study the effect of chemotherapeutics on *ex vivo* and *in vitro* cancer tumor models [1-3], the viability of oocytes for artificial insemination [4, 5], and is currently developing predictive methods for assisting in cancer patient chemotherapy selection [6].

Biodynamic imaging currently has three modes: optical coherence imaging (OCI), motility contrast imaging (MCI), and tissue dynamics spectroscopy (TDS). Biodynamic imaging begins with optical coherence imaging (OCI) [7], a full-frame, *en face* optical coherence tomographic technique with important similarities to optical coherence tomography (OCT) [8-12]. Motility contrast imaging (MCI) [13] uses intensity fluctuations in the OCI image as the contrast agent of an imaged tissue target. These intensity fluctuations arise due to dynamic changes in the local index of refraction of the target volume. Thus, MCI generates a representation of the motile activity of the target within the imaged volume. Tissue dynamics spectroscopy (TDS) [14] calculates the

spectral power of the intensity fluctuations of the OCI image. The shape of the resulting power spectrum characterizes the motion present within the imaged volume and changes with changing tissue behavior. Thus TDS measures the response behavior of tissue to perturbations, such as chemotherapeutics.

This thesis presents the development of BDI toward being a clinically relevant predictive assay for chemotherapeutic therapy selection. CHAPTER 2 reports a study of how changes in the cellular microenvironment affect BDI response measurements and shows distinct differences in behavior between 2D cell culture and 3D tissue environments. It presents a 3D tissue model that mimics 2D culture response and shows that this model will transition into the full 3D culture response. An assay of ovarian cancer sensitivity to platinum therapies using BDI is presented in CHAPTER 3, while CHAPTER 4 looks at how metastasis alters that sensitivity. This is the first application of BDI to *in vivo* and *ex vivo* chemotherapeutic response assessment. BDI shows clear differences in *ex vivo* response between tumor biopsies grown from sensitive and insensitive ovarian cancer cell lines. A method for assessing *in vivo* response using *ex vivo* re-exposure is discussed, and a method for predicting patient response to chemotherapy is developed using BDI measurement biomarkers.

CHAPTER 5 presents the development of a fourth BDI mode: tissue dynamics spectroscopic imaging (TDSI), which combines the biodynamic measurements of OCI, MCI, and TDS as contrast agent to generate a false color image of the spatially heterogeneous behavior of a tissue sample, including response to chemotherapeutics. TDSI shows regional differences in sample behavior characteristic of heterogeneous

cancer tissue that are not apparent in traditional BDI analysis. Such heterogeneous response to chemotherapeutics has important implications determining the cause of multi-drug resistance and patient relapse.

1.2 Cellular dynamics and 3D tissue

Imaging of live tissue in a three-dimensional (3D) environment is of critical importance to biophysical science and especially to the study and treatment of cancer. Several 3D tumor models have been developed, including *in vitro* multicellular tumor spheroid models [15-18] and murine xenografts. However, the majority of chemotherapeutic efficacy assays continue to use two-dimensional (2D) culture models. This is because photon diffusion makes direct optical imaging through highly scattering media, such as tumor tissue, difficult and limits the depth resolution of traditional microscopy.

Cells have a typical size of 5-20 μm, which is much larger than the wavelength of near-infrared light. In this regime, ray optics dominates and cells act as tiny lenses. Stacked into tissue structures, these lenses generate a "showerglass" effect due to optical aberrations that limits resolution as imaging depth increases. Furthermore, the eukaryotic cell is a heterogeneous body containing many different structures with different refractive indices. This causes significant scattering of light as it propagates through tissue.

Eukaryotic cell structure can be separated into different regions. Outside the cell is the extracellular matrix, a region composed of collagen proteins and other molecules used by to organize cells into tissue. The cell membrane surrounds the interior of the cell. It is transfixed by different components through which the cell senses changes in the

extracellular matrix, communicates with other cells via cell-cell contacts, and takes in nutrients and expels waste. The cytoskeleton, made of microtubules, actin filaments, and stress fibers, is a flexible structure with high tensile strength that gives the cell dynamic rigidity. The cytoplasm fills the interstices of the cytoskeleton and is made up of cellular organelles, the largest of which, the nucleus, exhibits both geometric optic and Mie scattering behaviors [19]. Other organelles important to the study of tissue imaging are mitochondria (typical size: 200 nm to 5 μm), endosomes and exosomes. For these smaller organelles, scattering dominates optical interaction.

Cells and organelles are in constant motion. Mitosis and other processes change cell shape and cause undulations in the cell membrane. The common characteristic frequency of these undulations is in the range of 0.01 Hz to 0.1 Hz [20, 21]. Cytoskeletal components are in dynamic equilibrium, constantly being built and dismantled. Organelles driven by molecular motors travel at speeds in the range of several microns per second [22-25]. The various cellular components create dynamically shifting scattering interfaces.

1.3   Dynamic Light Scattering

When tissue is illuminated with a coherent source, scattering interactions lead to coherent noise, or speckle. Speckle arises due to interference between multiple waves scattered from spatially distributed variations in the refractive index of the illuminated target [26]. In biological targets, such refractive index variations come from different

cellular and tissue components. These components are in motion and generate time-varying speckle patterns through dynamic light scattering. This dynamic speckle is used by BDI to assess tissue health and response to perturbations.

Dynamic light scattering is a well-established technique for investigating biological systems, and has been used to study motions of the cell and nucleus [27, 28]. Dynamic light scattering is appropriate for optical systems in the dilute limit where single scattering interactions dominate. Diffusing wave spectroscopy (DWS), first proposed by Pine, *et al.* in 1988 [29], extends dynamic light scattering to optically dense scattering regimes by using the diffusion approximation to treat photon scattering as random walks [30, 31].

Dynamic light scattering is caused by the change in the optical phase of the scattered light as the particle moves. For instance, consider the incident light scattering off a moving particle illustrated in Figure 1.1 [26].
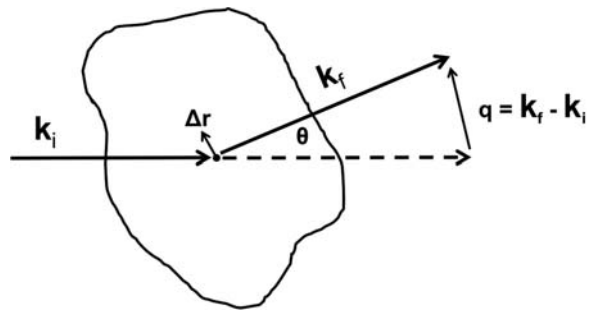
Figure 1.1. Illustration of momentum transfer during scattering events.

The light field scattered from a single moving particle is

$$E(t) = E_s \exp\left(-i\left(\mathbf{k}_f - \mathbf{k}_i\right) \cdot \mathbf{r}(t)\right) \qquad 1.1$$

As the position $r(t)$ of the particle changes, the phase of the scattered light changes. The difference in phase from one position to the next is

$$\begin{aligned}
\Delta\phi &= -\left(\mathbf{k}_f - \mathbf{k}_i\right) \cdot \left(\mathbf{r}(t_2) - \mathbf{r}(t_1)\right) \\
&= -\left(\mathbf{k}_f - \mathbf{k}_i\right) \cdot \Delta\mathbf{r} \\
&= -\mathbf{q} \cdot \Delta\mathbf{r}
\end{aligned} \qquad 1.2$$

where $\mathbf{q} = \left(\mathbf{k}_f - \mathbf{k}_i\right)$ is the scattering vector. The direction of the initial k-vector defines $\theta = 0$, and the magnitude of q for a scattering angle θ is

$$q = 2k\sin\frac{\theta}{2} = k\sqrt{2\left(1 - \cos\theta\right)} \qquad 1.3$$

Field autocorrelation is obtained by taking an ensemble average over scattered fields, or by integrating over all time. (Ensemble averages and time averages are equivalent under stationary statistics.) The stochastic sum is evaluated using a probability distribution as

$$\left\langle E^*(0)E(t)\right\rangle = \sum_n P\left(\Delta x_n(t)\right)E^*(0)E(t) \qquad 1.4$$

where $P\left(\Delta x_i(t)\right)$ is the probability functional of the displacement Δx. The autocorrelation is

$$\left\langle E^*(0)E(t)\right\rangle = E_0^2 + \sum_{n=1}^{N} E_n^2 P\left(\Delta x_n(t)\right)\exp\left(-iq\Delta x_n(t)\right) \qquad 1.5$$

and the stochastic sum is equivalent to an integral over the probability distribution

$$
\begin{aligned}
\left\langle E^*(0)E(t)\right\rangle &= E_0^2 + NI_s \int_{-\infty}^{\infty} P(\Delta x)\exp(-iq\Delta x) \\
&= I_0 + NI_s\, FT\left(P(\Delta x)\right)
\end{aligned}
$$

1.6

where the autocorrelation is proportional to the Fourier transform of the probability functional. The physical process, such as diffusion or drift or active transport, determines this probability functional. Different types of motion have different probability functionals. For diffusion, the probability functional is

$$
P_D\left(\Delta x_i(t)\right) = \frac{1}{\sqrt{4\pi Dt}}\exp\left(-\left(\Delta x_i(t)\right)^2/(4Dt)\right) = \frac{1}{\sqrt{2\pi\Delta x_{rms}^2}}\exp\left(-\left(\Delta x_i(t)\right)^2/2\left(\Delta x_{rms}^2\right)\right)
$$

1.7

which gives the diffusion autocorrelation function

$$
A_D^E(\tau) = \left\langle E^*(t)E(t+\tau)\right\rangle - I_0 = NI_s \exp\left(-q^2 D\tau\right)
$$

1.8

A one-dimensional random walk can be described as the sum of uncorrelated steps X_i

$$
Z = \sum_{i=1}^{N} X_i
$$

1.9

where N is the number of steps, X_i is a Gaussian distributed set of random steps, and Z is evaluated as statistical ensembles [4]. Active transport is defined by velocity distributions and by persistence times (the time of unidirectional free runs). If the velocity distribution is Gaussian, and the mean free run time (persistence time) distribution is exponential, then the rms step size is given by

$$
\begin{aligned}
X_i^2 &= A\int_{-\infty}^{\infty} v^2 \exp\left(-v^2/2v_0^2\right)dv \int_0^{\infty} t^2 \exp(-t/\tau)dt \\
&= 2v_0^2\tau^2
\end{aligned}
$$

1.10

where it is assumed that the mean speed is zero, with a standard deviation given by the

characteristic speed v_0 with a characteristic persistence time τ. The expectation of the

squared displacement of the random walk is then

$$E\left[Z^2\right] = NX_i^2 = 2Nv_0^2\tau^2 \qquad 1.11$$

The mean number of steps taken in a measurement time t is given by $N = t/\tau$, which

yields

$$\begin{aligned} E\left[Z^2\right] &= 2Nv_0^2\tau t \\ &= 2Dt \end{aligned} \qquad 1.12$$

where the equivalent diffusion coefficient of the actively driven random walk is defined

as

$$D = v_o^2\tau \qquad 1.13$$

The holographic fringes and the dynamic speckle set the resolution of the speckle

image. Nyquist theory predicts that two pixels are required to fully resolve each

interference fringe and two fringes resolve each speckle. In practice, however, it is more

convenient to use the "Rule of 9" with three fringes per speckle and 3 pixels per fringe.

The holographic fringe spacing is set by the angle θ between the beam axis of the off-

axis reference beam and the optic axis of the speckle. The fringe spacing is

$$\Lambda = \frac{\lambda}{\sin\theta} \qquad 1.14$$

and the resolution of the system is

$$R \approx \frac{9}{N} \text{ FOV}$$

1.15

where N is the number of pixels on the CCD and FOV is the field-of-view of the reconstruction.

1.4   Optical Coherence Imaging (OCI)

Tomographic techniques have successfully imaged through deep tissue and have found wide clinical and experimental applications. Ultrasound [32], X-ray computed tomography (CT) [33], and magnetic resonance imaging (MRI) [34] are standard imaging modalities found in hospitals all over the world. In more recent years, confocal microscopy [35-37], photoacoustic tomography (PAT) [38-43], and optical coherence tomography (OCT) [8, 10, 11] have achieved smaller resolutions and are growing in clinical use [44-47].

OCT is based on low-coherence reflectometry [48], an optical ranging technique that measures reflectance as a function of depth. OCT uses heterodyne detection to obtain a one-dimensional A-scan of the reflectance. When combined with a second, transverse OCT scan, a two-dimensional B-scan image is generated. The joint system rasters across the target to construct the full 3D image. Depth resolution is limited by the coherence-length of the source independent of the numerical aperture of the imaging system, which allows OCT systems to use very small optics, such as those in an

endoscope. OCT has gained wide acceptance since it was first reported in 1991 [8]. It has a penetration depth of about 1 mm in turbid media and a spatial resolution near the diffraction limit for shallow depths in translucent media.

In 1996, Dr. David Nolte's group, in collaboration with Dr. Paul French of Imperial College, London, invented holographic optical coherence imaging (OCI) [49] as a full-frame imaging version of optical coherence tomography (OCT) for probing tissue up to a millimeter in depth. In OCI, positioning the reference off-axis relative to the optical axis of the scattered photons creates a spatially modulated intensity profile. The off-axis orientation allows OCI to record the full image frame in a single capture. OCI was first performed using photorefractive quantum well (PRQW) devices to image live rat osteogenic tumor spheroids [50, 51]. Dr. Kwan Jeong updated the OCI system by moving the PRQW device from image plane to Fourier plane and, later, by replacing the PRQW device with a digital CCD camera [52-54]. Current OCI uses low-coherence [55-58] digital holography [59] to reduce background and improve sensitivity. It achieves high frame rates (25 frames per second) while maintaining resolution and has proven to be a useful tool for studying tissue-level biophysics.

1.4.1 Fourier-domain digital holography

At the core of the OCI is Fourier-domain digital holography. The theory is explained in greater detail in [7, 54]. In brief, consider the Mach-Zehnder interferometer shown in Figure 1.2.
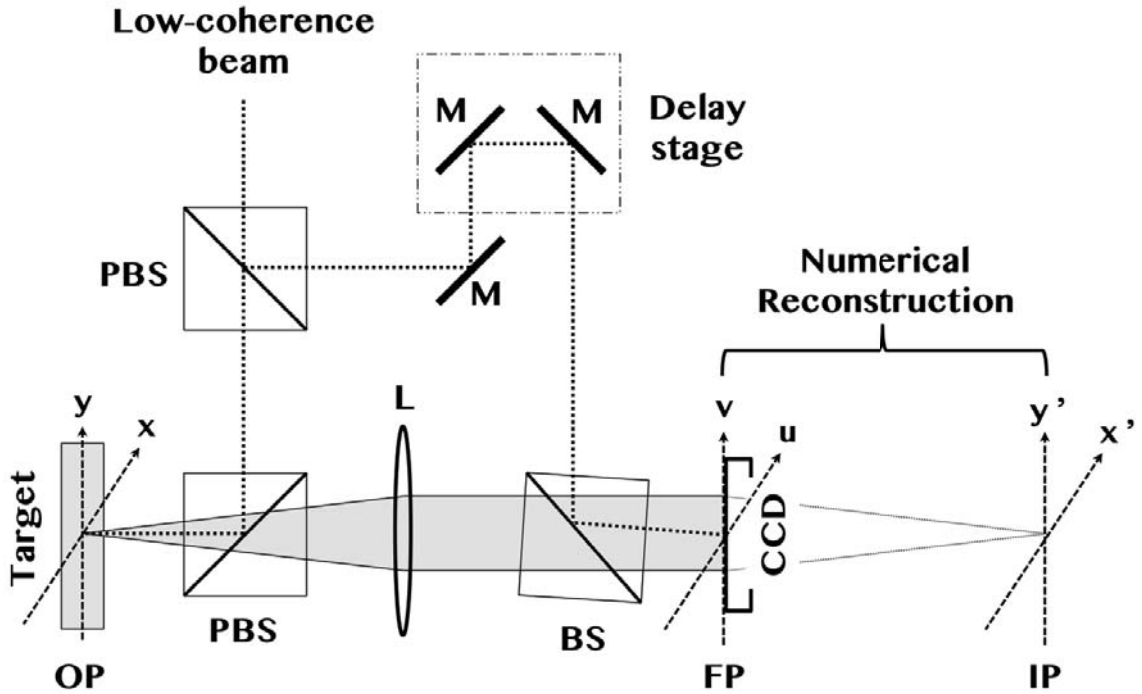
Figure 1.2. Fourier-domain digital holographic configuration. A beam splitter (BS) splits the light into two coherent beams: the object beam that impinges on the target, and the reference beam that is routed through a series of delay mirrors (M). Light scattered from the target (OP) is projected onto the Fourier plane (FP) by the lens (L) where it is spatially heterodyned with the reference beam, and the CCD records the resulting interference as an intensity hologram. The hologram is numerically Fourier-transformed back into an image (IP) of the target.

A beam splitter splits the coherent light wave into two waves: a reference plane wave and an object wave. The object wave $E_o(x, y)$ scatters off a target and is Fourier-transformed by an ideal lens of focal length f onto the plane of the CCD camera. The object wave at the plane of the detector is given by

$$E_{od}(u, v) = \frac{i}{\lambda f} \exp\left(-\frac{i4\pi f}{\lambda}\right) \int_{-\infty}^{\infty} \int_{-\infty}^{\infty} E_o(x, y) \exp\left(\frac{i2\pi}{\lambda f}(xu + yv)\right) dx\, dy \quad 1.16$$

where λ is the wavelength of the source. The reference wave travels through the delay path and is directed onto the detector so that at the detector. The reference plane-wave is given by

$$E_{rd} = E_r \exp\left(i2\pi(v_x x + v_y y)\right) \qquad 1.17$$

where v_x and v_y are the spatial wavenumbers. The reference wave in OCI replaces the need for a phase modulator in conventional OCT, and an off-axis configuration provides a spatially modulated carrier wave, which allows for full-frame imaging of the hologram. The electric wave at the detector is a coherent sum of the object and reference waves. The intensity pattern recorded by the detector is

$$I_d(u, v) = |(E_{od} + E_{rd})(E_{od}^* + E_{rd}^*)| = |E_{od}|^2 + |E_{rd}|^2 + E_{rd}^* E_{od} + E_{rd} E_{od}^* \qquad 1.18$$

The first two terms of Eq. (1.18) are the respective intensities of the object and reference beams at the detector. The last two terms are Fourier- and conjugate Fourier-transforms of the image. After capturing the intensity pattern using a digital camera, a computer performs numerical reconstruction of the images using a fast Fourier transform (FFT). The third and fourth terms can be calculated using Eq. (1.16) and Eq. (1.17), and are given by

$$FT(E_{rd}^* E_{od}) = i\lambda f E_r \exp\left(-\frac{i4\pi f}{\lambda}\right) E_o\left(-\lambda f v_u + \lambda f v_x, -\lambda f v_v + \lambda f v_y\right) \qquad 1.19$$

and

$$FT(E_{rd} E_{od}^*) = -i\lambda f E_r \exp\left(\frac{i4\pi f}{\lambda}\right) E_o^*\left(\lambda f v_u + \lambda f v_x, \lambda f v_v + \lambda f v_y\right). \qquad 1.20$$

The image is located at $(\lambda f v_x, \lambda f v_y)$ and the conjugate image is located at

$(-\lambda f v_x, -\lambda f v_y)$, and are separated from the zero-order image at (0,0). Figure 1.3 shows

an example of recorded Fourier-domain hologram and the resulting reconstructed image.
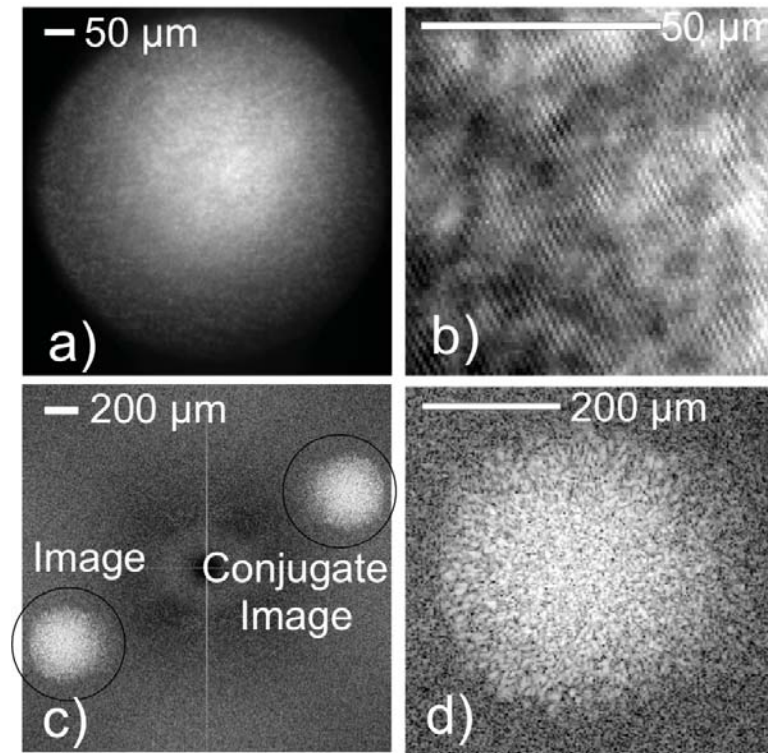
Figure 1.3. OCI frame and corresponding transformed image. a) The OCI Fourier frame captures b) a holographic intensity pattern when the optical path length difference between the object and reference beams is within the coherence length of the source. c) The corresponding image and conjugate image are reconstructed from the OCI frame through a fast Fourier transform. d) An image of the target, a tumor spheroid, can be seen.

For a CCD camera with pixel size $\Delta u \, (= \Delta v)$ and a chip size of N by N pixels,

the resulting reconstructed image has N by N pixels of size

$$\Delta x' = \Delta y' = \frac{\lambda f}{L} \qquad\qquad 1.21$$

where $L(= N\Delta u)$ is the width of the CCD chip. Fourier detection is less sensitive than

image detection to debris in the light path, and digital processing improves image contrast

and noise reduction capabilities. Holographic image capture also provides depth

resolution when a low-coherence illumination source is used.

1.4.2   Three-dimensional volumetric holography with low-coherence

Imaging through translucent, dynamic media is complicated for a source with

high-coherence because photons coherent at the detector have scattered from different

depths within the sample, Depth resolution can be achieved by using a low-coherence

source to generate the holograms [55]. With a low-coherence source, only photons whose

distance-of-flight is equal to that of the reference interfere coherently at the plane of the

detector to generate the hologram. In the backscatter configuration, the depth resolution is

given by [60]

$$\Delta z = \frac{2\ln 2}{\pi}\frac{\lambda^2}{\Delta\lambda}. \qquad\qquad 1.22$$

where $\Delta\lambda$ is the full-width-half-max (FWHM) bandwidth of the source. Scattered light

outside this volume is added incoherently and can be removed during image processing.

This coherence-gating allows for images to be made of specific depths within the target,

limited by the extinction of the beam within the target and by the sensitivity of the

detector.

1.5   The OCI system

Figure 1.4 shows a complete diagram of the current OCI system. A neutral density filter (ND) attenuates the light from the super-luminescent diode (SLD). The waveplate ($\lambda/2$) adjusts the polarization of the beam before it is split by a polarizing beamsplitter (PBS) into object and reference beams to maximize the intensity of the object beam. The object beam is focused by lens L1 onto the target, and the scattered light is collected and projected onto an image plane (IP) by lenses L2 (f = 15 cm) and L3 (f = 15 cm). The projected image plane is Fourier-transformed by lens L4 (f = 5 cm) onto the second Fourier-plane (FP2) at the camera (CCD) with a 1/3 magnification. The reference beam passes through the delay stage (dotted box) and is attenuated by another ND to match the intensity of the object beam at the CCD. The reference beam is directed onto the CCD by means of mirrors (M). Lenses L5 and L6 are used to shape the reference beam to match the beam profile of the scattered object beam at the CCD. Interference patterns are recorded and digitally Fourier-transformed back to the image plane to generate OCI images of the target. The delay stage can be adjusted to probe different depths within the target.
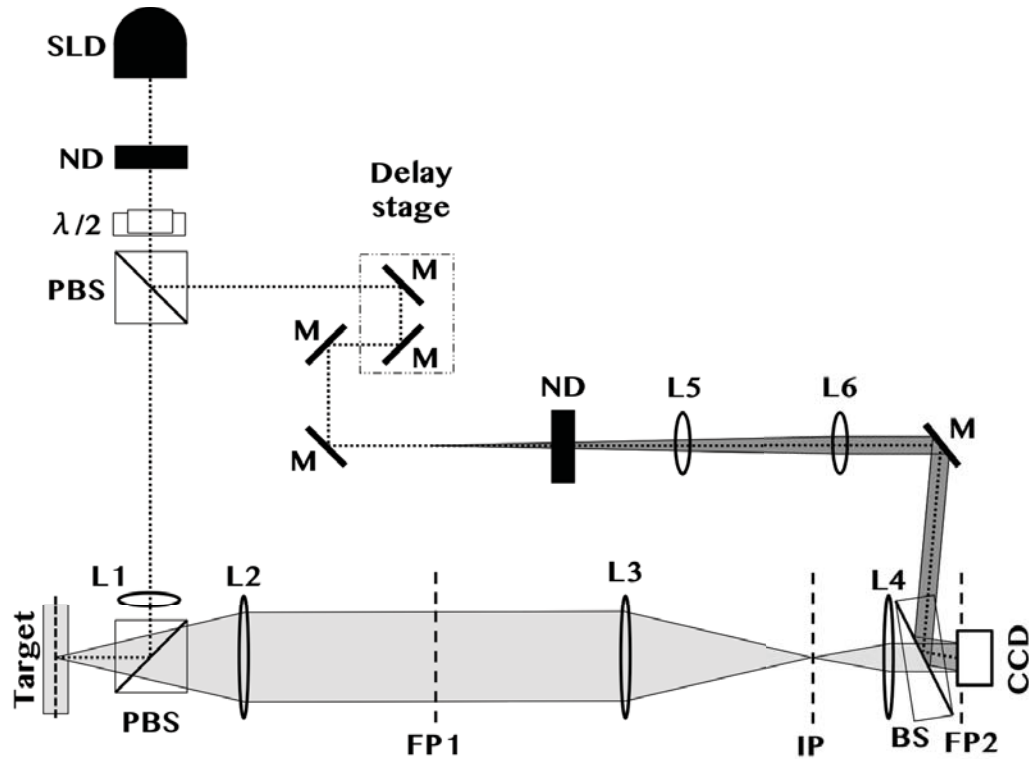
Figure 1.4. BDI setup.

Short coherence light at 847.2 nm wavelength with 50 nm FWHM bandwidth is supplied by a 20.5 mW Superlum Broadlighters Fiber Lightsource (model: S-840-B-I-20 SM). This gives a depth resolution of 6.3 μm (single-scattering). The CCD camera is a Rolera EM-C2 from QImaging with a bit depth of 14 bits. Recorded images are 800 by 800 pixels with a square pixel of size of 8 μm. This results in a minimum practical fringe spacing of 24 μm and a minimum speckle size of 72 μm. Capture is triggered externally through a function generator controlled by a custom-developed LabVIEW VI (National Instruments) that also controls the motion of the 2-axis translation stage and the reference

beam delay stage. Camera frames are recorded using StreamPix 5 (Norpix). Spatial

coordinates and zero-path matched position of the reference beam delay stage are

recorded for each tumor [61].

1.6   Motility Contrast Imaging (MCI)

Motility contrast imaging (MCI) [13] uses the speckle intensity fluctuations as a

label-free image contrast to create a false-color image of the sample motility. Sample

motility is influenced by all cellular activity and is an indication of cell health and

cellular action. MCI images can indicate regions of hypoxia/necrosis and other tumor

inhomogeneities that exhibit strong motional differences.

A sequence of OCI frames is captured, representing one observation of the living

target. By capturing several sequences, changes in the time-dependent behavior of the

target are detected. For a single OCI sequence, the temporal normalized standard

deviation (NSD) of the intensity I is defined at each pixel (x,y) as

$$NSD(x,y) = \frac{\sigma_I(x,y)}{\langle I(x,y) \rangle} = \frac{\sqrt{[\langle I^2 \rangle - \langle I \rangle^2]}}{\langle I \rangle} \qquad 1.23$$

This value is used to assign a color to each pixel to create a false-color MCI frame of the

motility of the sample during that sequence. Figure 1.5 shows MCI frames of two

different HT-29 tumor spheroids following the application of either growth medium or

nocodazole (10 μg/mL). The motility of the sample changes very little after the growth

medium is applied while the nocodazole causes significant decrease.
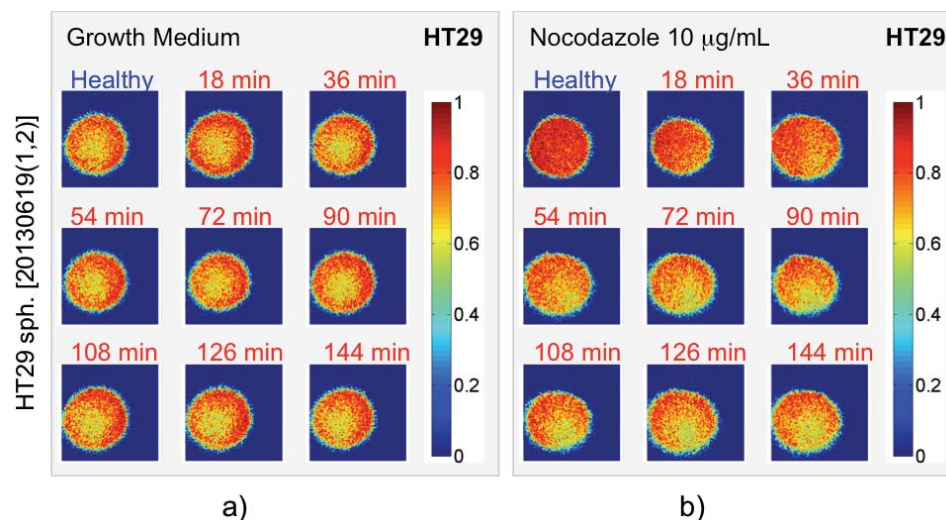
Figure 1.5. MCI frames of healthy and treated HT-29 tumor spheroids at successive times. Frames show the motility of the spheroid after application of either a) growth medium, in the healthy case, or b) 10 µg/mL nocodazole, for the drugged tumor. Motility of the healthy tumor is maintained while that of the drugged tumor decreases over time as the nocodazole begins to affect cellular processes. MCI frames also show the low-motility region that often forms in the interior of the tumor spheroids.

Changes in sample health can be inferred by calculating the average NSD of the entire sample during a particular OCI sequence and recording that average over time. Figure 1.6 shows the average NSD in time for two different tumor spheroids. One spheroid received growth medium at time $t = 0$ while the other tumor received 10 µg/mL nocodazole. The average sample NSD decreases rapidly following the application of nocodazole. The average NSD of the healthy tumor did not change significantly, from which can be inferred that the growth medium maintained the health of the sample.
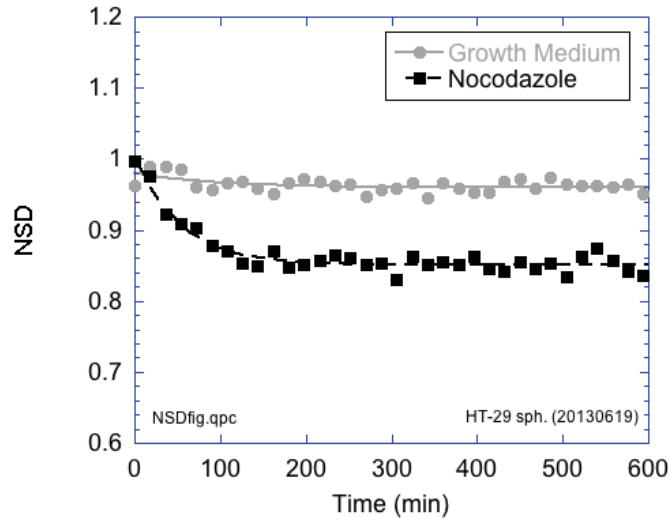
Figure 1.6. Average NSD of healthy (growth medium) and drugged (nocodazole) tumor. The motility of the drugged tumor decreases rapidly following the application of nocodazole (10 μg/mL) with a decay time of 33 minutes

MCI and average NSD detect changes in the overall motion of a sample, but these changes can arise from several different biological processes. Tissue dynamics spectroscopy analyzes the different frequencies of motion within the sample to separate one process from another.

1.7   Tissue Dynamics Spectroscopy (TDS)

Another technique within BDI is tissue dynamics spectroscopy (TDS) [62]. TDS uses speckle fluctuation spectroscopy on the reconstructed OCI frames to produce a characteristic power spectrum for the sample. The shape of this power spectrum is dependent on the motion of scattering objects within the sample and changes with changing sample conditions. The theory is explained briefly.

Different biological processes happen at characteristic speeds [20, 63, 64]. All these processes result in local fluctuations in the index of refraction and cause dynamic changes in the scattered speckle. The autocorrelation of the intensity I of a pixel is given by

$$A(\tau) = \langle I(0)\, I(\tau)\rangle = \langle I\rangle^2 + [\langle I^2\rangle - \langle I\rangle^2]\, exp\left\{-\frac{\tau}{\tau_C}\right\} \qquad 1.24$$

where τ_C is the relaxation of the process. For diffusion,

$$1/\tau_C = q^2 D = 4Dk_i \sin^2(\theta/2) \qquad 1.25$$

with k_i being the magnitude of the wavevector of the incident light and D being the diffusion coefficient. The autocorrelation can be written as

$$A(\tau) = 1 + (NSD)^2\, exp\left\{-\frac{\tau}{\tau_C}\right\} \qquad 1.26$$

The Fourier transform is a Lorentzian

$$S(\omega) = \frac{(NSD)^2\, \tau_C}{(\omega\, \tau_C)^2 + 1} \qquad 1.27$$

In log-space, $S(\omega)$ has a distinct shape and exhibits a knee frequency

$$\omega_C = \frac{1}{\tau_C} = q^2 D \qquad 1.28$$

While the observed process may not be strictly diffusive, the power spectrum can be approximated as

$$S(\omega) = \frac{(NSD)^2/\omega_C}{(\omega\,/\omega_C)^s + 1} \qquad 1.29$$

Figure 1.7 shows how the relaxation time of the autocorrelation function influences the shape and knee frequency of the power spectrum, and Figure 1.8 shows how s influences the shape of the curve.
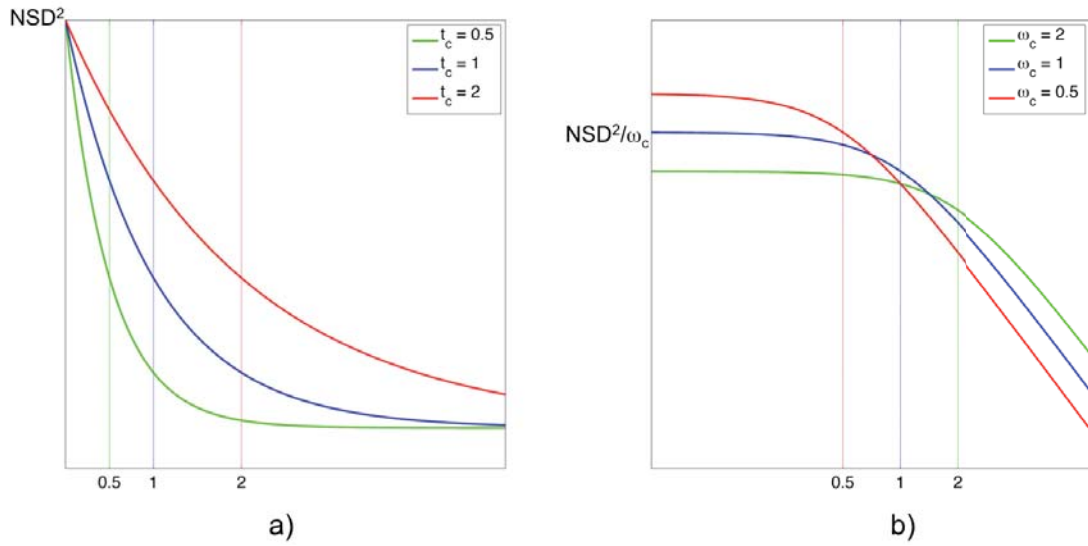
Figure 1.7. Example autocorrelation functions and power spectrum. a) Three autocorrelation plots are shown for three different relaxation times—0.5 s, 1 s, and 2 s—along with b) their corresponding power spectra.
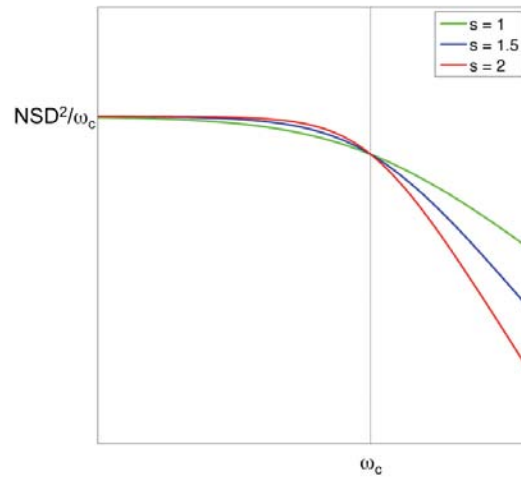
Figure 1.8. Example power spectra with exponential dependencies. The graph shows power spectra for three different values of *s*—1, 1.5, and 2.

A tissue sample may exhibit many different biological processes at the same time, causing its speckle fluctuation spectrum to have a complicated shape. Also, detection bandwidth causes information above the Nyquist frequency to be shifted to frequencies near the Nyquist. This raises the power spectral density at high frequencies and creates a Nyquist floor to which the power spectrum asymptotes. Figure 1.9 shows the fluctuation power spectrum for two different tumor spheroids. MIA PaCa-2 (PaCa-2) tends to be a more aggressive and active cancer cell line than HT-29, which may be reflected in the higher knee-frequency.
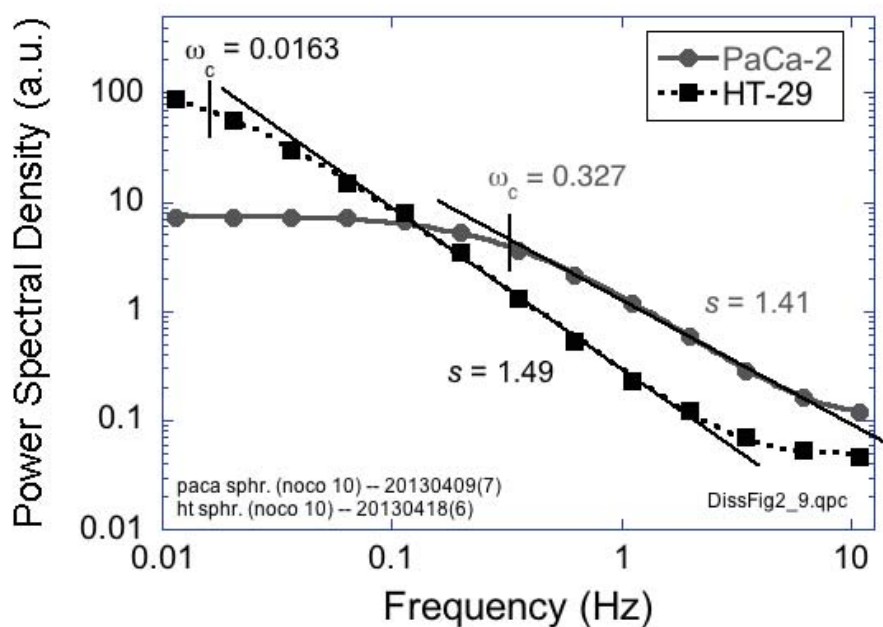
Figure 1.9. Example power spectra of healthy tumor spheroids for two different cell lines. Speckle fluctuation power spectra show the power spectral density for different frequencies of motion of scattering objects within the target volume and are characteristic of the behavior of the target. The power spectra are fitted with a modified Lorentzian function. For the HT-29 spectrum, the effective relaxation time $\tau_C = 61.3$ seconds and the exponent of the fit $s = 1.49$. For PaCa-2, $\tau_C = 3.06$ seconds and $s = 1.41$.

By comparing the power spectrum of a sample after a perturbation relative to the baseline power spectrum of the sample, the time-dependent response of the sample to the perturbation can be determined. For a power spectrum $S(\omega, t)$ measured at time t, the differential spectral power is defined as

$$D(\omega,t) = \frac{S(\omega,t) - S(\omega,t_0)}{S(\omega,t_0)} \qquad\qquad 1.30$$

where t_0 is the time of the baseline measurement. More recently, computations have used

$$D(\omega,t) = \log\left[S(\omega,t)\right] - \log\left[S(\omega,t_0)\right] \qquad\qquad 1.31$$

Eq. (1.30) is the first-order term in the Taylor expansion of Eq. (1.31), so in the limit that $S(\omega, t) \ll S(\omega, t_0)$ the two definitions are equal. However, Eq. (1.31) is less susceptible to noise in the spectrum.

The differential spectral power can be represented by a drug-response spectrogram that acts as a "voiceprint" of the sample response to a perturbation. Figure 1.10 shows example response spectrograms for tumor spheroids of two different cell lines, PaCa-2 and HT-29, to nocodazole (10 µg/mL). Frequency (horizontal axis) spans three orders of magnitude from 0.01 Hz to 12.5 Hz. Time (vertical axis) typically spans 11-16 hr. The zero on the time axis marks the introduction of the perturbation (nocodazole in Figure 1.10).
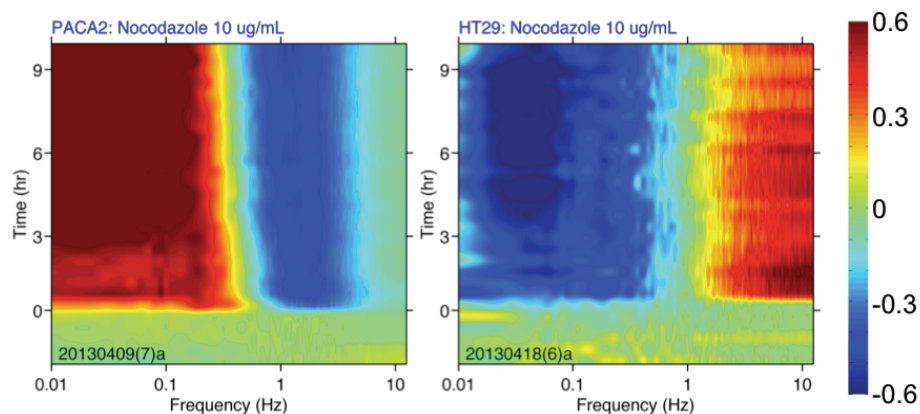
Figure 1.10. Example drug response spectrograms to nocodazole (10 μg/mL) for spheroids of two different cell lines. The 2D color graph shows shifts in speckle fluctuation spectra relative to the baseline sample spectrum. These shifts are indicative of changes in the dynamics of the spheroid due to the introduction of the drug.

The amplitude of the differential spectral power is indicated by color. Shifts to higher power are red, indicative of an enhancement of the motions in the target at that frequency. Blue areas mark shifts to lower spectral power and indicate suppression of motions at that frequency. Thus a spectrogram gives an easily readable representation of the changes in motion of the imaged volume in response to the perturbation. In Figure 1.10, two tumor spheroids from different cancer cell lines, MIA-PaCa-2 (PaCa-2) and HT-29, respond to the microtubule-destabilizing drug nocodazole. As microtubules make up part of the cytoskeleton of the cell, the destruction of microtubules leads to less rigid structure in PaCa-2 and a corresponding enhancement appears in the low frequencies as cell deformation increases. HT-29 forms a more rigid cell structure (see CHAPTER 2.4) and the cell deformations do not appear at frequencies above 0.01 Hz, but the high frequency enhancement in the spectrogram indicates increased vesicle activity as the cells respond to microtubule depolymerization.

1.8   Biomarkers and Feature Vectors

BDI generates a wealth of information that is difficult to quantify objectively. One

method developed is to use feature vectors to condense the results from OCI, MCI, and

TDS into a set of values that characterize a single sample response measurement. The

feature vector includes a set of conditional biomarker values calculated from OCI, MCI,

and TDS measurements of the initial and final condition of the sample. Examples of such

markers are backscatter intensity (BB), NSD, spectral knee frequency and slope, and the

change in these parameters.

Other biomarker values are obtained through a linear filter applied to the

spectrogram and integrated over log frequency. For linear filter $L(\omega, t)$, the biomarker

value M is

$$M = \langle \int_{\omega_{min}}^{\omega_{max}} L(\omega, t)D(\omega, t)d(\ln \omega) \rangle \qquad 1.32$$

Figure 1.11 shows a collage of different linear filters used to generate biomarker values

entered into the feature vector.
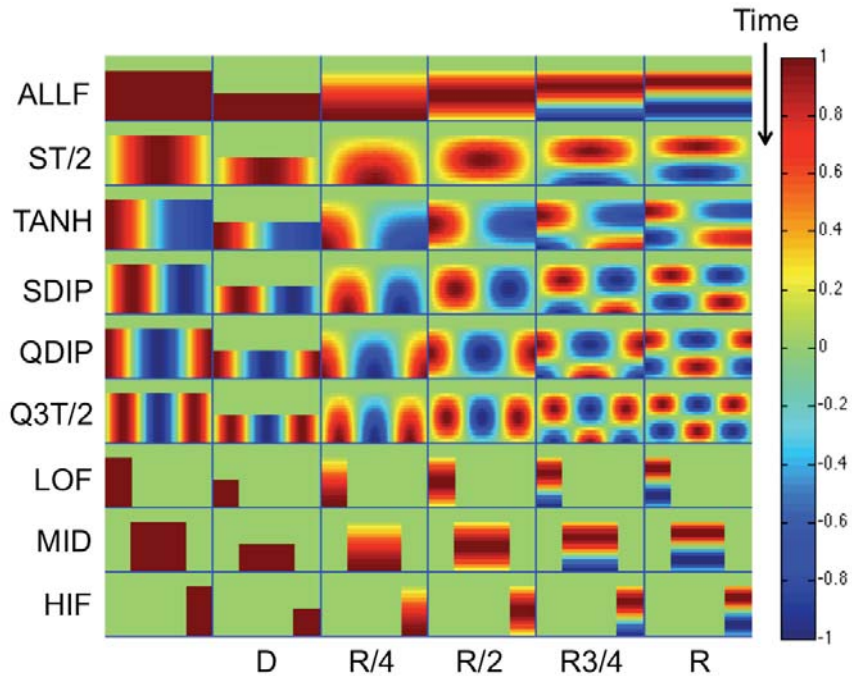
Figure 1.11. Collage of linear biomarker filters.

Other biomarkers come from logical combinations of the linear filters described above and select for specific biological responses. For example, APOP is a nonlinear filter that identifies enhanced frequency bands at high and low frequencies (a signature that previously has been correlated with apoptosis [65]).

CHAPTER 2. CELLULAR ADHESION EFFECTS IN BIODYNAMIC IMAGING

2.1   Abstract

In this chapter, biodynamic imaging is used investigate the change in adhesion-dependent tissue response in 3D cultures. Cellular adhesions play a role in tissue dynamics and have connections to chemotherapeutic resistance and metastasis. The results of this study show that increasing density of cellular adhesions slows motion inside tissue and alters the response to cytoskeletal drugs. A clear signature of membrane fluctuations was observed in mid frequencies (0.1 – 1 Hz) that was enhanced by the application of cytochalasin-D that degrades the actin cortex inside the cell membrane. This enhancement feature is only observed in tissues that have formed adhesions, because cell pellets initially do not show this signature, but develop this signature only after incubation enables adhesions to form.

2.2   Introduction to cellular adhesions

Traditionally, imaging through deep tissue has been difficult and *in vitro* tissue assays have favored a two-dimensional (2D) culture model. However, while 2D culture assays have the advantage of simplicity, 2D monolayer cultures feature an artificial environment that modifies cell shape and cell contacts and provides limited connections to the surrounding extracellular matrix (ECM). Furthermore, the mechanical and

chemical properties of, and the contacts with, the extracellular environment modify expression of adhesion compounds and adhesion structure [66-69]. Cellular adhesions have been linked to the development and spread of various cancers including colorectal [70, 71], breast [72], ovarian [73], and lung [74], and may contribute to the resistance of tumors to chemotherapeutic treatments [75, 76]. Cellular adhesions are an important target of chemotherapy research. 2D cell cultures, with a modified cellular environment and lack of adhesions, may change how they respond to chemotherapeutic drugs. A more biologically accurate, three-dimensional (3D) tissue model is needed.

Multicellular tumor spheroids closely resemble the macrostructure of *in* vivo cancer tumors [77]. Use of dense 3D tissue models such as tumor spheroids for drug testing has been limited by the difficulty to obtain information from deep tissue imaging. Biodynamic imaging (BDI) makes it possible to probe processes within the tissue without altering the surrounding microenvironment. In this chapter, BDI and dynamic light scattering (DLS) are used to investigate how culture morphology affects cellular adhesions and the measured response of the sample to cytoskeletal drugs. Much of this work was reported in [78].

2.3   Materials and Methods

2.3.1   Cell cultures

Cell lines are from American Type Culture Collection (ATCC) Manassas, VA. Cells were cultured in their respective growth media (Table 2.1) at 37 °C in a humidified CO_2 incubator. All growth media contain 10% fetal calf serum (Atlanta Biologicals), penicillin (100 IU), and streptomycin (100 µg/mL).

Table 2.1. Cell culture information. Information about genetic mutations comes from [79, 80].

Cell Line	Cell Origin	Mutation	Growth Medium
HT-29	Human colon	c-myc, H-ras, K-ras, N-ras, myc, fos and p53	McCoy 5A
UMR-106	Rat bone	p53	DMEM
MIA PaCa-2	Human pancreas	p53, K-ras	DMEM

2.3.2   Cytoskeletal Drugs

Cytochalasin-D, colchicine, nocodazole, paclitaxel, and dimethyl sulfoxide

(DMSO) were obtained from Sigma. Each drug was prepared to twice the desired

concentration to allow for later mixing inside the sample well [78]. DMSO (0.05%)

dissolved in growth medium was used as the negative control in all experiments, and all

drugs were dissolved in DMSO before being added to the growth medium to improve

solubility. The cytoskeletal action of each drug is outlined in Table 2.2.

Table 2.2. Cytoskeletal drug information.

Drug	Abbr.	Mechanism of Action
Cytochalasin-D	Cyto.	Inhibit actin polymerization
Colchicine	Colch.	Inhibit microtubule polymerization
Nocodazole	Noco.	Inhibit microtubule polymerization
Paclitaxel	Taxol	Inhibit microtubule depolymerization

2.3.3   Tumor Spheroids

A 50 mL capacity Sythecon rotating bioreactor (Synthecon, Houston, TX) was

seeded with 2×10^6 cells in growth media. Bioreactors were incubated for 7-10 days, or

until tumor spheroids were just visible to the naked eye (200-300 μm), before spheroids began being used in an experiment [78]. Spheroids typically had diameters between 150 and 500 μm. Spheroids were immobilized in 8-well chamber slides. To immobilize the spheroids, they were first pipetted into each well. Then 75-100 µL of low gelling temperature agarose made up in medium without serum was added. After a gentle mixing step some of the mixture was withdrawn to leave approximately 100µL of material. The spheroid was typically covered by the agarose.

Slides were glued to a 2-axis translation stage in the OCI system to prevent the sample moving during observation. Eight tumors were selected from each slide for testing, typically one tumor from each well. Growth medium was heated to 37 °C and pipetted into each well until the well was full and any bubbles were removed. The wells were covered with a microscope slide to limit evaporation and contamination from the environment.

2.3.4   Cell Suspensions

Cells were grown in flasks until about 80 % confluent. Cells were then trypsinized and pipetted into a 1.5 in. diameter petri dish at 10^5-10^6 cells/mL. Low gelling temperature agarose was added until the sample was slightly more than 1 mm in depth at its center. Cells and agarose were gently mixed and the dish was incubated for ~4 hours prior to experimentation. Each sample was cut into roughly rectangular shape (~10 mm x 5 mm) using a razor blade and then placed inside a flow cell (49IR1, NSG Precision Cells). The lid of the flow cell held the sample in place. Growth medium was heated to

37 °C and between 3 and 5 mL were injected through the flow cell using a syringe and tubing (Figure 2.1) [78].

Figure 2.1. Flow cell and drug injection components. a) Drug injection components were a syringe (3-10 mL volume, depending on need), a needle (20 guage), a pipet tip, ~3 in. of 1/32 in. inner diameter flexible tubing, and two ~3 in. pieces of 1/16 in. flexible tubing. b) Components were assembled as shown, the cut sample was placed inside the flow cell, and the device was clamped to the target stage of the DLS system.

2.3.5   Cell Pellets

8-well chamber slides of cell pellets were prepared from centrifuged cell cultures and embedded in low-temperature gelling agarose. Slides received either no incubation, or 24 hours of incubation, prior to testing to allow adhesions to form. Slides of cell pellets were otherwise handled in the same manner as those of tumor spheroids [78].

2.3.6   Optical Coherence Imaging (OCI)

A diagram and explanation of the optical coherence imaging (OCI) system can be found in CHAPTER 1.5. OCI frames of each tumor spheroid were captured in cycles every 20-24 minutes, on average [78]. Each capture sequence consisted of 15-45 seconds

travel time to allow the system to transition between tumors, followed by frame capture: 10 background frames captured at 10 frames per second (fps) with the reference beam not zero-path matched, then 50 frames at 0.5 fps and 500 frames at 25 fps with the reference beam zero-path matched. All frames were captured with a 10 ms exposure time.

Tumor spheroids were observed for 12 cycles (4.8 hours) to allow the tumors to stabilize. Then half of the growth medium (~0.5 mL) was removed from each well and replaced with a control drug. Tumors were then observed for 27 cycles (10.8 hours).

2.3.7   Image-domain DLS

A diagram of the homodyne DLS system is shown in Figure 2.2 [78]. The incident beam at 840 nm wavelength was supplied by a high-coherence 106 mW Melles-Griot CW diode laser (56DOL817). The CCD camera used was a Retiga EX from QImaging. Capture was triggered externally through a function generator controlled by a custom developed LabVIEW (National Instruments) program. Camera frames were recorded using StreamPix 5 (Norpix). Another custom LabVIEW program controlled the pump (NE-500, New Era Pump Systems) used for drug injection.

Frames were captured in 4-minute cycles, capturing 250 frames at 10 fps followed by 100 frames at 0.5 fps. All frames were captured with a 10 ms exposure time. Cells in suspension were observed for 46 cycles (~3 hours) to allow the sample to stabilize. Then 2 mL of control drug was injected into the flow cell over 8 minutes to completely replace the growth medium. Samples were observed for 180 cycles (12 hours). Frame capture was continuous with 4 cycles given to the drug injection. At the end of the experiment,

samples were fixed by injecting 3 % glutaraldehyde into the flow cell and were observed

for another 16 cycles (~1 hour).
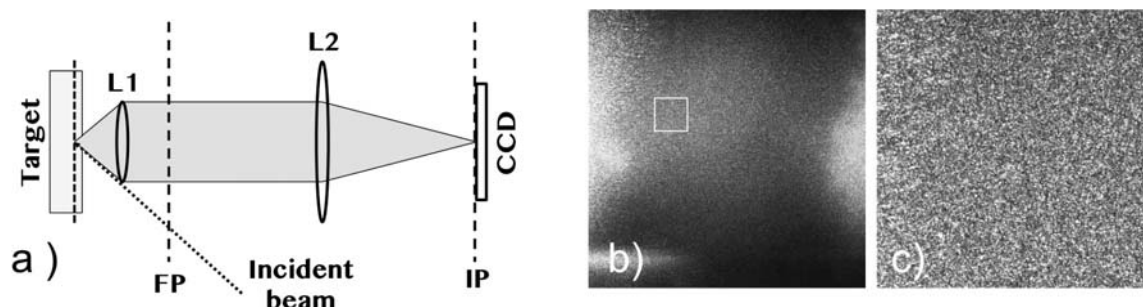
Figure 2.2. Image-domain DLS. In image-domain DLS (a), incident light from a CW laser scatters off a target and then is collected and projected onto the image-plane (IP) at a CCD by lenses (L1 and L2). Focal lengths of the two lenses are 5 mm for L1 and 20 mm for L2, resulting in a 4x magnification of the object plane at the CCD. The DLS frame captures an image of the object (b) as a dynamic speckle pattern. Dynamic measurements are made on a small portion of the sample (c), indicated by the white box in (b).

2.4   Cell line Trends in Cellular Adhesions

Three cell lines were chosen to investigate the effects of cell adhesion density on

the performance of biodynamic imaging [78]. The holographic MCI images (Figure 2.3a)

of human colorectal adenocarcinoma HT-29 demonstrated the strongest adhesions. They

form round spheroids and exhibit a low-motility core indicative of hypoxia even in small

tumors (< 100 mm). Human pancreatic carcinoma MIA PaCa-2 (PaCa-2) showed the

weakest adhesions, forming loose cell conglomerates instead of spheroids with no low-

motility core even in larger tumors (> 300 mm). Rat osteosarcoma UMR-106 had

adhesion density falling between the other two, forming round spheroids but exhibiting

low-motility cores in larger tumors.

Figure 2.3b shows microscope images of cells suspended in agarose for each cell line. HT-29 cells formed heterogeneous suspensions composed of cell clumps and individual cells. UMR-106 and PaCa-2 formed fairly homogenous suspensions. PaCa-2 formed slightly larger cell clumps due to rapid cell growth.
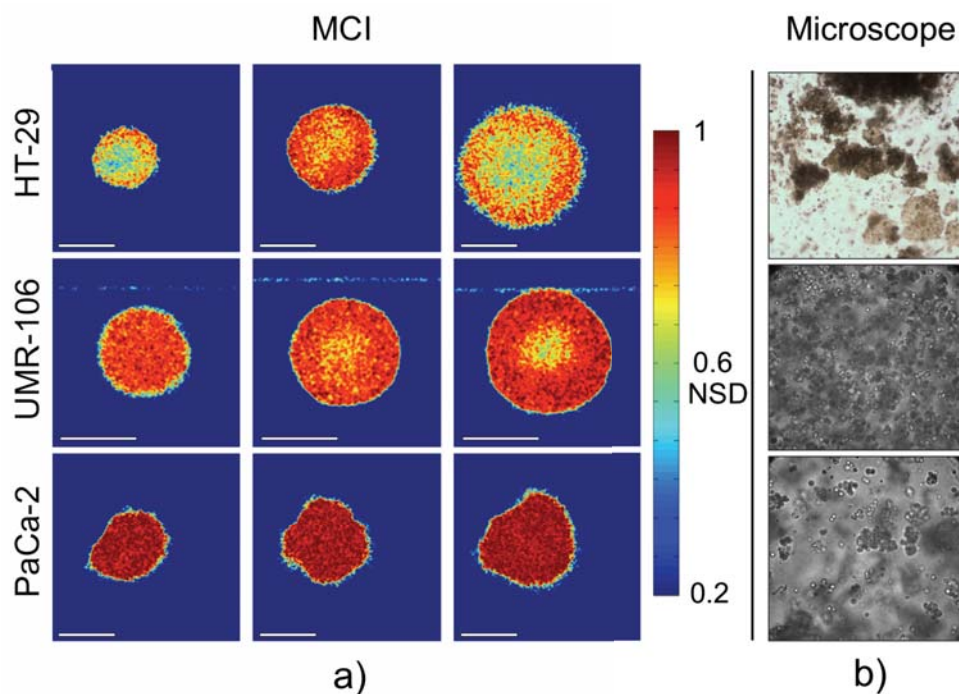
Figure 2.3. Holographic motility contrast images (MCI) (a) showing the shape and motility of tumor spheroids of different sizes for three cell lines along with microscope images (b) of cell suspensions for the same cell lines. The white bars in MCI are 200 μm. HT-29 formed tight, round tumor spheroids with large regions of low motility in the center even in tumors of less than 200 μm diameter. UMR-106 formed round tumor spheroids, with low-motility central regions typically appearing in spheroids of greater than 200 μm diameter. PaCa-2 formed irregularly shaped tumors that showed no low-motility regions even at sizes greater than 500 μm.

Sample responses were measured under the four cytoskeletal drugs (Table 2.2). Figure 2.4 shows average tissue response spectrograms for the three cell lines under the four drugs. Response to cytochalasin-D for the three cell lines showed an enhancement

in the mid-frequencies, generally between 0.1 and 1 Hz (shown in white square on the figure). This frequency band is associated with undulations in the cell membrane [63] and its enhancement is consistent with increased movement of the cell membrane due to a decrease in cell adhesions.
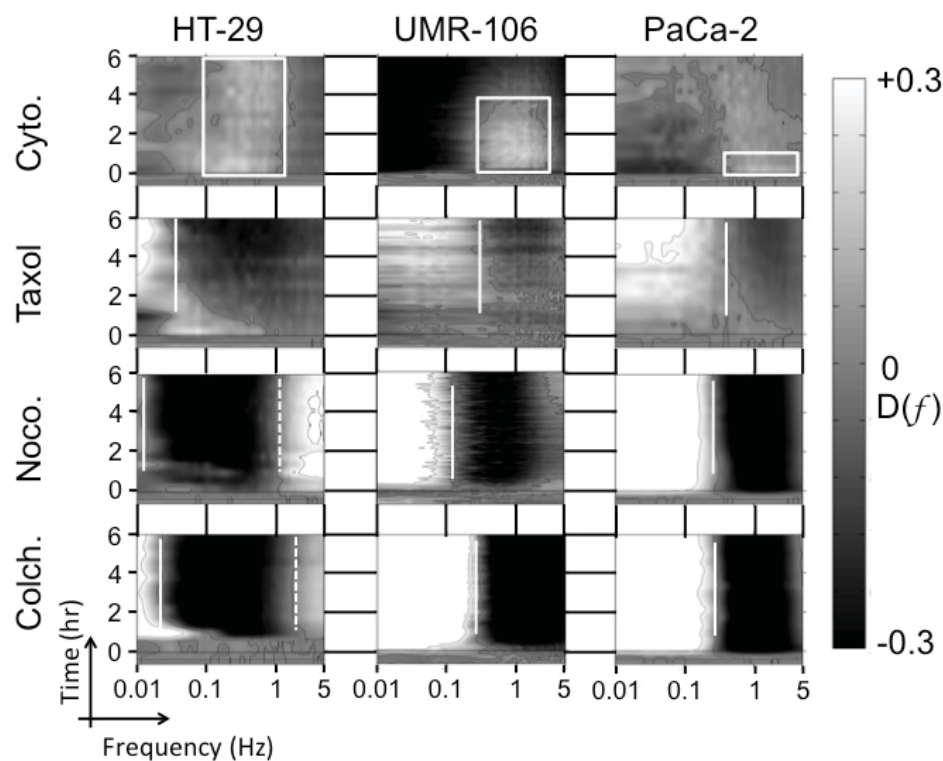
Figure 2.4. Biodynamic tissue response spectrograms of tumor spheroids responding to different cytoskeletal drugs. All drugs were administered at 10 µg/mL concentrations. BDI of HT-29 and PaCa-2 spheroids used a faster frame rate (25 fps) compared with BDI of UMR-106 (10 fps). The response of HT-29 to the microtubule-affecting drugs—paclitaxel (Taxol), nocodazole (Noco.), and colchicine (Colch.)—was noticeably different from the response of PACA-2 or UMR-106. The white lines highlight the zero-contour of the relevant feature.

The intensity and duration of the mid-frequency enhancement (Figure 2.5) caused by cytochalasin-D were proportional to the relative cell adhesion strengths of the three cell lines as predicted from the MCI images. The center frequency describes the

frequency about which the enhancement is centered which decreases with increasing

relative cell adhesion strength, indicative of the resistive influence that cell adhesions

have on the motion of the cell membrane.
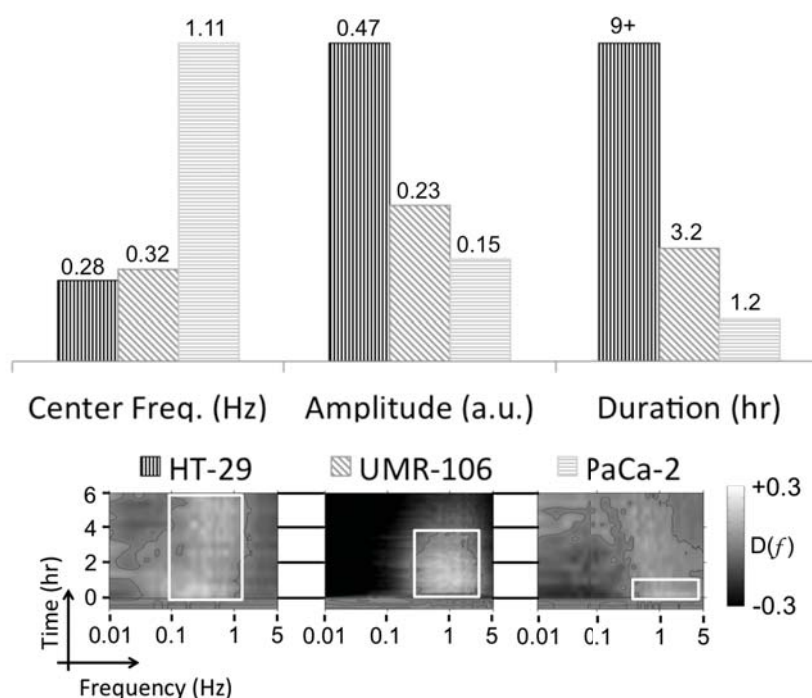
Figure 2.5. Response to cytochalasin-D. Center frequency, amplitude, and duration of mid-frequency enhancement measured from tissue dynamic response spectrograms for cytochalasin-D applied to different cell lines. As the relative adhesion strength of the cell line increases, the enhancement shifts to lower frequencies, suggesting slower motion, and has higher amplitude and longer duration.

The response to colchicine, nocodazole, and paclitaxel (Figure 2.4) in UMR-106

and PaCa-2 showed a low-frequency enhancement that shifts to lower frequencies with

increasing relative adhesion strength. Significantly, HT-29 response to these microtubule

drugs had almost no low-frequency enhancement, but does exhibit enhanced motion

above 1 Hz. This high-frequency enhancement was observed in the UMR-106 and in PaCa-2 at or above 5 Hz.

2.5   Influence of Growth on Cell Adhesion Formation

To test the effect of different growth techniques on drug responsivity, tissue response was measured for three different cell culture growth environments: tumor spheroids, cell pellets, and cells suspended in agar [78].

The response in UMR-106 to colchicine and paclitaxel (Figure 2.6) is consistent between tumor spheroids and cells in suspension. Colchicine shows a characteristic low-frequency (0-0.1 Hz) enhancement that reflects changes in cell shape due to reduction in cytoskeletal stiffness by inhibition of microtubule polymerization. The features of the response spectrogram shift from 0.05 Hz in the cell suspension to 0.1 Hz in the tumor spheroids due to the increased degree of multiple light scattering.
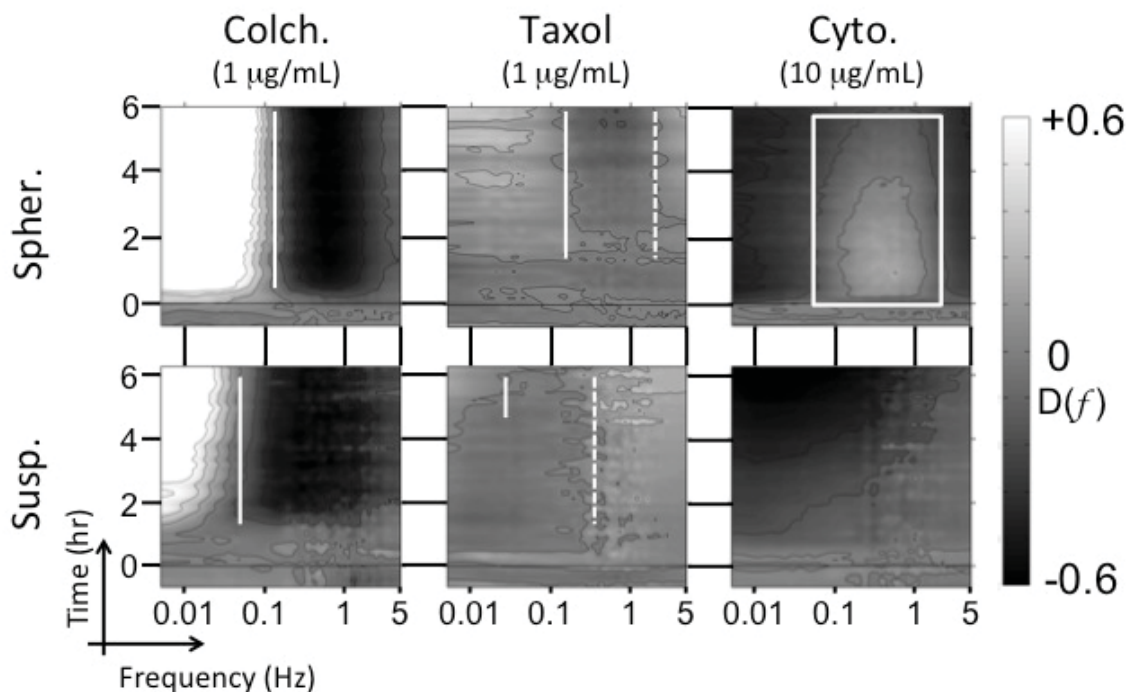
Figure 2.6. Comparison of tissue response spectrograms for UMR-106 to cytoskeletal drugs. Response spectrograms for cells in suspension (Susp.) under colchicine (Colch.) and paclitaxel (Taxol) present features (marked by the white lines) consistent with those for the tumor spheroids (Spher.) under the same drug. However, the response spectrogram for cells in suspension under cytochalasin-D (Cyto.) lacks the mid-range (0.1-1 Hz) enhancement seen in the tumor spheroid (white square). The white lines and square highlight the zero-contour of the relevant feature.

On the other hand, the response to cytochalasin-D in UMR-106 (Figure 2.6) is inconsistent between tumor spheroids and cells in suspension, and the mid-range (0.1-1 Hz) spheroid enhancement response is not present in the response of the cells in suspension. This lack of mid-range enhancement was found to be independent of the dose of cytochalasin-D, although the cells in suspension exhibit a overall suppression indicative of cell death with a time-to-saturation that is dose-dependent (Figure 2.7).
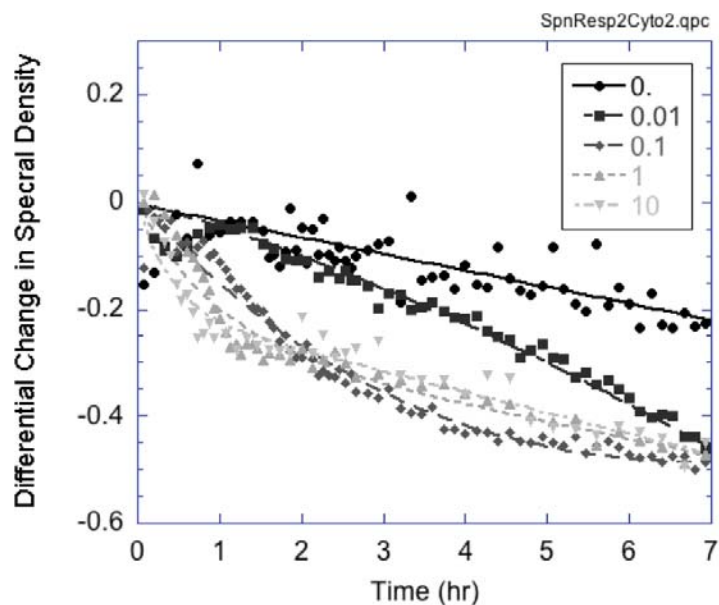
Drug Dose (μg/mL)	0.	0.01	0.1	1	10
Saturation Time (hr)	>340	20.9	6.1	0.9	0.4

Figure 2.7. Dose dependent response to cytochalasin-D for UMR-106 cells in suspension. Tissue response spectrograms for UMR-106 cells in suspension under cytochalasin-D at concentrations of 0, 0.01, 0.1, 1 and 10 μg/mL lack mid-range (0.1-1 Hz) enhancement at all doses. However, the average of the differential response shows an overall suppression whose saturation time decreases monotonically with increasing concentration. The saturation time estimates how quickly the cytochalasin-D affects the cells in suspension. Average differential response is averaged over frequencies from 0.005 to 1 Hz. The samples under 0 and 0.1 μg/mL cytochalasin-D have an slight initial enhancement relative to the baseline (0.095 and 0.126, respectively) that offsets the overall suppression measured.

Tumor spheroids and cell suspensions of PaCa-2 (Figure 2.8) show a difference in their respective drug responses that is similar to the difference in drug response of UMR-106, with the cell suspensions lacking an enhancement feature in the mid-frequencies that occurs in the drug response of the tumor spheroids. Spectrogram features for PaCa-2 appear at higher frequencies than UMR-106 in both tumor spheroids and cell suspensions,

which is consistent with the hypothesis that the lower adhesion density of PaCa-2 allows for faster cell membrane motion when the cytoskeletal drugs are applied.

To investigate the transition in response between the adhesion-poor environment of the cells in suspension and the adhesion-rich environment of the tumor spheroids, we measured the response of dense cell pellets formed from cell cultures. These pellets are optically dense like tumor spheroids, but initially they have fewer adhesions. Incubating the pellets allows adhesions to form. Cell pellets of PaCa-2 were treated with cytochalasin-D and their response was measured to rule out sample density and scattering frequency as the cause of this difference in drug response. Differing levels of cell adhesions were allowed to develop by changing the time over which the pellets were incubated. Pellets that received no incubation prior to testing showed a drug-response similar to that of the cell suspensions. After 24 hours of incubation, cell pellet drug-response showed a moderate enhancement in the mid-frequencies, becoming more like the tumor spheroid response, indicating increased formation of cell contacts prior to drug injection (Figure 2.8).
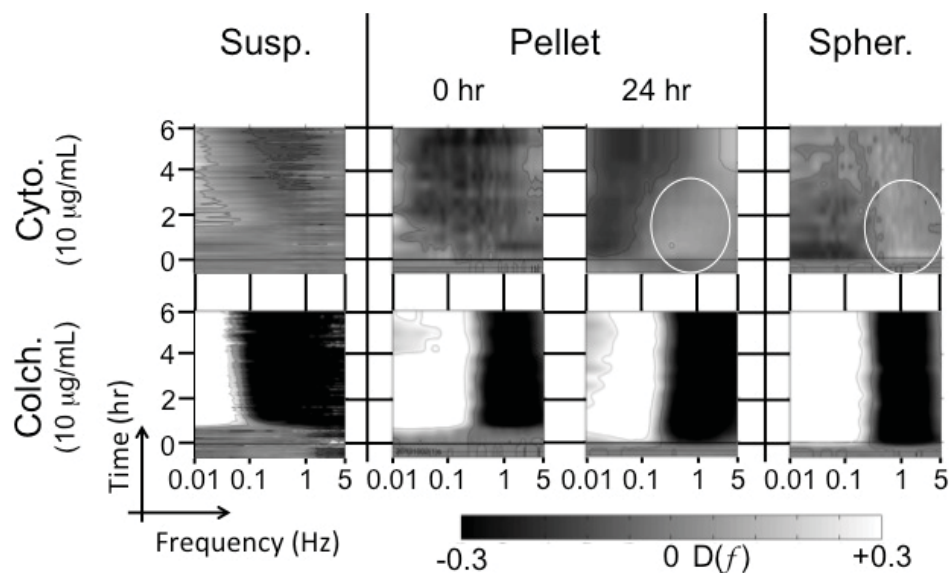
Figure 2.8. Tissue response spectrograms of PaCa-2 to cytochalasin-D and colchicine for cells in suspension (Susp.), cell pellets, and tumor spheroids (Spher.). Cell pellets were tested after 0 and 24 hours of incubation. The response to colchicine consistently shows a strong low-frequency range enhancement. The response of the cell pellets to cytochalasin-D demonstrated a transition in responses with the response of samples without incubation (0 hr) being similar to the response of cell suspensions, lacking the enhancement associated with changes in the cellular adhesions. After 24 hours of incubation the response becomes closer to that of the tumor spheroid and begins to show the expected enhancement (indicated by the white oval).

2.6   Discussion and Conclusion

Predicting cancer response to chemotherapies requires culture models that accurately mimic the native tissue microenvironment and requires assays that can measure cell response within that environment. In the present study, we used digital holography in the form of biodynamic imaging to study the response of multicellular tumor spheroids, a common 3D tissue model, to several cytoskeletal drugs. We also investigated how this response is altered by differences in the level of cellular adhesions present in the culture model.

Tumor spheroids of the three cell lines—HT-29, UMR-106, and PaCa-2—displayed strong changes in cellular motion in response to disruption of the cytoskeleton. For the UMR-106 and PaCa-2 cell lines, changes to the microtubules resulted in similar alterations in the cellular motion irrespective of whether the disruption was due to polymerization or depolymerization. The changes due to microtubule disruption for HT-29, however, are significantly different from those of UMR-106 and PaCa-2 over the frequencies measured. Cohen [81] showed that microtubule disruption in HT-29 induced cell differentiation and was accompanied by assembly and reorganization of the actin microfilaments, which suggests that HT-29 displays a response to nocodazole, colchicine, and paclitaxel that is physiologically different from that of UMR-106 or PaCa-2.

Tumor spheroids and cells in suspension exhibit significantly different behavior in response to cytochalasin-D for the UMR-106 and PaCa-2 cell lines. Drug dosage does not account for this difference, with dose only influencing how quickly a drug affects the cells. While cytochalasin-D appears to induce cell death in both the tumor spheroids and cells in suspension, only the adhesion-rich tumor spheroids showed significant increase in membrane motion accompanying the actin microfilament depolymerization. Ujihara found that actin disruption by cytochalasin-D significantly decreased adhesion area in fibroblasts while microtubule disruption by colchicine had a much smaller effect [82]. Greater decrease in adhesion area would account for the stronger difference in tissue response due to cytochalasin-D relative to colchicine observed between adhesion-rich and adhesion-poor culture models.

Holographic biodynamic imaging measurements on cell pellets with variable incubation demonstrate a transition from adhesion-poor to adhesion-rich environments.

This suggests that the difference in response shown by the cell suspensions and tumor spheroids is not due to differences in sample density, but is caused by changes in the microenvironment during incubation and is a strong indication of the influence of cell-cell contacts and the extracellular matrix on overall sample response to chemotherapeutic drugs.

In conclusion, a systematic study was performed of dynamic light scattering signals as a function of the adhesion strength among the cells in tissues grown from different cell lines and different growth environments. A clear signature of membrane fluctuations was observed in mid frequencies (0.1 – 1 Hz) that was enhanced by the application of cytochalasin-D that degrades the actin cortex inside the cell membrane. This enhancement feature is only observed in tissues that have formed adhesions, because cell pellets initially do not show this signature, but develop this signature after incubation enables adhesions to form. Digital holography, and in particular biodynamic imaging that uses digital holography to capture tissue dynamics, provides a new analysis technique to assess drug effects in natural 3D tissue environments.

CHAPTER 3. OVARIAN CANCER CELL LINES SENSITIVITY TO PLATINUM THERAPY

3.1   Abstract

Three-dimensional (3D) tissue cultures are replacing conventional two-dimensional (2D) cultures for applications in cancer drug development. However, direct comparisons of in vitro 3D models relative to in vivo models derived from the same cell lines have not been reported because of the lack of sensitive optical probes that can extract high-content information from deep inside living tissue. This chapter discusses the use of BDI to measure response to platinum in 3D living tissue. Human ovarian cancer cell lines were grown either *in vitro* as 3D multicellular monoculture spheroids or as xenografts in nude mice. Fragments of xenografts grown in vivo in nude mice from a platinum-sensitive human ovarian cell line showed rapid and dramatic signatures of induced cell death when exposed to platinum *ex vivo*, while the corresponding 3D multicellular spheroids grown *in vitro* showed negligible response. The differences in drug response between *in vivo* and *in vitro* growth have important implications for predicting chemotherapeutic response using tumor biopsies from patients or patient-derived xenografts. This chapter also discusses the use of BDI for *ex vivo* testing of *in vivo* drug exposure. Xenograft fragments from nude mice exposed to platinum treatment

in vivo showed decreased sensitivity to *ex vivo* re-exposure when compared to xenografts from untreated mice. This is the first time BDI has been used to assess the efficacy of *in vivo* treatment [3].

3.2   Introduction

Ovarian cancer accounts for 3% of all cancers in women. It is the fifth deadliest overall and the most deadly gynecological variant, killing 14,030 women in the United States in 2013. That same year 22,240 new cases were diagnosed [83, 84]. Approximately 80% of patients diagnosed with epithelial ovarian cancer (EOC) will relapse after first-line platinum-based and taxane-based chemotherapy. The average duration of *survival* after EOC *recurrence* is 12 to 18 months. Currently, fewer than one in ten patients with advanced EOC *survive* beyond 5 years. On the other hand, it has been shown that patients whose time-to-recurrence is increased have higher rates of overall [85, 86]. Recurrence of ovarian cancer is associated invariably with the emergence of partial or complete platinum or taxane resistance. Development of a methodology that can predict subsequent response to treatment would be useful for selecting chemotherapeutic or biological agents most likely to arrest tumor growth. At the present time, treatment selection is empirical, and is not individualized to tumor characteristics.

Even though cells thrive in three-dimensional environments and communicate with near and distant neighbors, most assays in cell biology use two-dimensional cultures. For instance, current methodologies used to predict response to therapy include 2D chemosensitivity assays that test cultured cancer cells to chemotherapy [87, 88]. These

assays have limited ability to yield cells from clinical specimens, lack predictive power for subsequent clinical applications [89-92], and rely solely on the epithelial tumor components. It is now known that cells in 2D do not behave as cells in 3D tissues, displaying different genetic expression profiles [93-95], different intercellular signaling [96-99], and different forces attaching them to their environment [69, 100, 101]. The cellular dimensionality and microenvironment exert an essential influence on drug sensitivity [102, 103] or resistance [104, 105] of 3D cultures relative to 2D monolayers. Therefore, an evolution is in progress in cell-based assays transitioning from 2D cell culture to 3D tissue because three-dimensional tissue presents a more natural environment to cells [106, 107], enabling contacts to the extracellular matrix and to other cells that translate to intracellular signaling [95, 99] and gene expression [93, 94, 108] that more closely replicate the tumor environment.

Three-dimensional tissue models that are ideal *in vitro* models to study complex three-dimensional tumor heterogeneity include multicellular tumor spheroids [15-17, 109], tumor xenografts from mouse models that are excised and tested in vitro, and finally human tumor biopsies. In spite of the distinct advantages of these 3D tissues [110], conventional imaging techniques are unable to penetrate deep enough within tissue to image the heterogeneous regions of tumors. Here we use biodynamic imaging (BDI) and the signatures of different dynamical cellular functions [111, 112] to solve this problem. We have validated BDI in applications of drug screening and phenotypic profiling [112-118], but this is the first application of the technique to pre-clinical cancer biology.

3.2.1 Biology of ovarian cancer

Ovarian cancers exhibit clinically relevant heterogeneity that makes it difficult to develop widely applicable treatments [84, 119]. Though surface epithelial cancer is the most common of ovarian cancers, there is controversy over the actual originating cells of different ovarian cancers [84, 119-122]. Surface epithelial ovarian cancer is classified as serous, endometrioid, mucinous, and clear cell type based on morphology, differentiation, progression, response to therapy, and prognosis. Classification is hampered by the fact that epithelial ovarian cancer can mimic cancers of the oviduct, uterus, and cervical canal. [120]. Several hypotheses have been advanced as to the cause of carcinogenesis [123-126].

Primary and recurrent ovarian cancers are generally bulky, and it is accepted that tumor heterogeneity related to polyclonal cell expansion is omni-present and partly responsible for variable and incomplete responses to therapy [127] and tumor recurrence. The recently-released results of the human tumor genome atlas for ovarian cancer demonstrated that ovarian tumors are characterized by genomic chaos and that no driver mutations or pathway activation characterize specific ovarian tumor subsets [128]. Thus therapeutic progress has been hindered by the inevitable emergence of chemotherapy resistance and tumor heterogeneity leading to incomplete or mixed tumor response [129].

A2780 is an established human ovarian epithelial cancer cell line cultured from tumor tissue of an untreated patient. A2780 responds to platinum treatments and has been used as a parent cell line to derive other platinum-resistant cell lines by culturing A2780 cells in the presence of platinum compounds. A2780/CP70 (CP70) is created by intermittently exposing A2780 culture to increasing doses of cis-

diamminedichloroplatinum(II) (cisplatin) up to 70 uM [130]. This cell line was later modified to stably express green fluorescent protein to create the A2780/CP70-GFP cell line (CP70-GFP). A2780cis is a platinum-resistant cell line derived from A2780 through chronic exposure to increasing concentrations of cisplatin [131].

3.2.2 Biochemical and biophysical effects of platinum therapies

There is a high degree of variability in response to existing and developing EOC therapies. Primary treatment is based on platinum and taxanes that follow initial surgery [132]. While platinum compounds have proved effective in increasing the survival rate among ovarian cancer patients, patient cancers frequently develop platinum-resistance. In many cases, these tumors also exhibit resistance to other standard-of-care therapies [130]. Predicting how a patient's cancer will respond to chemotherapeutic compounds is a critical tool for improving patient longevity and quality of life.

Cisplatin, cis-diamminedichloroplatinum(II), and carboplatin, cis-Diammine(1,1-cyclobutanedicarboxylato)platinum(II), are two common platinum compounds used to treat a number of cancers including ovarian, cervical, lung, and testicular types [130, 133-135]. The primary cytotoxic action of cisplatin is DNA damage [136, 137]. Cisplatin resembles alkylating agents and cross-links DNA strands by bonding to certain nucleotides [138]. These cross-links interfere with DNA replication and transcription. These DNA lesions are sensed by the cell and induce DNA repair or cell death. Increased DNA repair in associated with ciplatin resistance. This chapter presents a study of cisplatin response in sensitive (A2780) and resistant (A2780/CP70 and A2780cis) cell lines in *in vivo*, *ex vivo*, and *in vitro*, 3D tissue models using BDI.

<center>3.3   Materials and Methods</center>

<center>3.3.1   Animal and Tissue Models</center>

A2780 and A2780cis ovarian cancer cells were from Sigma. A2780/CP70 cells were a gift from Dr. Bob Sanders, University of Texas at Austin. A2780/CP70-GFP cells were produced in Dr. Daniela Matei's laboratory. Cells were cultured at 37 °C in a humidified CO_2 incubator in RPMI 1640 (Cellgro, Manassas, VA) supplemented with 10% fetal bovine serum (Cellgro) and 1% antibiotics [139].

Xenografts were generated by Dr Matei's laboratory through intraperitoneal (ip) implantation of $5x10^6$ cells into 6-7 week-old nude female BalbC mice. IP xenografts formed and were harvested after 4 weeks. Harvested tumors were placed in ice cold media and were transported to Dr. John Turek's laboratory within 2 hours and prepared for imaging. This extraction/transport/preparation protocol ensured that the samples experienced limited degradation during transport and preparation for BDI.
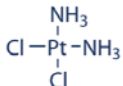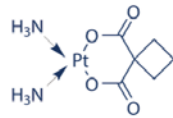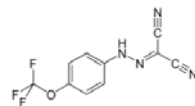
<center>3.3.2   Chemotherapy drugs</center>

Cisplatin and carboplatin were obtained from Selleck Chemicals. Dimethyl sulfoxide (DMSO) came from Sigma-Aldrich. Each drug was prepared to twice the desired concentration to allow for later mixing inside the sample well. DMSO dissolved (0.05%) in growth medium was used as the negative control in all experiments. DMSO was selected since cisplatin, carboplatin, and the positive control drug were each dissolved in DMSO before being added to growth medium to improve solubility.

Carbonyl cyanide 4-(trifluoromethoxy)phenylhydrazone (FCCP) was used as a positive control. To prepare the FCCP (Sigma-Aldrich), 50 mg was dissolved in 200 µL

of DMSO and divided into 40 aliquots of 5 μL each. 5 mL growth medium was added to one aliquot of FCCP to make the 200 μM FCCP solution used in each experiment. FCCP was chosen as a positive control because of the strong, predictable response demonstrated by other cancer cell lines. Table 3.1 shows chemical information for the three drugs.

Table 3.1. Chemical information. Information obtained from manufacturer's website.

Drug	Chemical name	Molec. Wt. (g/mol)	Chem. Struct.
Cisplatin	cis-diamminedichloroplatinum(II)	300.05	
Carboplatin	cis-Diammine(1,1-cyclobutanedicarboxylato)platinum(II)	371.25	
FCCP	Carbonyl cyanide 4-(trifluoromethoxy)phenylhydrazone	254.17	

3.3.3 Tumor spheroids

Spheroids were formed using two methods: rotating bioreactors (Synthecon, Houston, TX) as described in CHAPTER 2.3.3, and 96-well Corning U-bottom spheroid plates. The U-bottom growth technique generates spheroids more rapidly by using high cell seeding density. Plates were seeded with $1-5 \times 10^4$ cells and incubated with typical incubation times of 48-72 hours. CP70-GFP spheroids grew slightly slower than A2780, though this was most likely due to low seeding density. CP70-GFP spheroids showed greater longevity while A2780 spheroids often broke up after 48 hours. In general, the U-

bottom samples had lower cohesion and lacked extensive cellular adhesions and had only minor extracellular matrix compared to the samples grown in bioreactors.

Both 8-well slides (see CHAPTER 2.3.3) and 96-well plates were used for these experiments. The 96-well plates were prepared by first transplanting tumors from the Corning plates into standard 96-well plates (Falcon). The residual medium after pipetting was 50 µL. Then 75-100 µL of low gelling temperature agarose made up in medium without serum was added. After a gentle mixing step some of the mixture was withdrawn to leave approximately 100 µL of material. The spheroid was typically covered by the agarose. If bubbles remained in the mixture, the plate was degassed at 5-7 mm Hg briefly. The plate was then briefly placed inside a refrigerator to allow the agar to partially solidify. Finally, more growth medium was added to each well and the plate was placed at 37 °C in a humidified CO_2 incubator for 0-3 hours.

Slides/plates were glued to a 2-axis translation stage in the OCI system to prevent the sample moving during observation. 8-16 tumors were selected from each slide/plate for testing, typically one tumor from each well. Growth medium was heated to 37 °C and pipetted into each well until the well was full and any bubbles were removed.

3.3.4   Murine biopsies

Tumor biopsies were harvested from the peritoneal cavity of nude mice by Dr. Matei's lab (Figure 3.1). Biopsies were maintained at 4 °C for 5-48 hours before testing. Biopsies were sectioned using a razor blade to cut the tumor into pieces of approximately

1 mm^3 in volume. Pieces were affixed inside either 8-well or 96-well plates using a small

drop of GLUture (Abbot Laboratories) and covered with agarose. Growth medium was

added to each well. Experiments were performed immediately after plates were prepared.

Figure 3.1. Photo of sacrificed mouse. Cancer cells ($2x10^6$ cells/mL) were injected into
the peritoneal cavity of each mouse. Tumors (as one held by the forceps) formed on
peritoneal lining and on the surface of surrounding organs. Tumors developed (with or
without drug) for 3 weeks prior to harvesting.

3.3.5   OCI sequence

A diagram and explanation of the OCI system is found in CHAPTER 1.5. OCI

frames of each tumor were captured in cycles every 20-24 minutes, for an 8-sample

experiment, or 40-48 minutes, for a 16-sample experiment, on average. Each capture

sequence consisted of 15-45 seconds travel time to allow the system to transition between

tumors, followed by frame capture: 10 background frames captured at 10 frames per

second (fps) with the reference beam not zero-path matched, then 50 frames at 0.5 fps

and 500 frames at 25 fps with the reference beam zero-path matched.

Tumor spheroids were observed for 5 cycles (4 hours), for a 16-sample experiment, or 9 cycles (3.6 hours), for an 8-sample experiment, to allow the tumors to stabilize. Then half of the growth medium (~150 μL) was removed from each well and replaced with a drug at twice the intended concentration to minimally disturb the sample. Tumors were then observed for 12 or 24 cycles (9.6 hours), respectively.

3.3.6   Proliferation assay

Exponentially growing A2780 and CP70 cells were seeded in 96-well plates. Twenty four hours after seeding, cells were treated with 2, 4, 8, 16, 32 μM of cisplatin. After 72 hours of drug exposure, a cell counting kit-8 (CCK-8) assay was performed according to manufacturer's specifications (Dojindi). In a CCK-8 assay, a solution containing a water-soluble tetrazolium salt (WST-8) is added to the cell culture. WST-8 is reduced by dehydrogenases in cells to give an orange colored product (formazan), which is soluble in the tissue culture medium. The amount of the formazan dye generated by dehydrogenases in cells is directly proportional to the number of living cells. Growth inhibition curves were generated, where each point represents mean ± SD of 3 replicates. The 50% inhibitory concentration (IC_{50}) value was calculated by using nonlinear regression by fitting the normalized data to a sigmoid dose–response curve. The treatment of cells cultured as spheroids was carried out using the same cisplatin concentrations for 72 hours, and normalized data were plotted.

3.3.7   Logistic Predictor

To define the performance of the predictive assay for therapy response, a logistic model was constructed which incorporated three biomarkers. These are apoptosis-related (APOP), all-frequency (ALLF) and knee-frequency (KNEE) motility metrics (See Chapter 1). These three metrics correlated most strongly with the two cell line populations (sensitive and insensitive). The logistic function used is

$$\frac{1}{1 + e^{-ARG}}$$

3.1

The argument *ARG* in the logistic function is constructed from the mean values and standard deviations of the motility metrics to construct a multivariable logistic predictor L_n of drug response for the nth sample as

$$L_n = \text{logistic}\left[\sum_{m=1}^{M} \frac{(b_{nm} - K_m)}{\sigma_m}\right]$$

3.2

where *m* varies over the selected biomarkers, *M* is the number of biomarkers, b_{nm} is the value of the mth biomarker for the nth sample, s_m is the standard deviation of the mth biomarker, and K_m is the Kolmogorov-Smirnov threshold between the two populations (responsive and non-responsive) for the mth biomarker.

3.4   Results

3.4.1   Biodynamic characterization of A2780 and CP70-GFP cell lines

The growth of tumor spheroids in the rotating bioreactor provides sufficient time for the tumors to generate tighter tissues, with multiple adhesions and minor extracellular matrix, and these samples would be the closest to naturally-occurring avascular tumors

grown *in vivo*. The average NSD of the tumor spheroids are 0.82 ± 0.01 (N = 56) for

A2780 and 0.91 ± 0.06 (N = 53) for CP70. In addition, several samples were grown as

co-cultures of both cell lines, and these had an average NSD of 0.85 ± 0.06 (N = 4),

which is approximately the average of the two separate cell lines (Figure 2a). A

comparison of the three growth techniques (bioreactor, U-bottom and biopsy) shows that

the U-bottom plate samples had the highest motility with an average NSD of 0.89 ± 0.03

(N = 8) and 0.92 ± 0.01 (N = 30) for A2780 and CP70, respectively. In general, both cell

lines had lower motility when grown in the bioreactor (0.82 ± 0.01, N = 43; 0.89 ± 0.01,

N = 18). The lower bioreactor motility is consistent with the presence of more

intercellular adhesions that constrain the motion of the cell membrane, which is a major

contributor to the overall motility metric. Average values for A2780 biopsies are $0.74 \pm$

0.02 and for the A2780-cis biopsies are 0.78 ± 0.01 (Figure 2b).
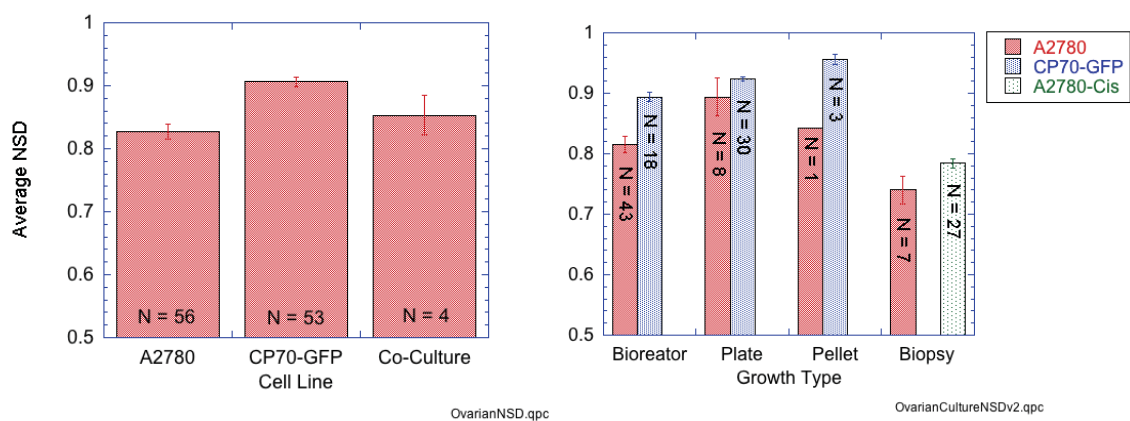
Figure 3.2. Average initial NSD of ovarian cultures. The number of samples averaged is indicated. Error bars show sample variability on the mean for each culture type. Cell line average NSD (left) includes samples of many different growth methods, including tumor spheroids, cell pellets, and murine biopsies. Though the average value of the initial NSD depends on culture growth type (right), the sensitive cell line always shows lower average initial NSD than the insensitive cell line.

MCI images of platinum-sensitive A2780 and platinum-insensitive CP70-GFP tumor spheroids (Figure 3.3) and murine biopsies show strong differences in the overall motility of the two cell lines. A2780 spheroids have regions of low motility tending toward the center of the tumor consistent with hypoxia occurring in the tumor's central region. CP70-GFP spheroids are more resistant to hypoxic effects due to constitutively expressed HIF1-α protein [140] and show less reduction in the motility of the central tumor region. Co-cultured spheroids of A2780 and CP70-GFP cells tend to form regions where one cell line predominates. MCI images of co-cultured spheroids show heterogeneous portions of high- and low-motility corresponding to groupings of CP70-GFP and A2780 cells, respectively. This separation was confirmed with fluorescence microscopy.
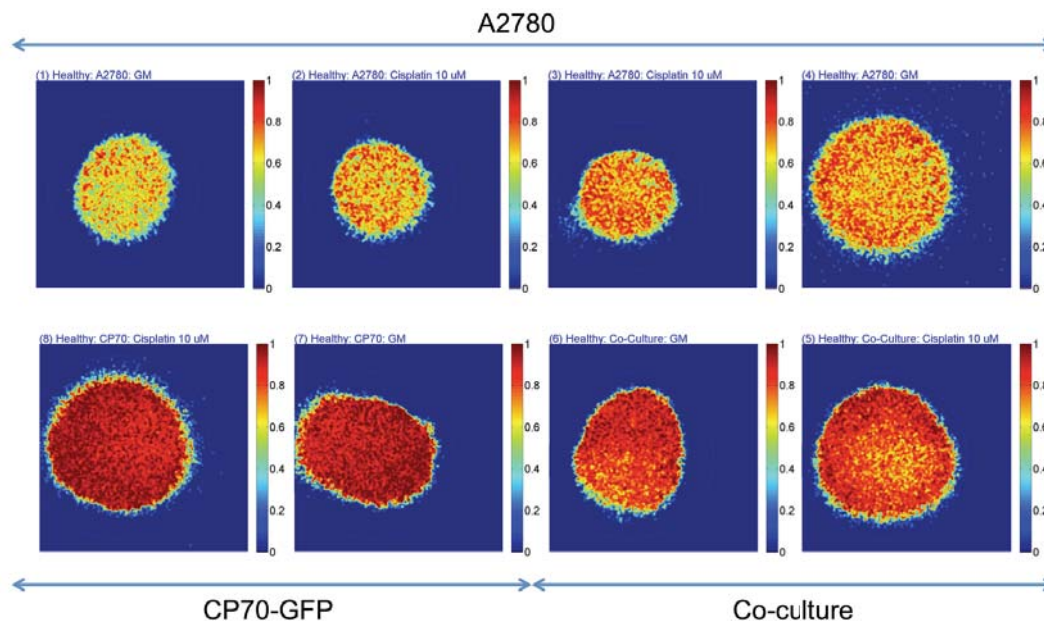
Figure 3.3. Sample MCI frames for sensitive (A2780), insensitive (CP70-GFP), and co-culture tumor spheroids. The difference in average motility is visible with A2780 tumor spheroids demonstrating much lower motility overall than the CP70-GFP. The co-cultured spheroids showed marginal heterogeneity with moderately high- and low-motility regions.

Examples of positive and negative control spectrograms are shown in Figure 3.4 for the mitochondrial toxin FCCP (100 M) and for the carrier DMSO (0.05%). The compound FCCP is a mitochondrial uncoupler (inhibits the mitochondrial membrane polarization), and the response of both A2780 and CP70 to FCCP is characteristic of TDS spectrograms on tumor spheroids from other cell lines [1]. The negative controls are relatively nonresponsive, with minor changes over time that are typical of healthy tissue samples that continue to proliferate.
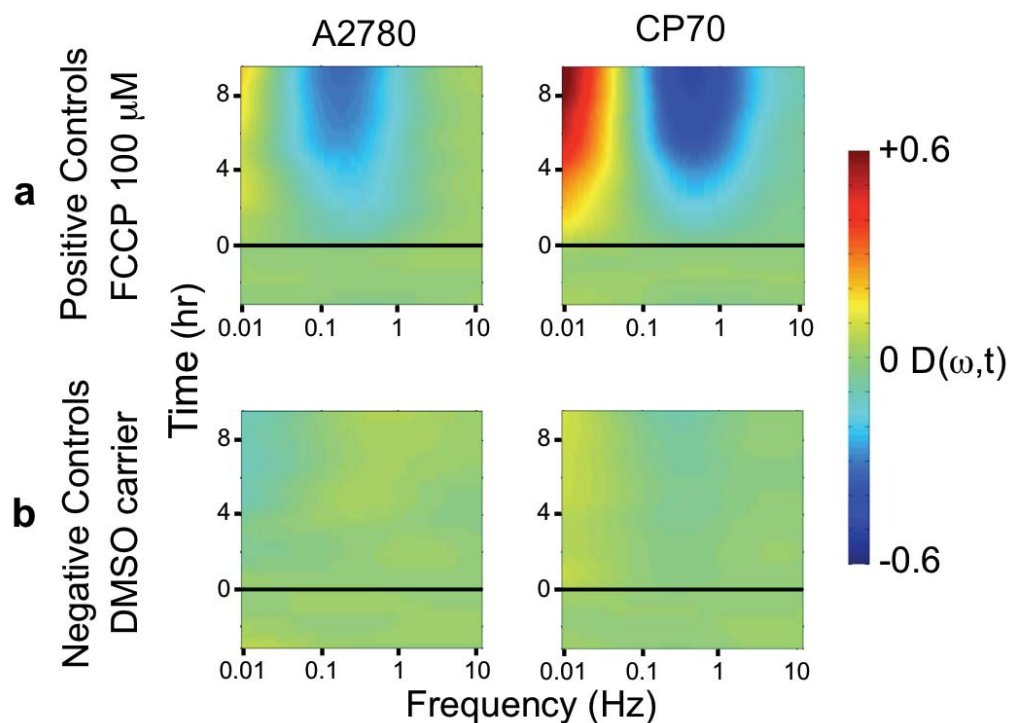
Figure 3.4. Tissue dynamics spectroscopy (TDS) control experiments on tumor spheroids from A2780 and A2780/CP70 (CP70) cell lines. a) Positive control consisted of 100 μM FCCP. b) Negative controls consisted of 0.05% DMSO.

3.4.2   Prospects for Therapy Efficacy Testing

Biodynamic imaging was used to measure the response of tumor spheroids and murine biopsies of platinum-sensitive and -insensitive ovarian cancer cell lines. The goal was to develop metrics for predicting sample response to chemotherapeutic treatments. Doses of 10 µM carboplatin or 10 µM cisplatin were administered to tumor spheroids (A2780 and CP70-GFP) and murine biopsies (A2780, CP70, and A2780cis) and tissue responses were measured. (However, the CP70 murine culture became infected before all experiments were completed, leading to low replicate numbers in some experiments). Table 3.2 gives sample numbers within each experimental group.

Table 3.2 Sample numbers for each drug group in therapy efficacy assessments.

		Sensitive		Resistant	
		Biopsy	Spher.	Biopsy	Spher.
Carboplatin	10 μM	6	3	7	2
	50 μM		3		4
Cisplatin	10 μM	7	11	7	24
	50 μM		4		1

Results show a strong response in the A2780 murine biopsies to both carboplatin and cisplatin while CP70 biopsies showed no significant response to cisplatin (Figure 3.5a). A2780cis biopsies also showed no response when treated. Tumor spheroids of both A2780 and CP70-GFP cell lines showed little significant response to either carboplatin or cisplatin even at high doses (Figure 3.5b). This result was unexpected. Average baseline and dosed spectra from tumor spheroids of sensitive and resistant cell lines are shown in Figure 3.5c. The baseline spectra show a normal spectral shape with knee frequencies at 0.018 Hz (A2780) and 0.025 Hz (CP70-GFP) and a slope of -1.2 for both cell lines. After treatment, the spectra show minimal changes in shape. The average baseline spectra of *ex vivo* xenograft biopsies (Figure 3.5c) have a knee frequency and slope of 0.0007 Hz and -1.3 for A2780, and 0.04 Hz and -1.8 for A2780cis. Figure 3.6 shows overall inhibition in ovarian tumor activity measured by BDI.
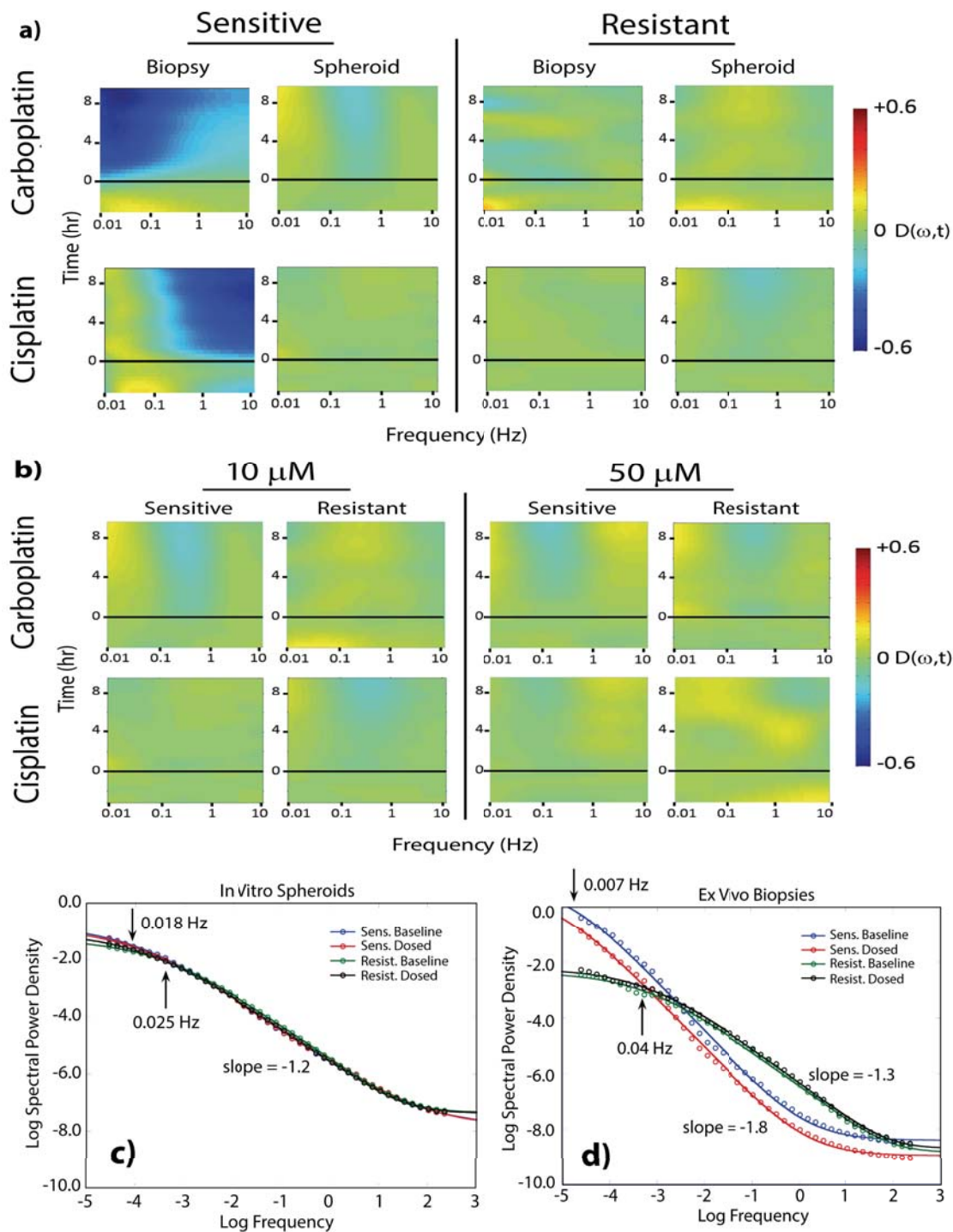
Figure 3.5. Tissue dynamics spectroscopy results of ovarian cancer cultures exposed to platinum compounds. a) Average TDS response spectrograms of sensitive/insensitive cell lines for biopsies and spheroids responding to cisplatin and carboplatin. The biopsies were xenografts grown from the same cell lines as the spheroids. The resistant biopsy data to carboplatin is from a related resistant cell line (A2780cis). There is a striking

difference in sensitivity between the A2780 explants relative to the spheroids. b) Average tissue dynamics response spectrograms of spheroids grown *in vitro* for A2780 (sensitive) and A2780/CP70 (resistant) cell lines and both platinum compounds for 10 μm and 50 μM over 9 hours after dose. Average baseline and dosed power spectra for c) *in vitro* spheroids and d) *ex vivo* xenograft biopsies of sensitive and resistant cells lines. Knee frequencies and slope parameters of each spectrum are indicated.
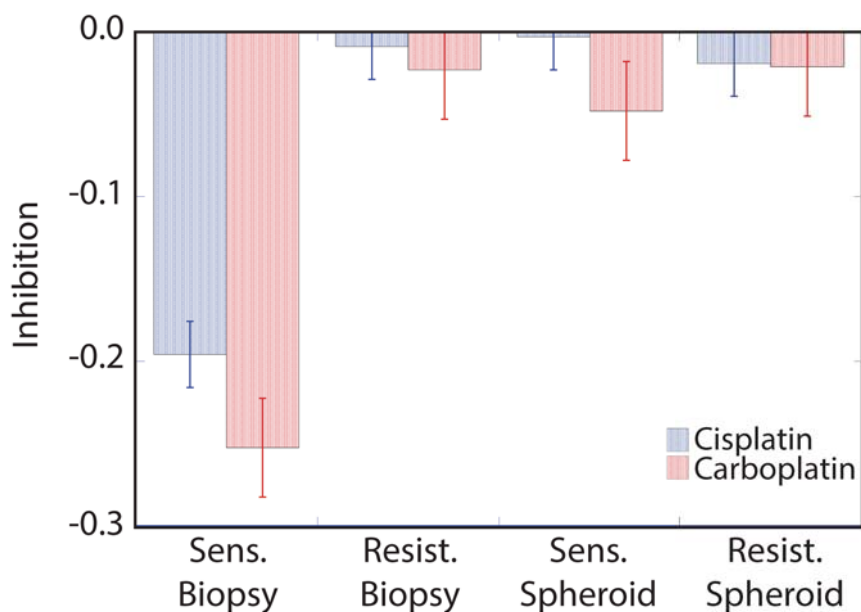
Figure 3.6. Inhibition, as measured by ALLF linear filter, of ovarian tumor activity in response to platinum therapy.

Distinct dose-dependent decreases in cell viability upon treatment with cisplatin were observed for A2780 (sensitive) and CP70 (resistant) cells, when grown as 2D monolayers. Spheroids were significantly more resistant to cisplatin compared to 2D cultures and differences between sensitive and resistant cells were not observed (Figure 3.7). Vascularization of the biopsies or effects caused by the transport of samples may account for the difference in sample sensitivity, and experiments are continuing. Tumor spheroids grown in a bioreactor have no significant stromal constituents, while xenografts

have mouse-derived stromal tissue as a constituent. In addition, clonal selection may be

different in the two different growth environments, leading to different phenotypes

between the explants and the spheroids. Therefore, the more natural mouse environment

for tumor growth, and the different tissue constituents, may provide markedly different

responses to the platinum therapy
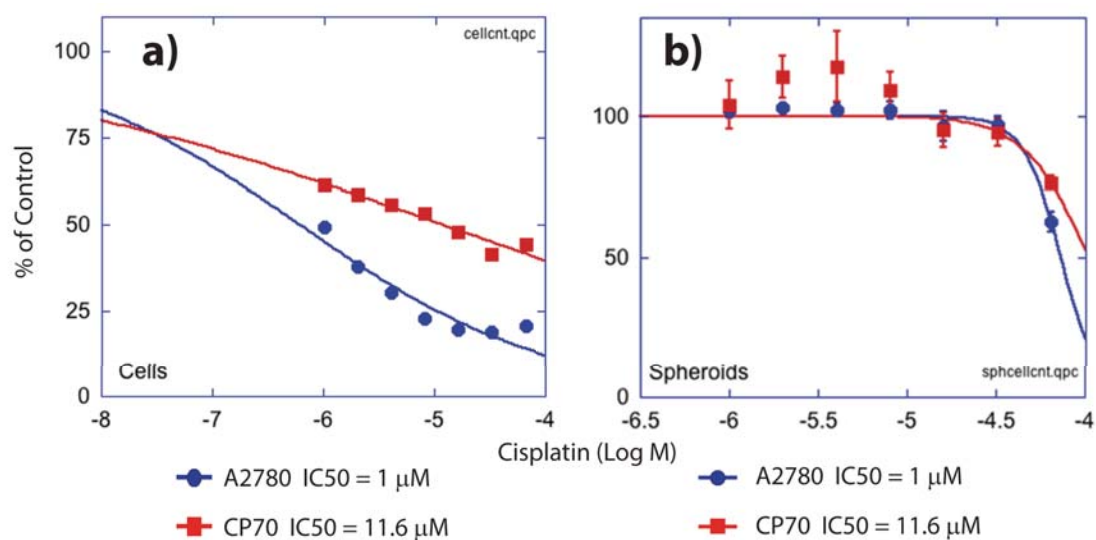
Figure 3.7. IC50s over 72 hours for a) 2D culture compared to b) 3D culture (tumor spheroids) from the same cell lines. The sensitive cell line is A2780, and the insensitive cell line is A2780/CP70 (CP70). The 3D spheroids have IC50 values approximately 10 times larger than for 2D. In the spheroids, both cell lines have high IC50s (72 μM and 104 μM) over 72 hours.

The sensitivity, specificity, and accuracy of the biodynamic chemoresponse assay

on murine xenograft biopsies were measured using a logistic regression on selected

biomarkers. The logistic values for each biopsy sample are shown in Figure 3.8.
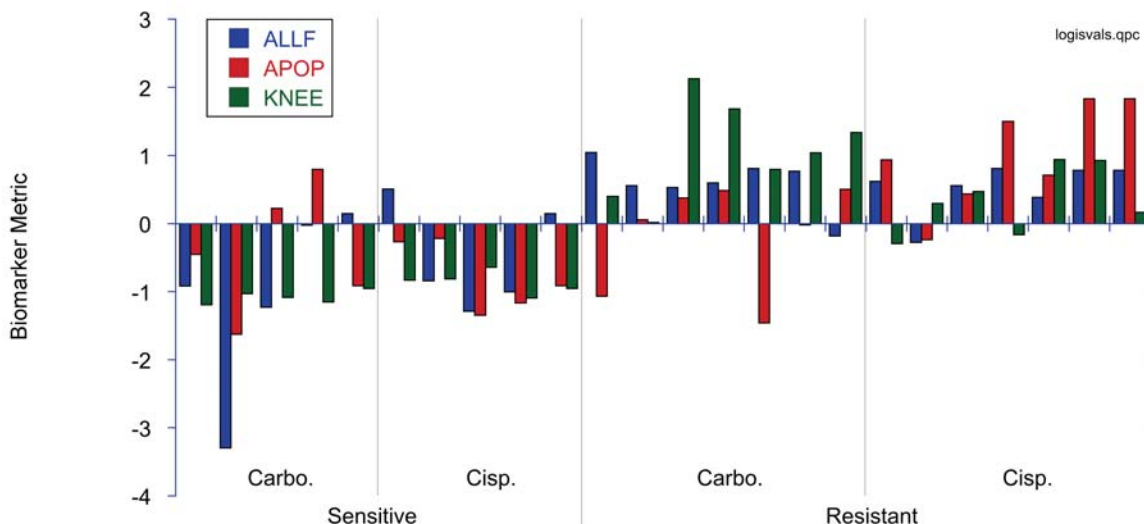
Figure 3.8. Values for three biodynamic biomarkers (ALLF, APOP and KNEE) measured across 24 samples. The samples are grouped as sensitive/carboplatin, sensitive/cisplatin, insensitive/cisplatin and insensitive/carboplatin. The ALLF biomarker measures overall inhibition in the drug-response spectrogram. The APOP biomarker is a nonlinear metric that correlates with apoptotic response. The KNEE biomarker is the knee frequency of the fluctuation spectral power.

By combining the three motility metrics in the multivariate logistic function, the combined group predicted chemotherapy response in 100% of cases using a binary classifier (response *vs*. non-response) that fully separated the two groups (Figure 3.9). To test for over-fitting of the data by the logistic predictor, a one-left-out (OLO) cross validation analysis was performed in which the logistic function was trained using 23 of the biopsies, holding one of the samples back that was subsequently tested in the predictor. This procedure was repeated for each of the 24 tumor fragments, and the results are shown in Figure 3.9 as the red bars. The performance of the OLO assay is almost identical to the full assay, with 100% separation between the two populations.

When the logistic prediction values were fit by continuous Gaussian distributions to generate a smooth a receiver-operator curve (ROC), the accuracy, sensitivity and specificity of the OLO analysis were all above 95%.
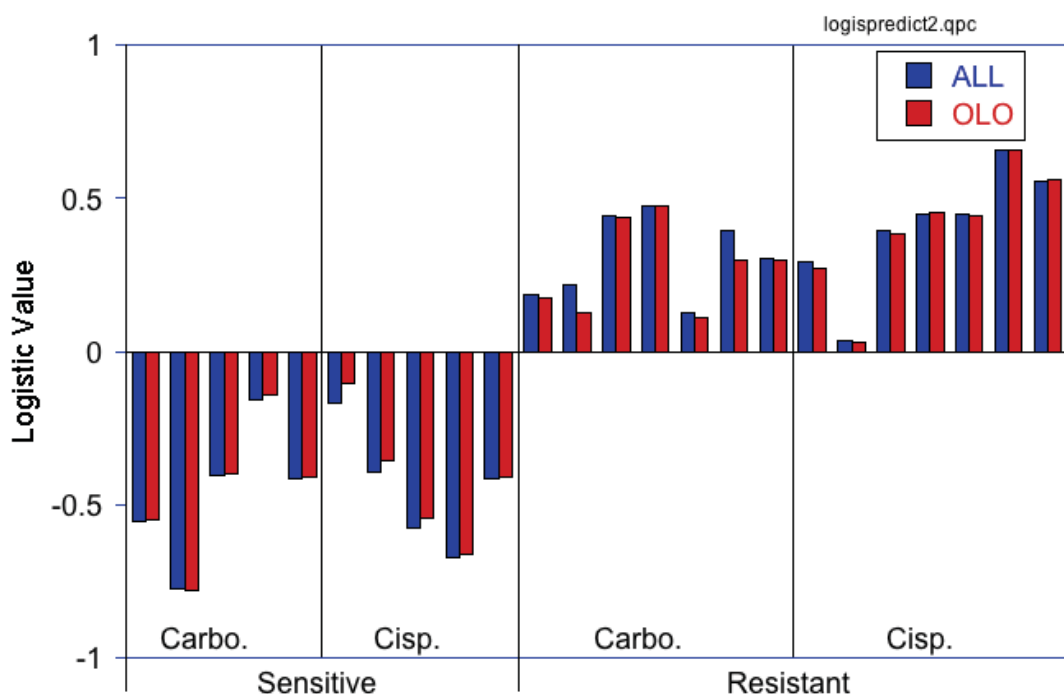
Figure 3.9. Logistic predictor model using selected biomarkers. The logistic predictor used three biomarkers (ALLF, APOP and KNEE) of 24 individual biopsy samples across sensitive (A2780) and resistant (A2780/CP70 and A2780cis) cell lines responding to 50 μM cisplatin (Cisp.) and carboplatin (Carbo.) treated ex vivo. Blue bars are results of training the logistic function with all samples. Red bars are results of the one-left-out (OLO) cross validation.

3.4.3   *In Vivo* Platinum Treatment Tested by *Ex Vivo* Re-exposure

The treatment of tumors *ex vivo* occurs in a very different environment compared to the more natural chemotherapy applied *in vivo* for which the drug is delivered to the tumor through the circulatory system of the mouse. To test the ability of biodynamic imaging to monitor tumor treatment in vivo, mice were treated with 50 mg/kg of carboplatin for varying periods of time before the mouse was sacrificed. The duration of the delay before sacrifice varied between 0 and 4 hours. The TDS response of the harvested tumor biopsies (with varying exposure time *in vivo*) was measured by further carboplatin (10 µM) treatment *in vitro*.

Response spectrograms of sensitive A2780 (Figure 3.10**a**) biopsies show expected sensitivity to carboplatin in the post-harvesting measurement, but the magnitude of the response decreases with increasing duration of pretreatment. The pretreatment of the tumors *in vivo* have an immediate inhibitory effect on the tumor tissue. Figure 3.10**b** shows the influence of pretreatment on initial sample motility. The NSD motility metric of biopsies from the insensitive A2780cis cell line remained essentially constant for different pretreatment times. However, the sensitive A2780 samples showed a decrease in initial NSD motility as pretreatment time increased. This demonstrates the sensitivity of biodynamic imaging to the state of health of the biopsies and the ability to measure, using *ex vivo* techniques, the patient response to therapy.
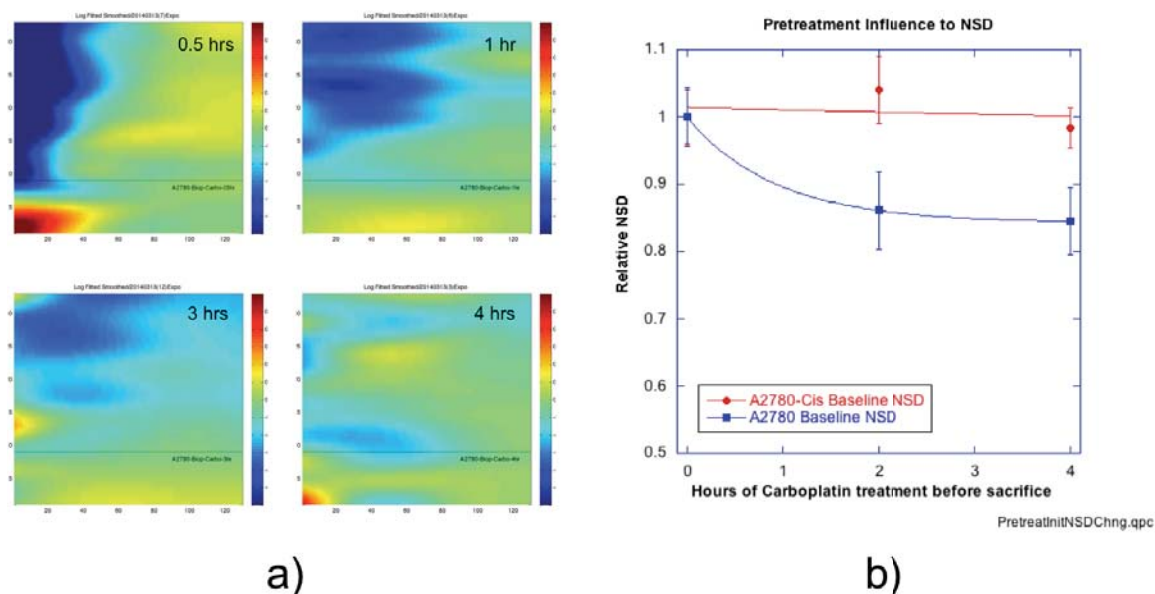
Figure 3.10. Response of A2780 xenograft biopsy to 10 µM carboplatin re-exposure *ex vivo* following carboplatin pretreatment. TDS drug response spectrograms show re-exposure for biopsies pretreated in vivo with 50 mg/kg carboplatin for 0.5 hr, 1 hr, 3 hr and 4 hr treatment. Xenograft fragments were then re-exposed during BDI assessment. a) Re-exposure of samples to carboplatin demonstrate low-frequency suppression, the amplitude of which correlated with decreasing time since initial treatment. The response to further treatment decreased with increasing pretreatment time. b) Effect of carboplatin pretreatment on sample health for sensitive (A2780) and insensitive (A2780cis) cell lines. Relative NSD is calculated by shifting the origin of the y-axis so that the average baseline NSD of the untreated samples for each day's experiment is unity. This reduces the systematic influences on average values and allows for comparison of experiments run on different days.

The drug-response spectrograms of Figure 3.10 were quantified by applying feature masks to the time-frequency spectrograms for feature extraction and quantification. Different feature masks correspond to different dynamical "biomarkers" or signatures of tissue response. One of the strongest biomarkers for chemotherapy response is the "dipole" feature mask that measures overall shift in spectral weight. A shift of spectral weight to lower frequencies constitutes metabolic inhibition and is captured by a positive dipole value. Another strong dynamical biomarker is

organelle/vesicle activity that appears near the Nyquist frequency. Enhanced organelle

activity has been associated with apoptotic processes [141]. The metabolic inhibition and

organelle activity biomarkers are plotted in Figure 3.11 as a function of the duration of

the *in vivo* treatment time. These values correspond to the response of the pretreated

tissues to an *in vitro* dose of platinum. Increasing treatments decrease this second

response. Tumors that have been degraded by treatment *in vivo* before surgery are less

healthy (reflected in the measured NSD values) and hence will not respond as strongly

because the tissue is less viable than untreated or more weakly-treated samples.
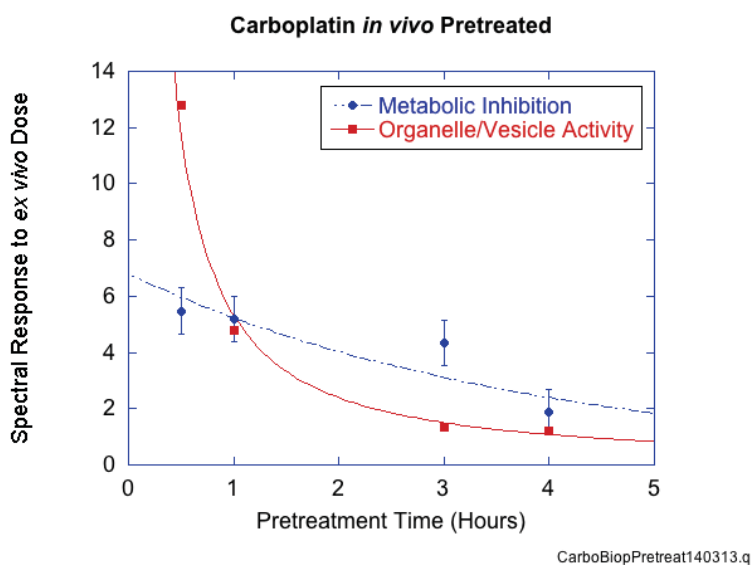
Figure 3.11. Spectral response to re-dosing. Spectral response measures average spectral change across masked spectrograms. Masks select for specific biological processes. Metabolic inhibition is the total average response (ALLF) while organelle/vesicle activity is the average of a dipole masked response (SDIP).

3.5   Discussion and Conclusion

Technologies that accurately assess the efficacy of chemotherapy could play a pivotal role in cancer care. The body is essentially a black box, opaque to most types of imaging, while for body-penetrating techniques (such as ultrasound or MRI), it allows only limited spatial resolution. Although the ultimate goal would be to observe, with microscopic resolution, cancer tissue responding to treatment in the patient in real time, imaging technology has not yet reached this stage. Compounding the difficulties of *in vivo* imaging are difficulties of finding specific biomarkers of treatment response. In many assessment techniques, tumor size reduction is the principal biomarker that provides a measure of the objective response to therapy. However, even if a therapy can kill most of a tumor, thereby providing a positive response measure, spatial heterogeneity in the tumor and its environment can prevent therapy from killing all of the cancer, which ultimately will relapse.

Biodynamic imaging may provide some solutions to this problem of therapy efficacy assessment. Although the BDI technology is not currently configured to image tissue *in vivo*, the next best thing is to measure fresh living tissue *ex vivo*. Excised living tissues can be maintained in a healthy state for more than a day by providing nutrients and oxygen to small tissue samples. The tissue inside the samples retain their essential 3D environment and microenvironment constituents (extracellular matrix, stromal tissue, etc.) and hence retain the ability to respond naturally to applied drugs. In this way, BDI approaches the ideal of measuring drug treatment efficacy *in situ*. The further challenge of specificity for biomarkers of assessment techniques is also provided by BDI. Biodynamic imaging is fundamentally a functional and mechanistic imaging modality.

The image contrast from Doppler light scattering arises entirely from changes in the physiology and mechanical motions induced by applied therapeutics. The altered dynamics of cells and tissues provides a direct measure of the mechanistic effects of the drug on the tissue. Furthermore, biodynamic imaging on small samples can measure spatial heterogeneity, isolating regions of tissue that have different responses, or that do not respond to the applied therapeutic. This capability of BDI could be potentially valuable for prediction of progression free times.

Chemotherapy response assays on *ex vivo* biopsies have two different applications in the clinic. These are therapy selection, and therapy monitoring. Therapy selection typically takes place after patient relapse when multiple salvage therapies are being evaluated. However, an application of growing utility in the clinic for chemoresponse assays is the selection of therapies even before first-line therapies and standard-of-care are selected. By personalizing therapy to the patient from the beginning of treatment, precious time would be saved for patients who do not respond to standard-of-care. The second application of biopsy-based chemoresponse assays for therapy monitoring is not typically as useful, because most patients do not undergo surgery during chemotherapy. However, for laboratory studies or preclincal trials, therapy monitoring of biopsies provides a valuable measure for drug development.

In this chapter, biodynamic imaging (BDI) was demonstrated for the first time in preclinical trials in the second application of therapy monitoring. Biopsies of sensitive and resistant tumor xenografts were tested for platinum sensitivity from *untreated* animals, as well as for platinum sensitivity from animals that *had* undergone initial treatment. Specific cell lines of human ovarian cancer were selected to control the

sensitivity/resistance of the tumor tissues to platinum. As expected, cell lines known to be sensitive to platinum produced tumor xenografts that were sensitive when tested as biopsies *ex vivo*, both with and without pretreatment in the mouse. Conversely, the cell line known to be resistant to platinum produced biopsy explants that were resistant to platinum in ex vivo treatments. BDI assessment of response vs. non-response using a multivariate logistic function resulted in 100% discrimination between known sensitive and resistant populations..

In contrast to this high-accuracy performance of the BDI chemoresponse assay on murine biopsies, the same assays run on tumor spheroids grown by both bioreactor and u-bottom plate techniques showed almost no differential response to platinum between the two cell lines. This null result on the *in vitro*-grown 3D tissue culture has important ramifications on several fronts. First, it highlights a potentially important difference between *in vitro* and *in vivo* tissue growth. These two environments are radically different and may induce the outgrowth of different clonal populations. Furthermore, the *in vivo* growth includes stromal cells and tissues that are missing from the *in vitro* culture. These different microenvironmental cues are known to lead to different gene expression and altered signaling pathways, which may contribute to the difference in the experimental responses to platinum. Second, the null results on the 3D tumor spheroids for cell lines with known sensitivity/resistance to platinum in 2D may highlight critical differences between 2D and 3D culture. It is clear that drug transport in 3D culture is different than for 2D monolayers, leading to EC50 values that can differ by an order of magnitude. The use of 3D culture for chemoresponse testing requires much higher concentrations, which consequently may induce off-target effects in the drug response.

These issues can confound interpretations and predictions from 3D culture assays. On the other hand, the biopsy explants do show the anticipated sensitivity/resistance to platinum that is predicted by 2D studies on these same cell lines.

Ultimately, it is the chemoresponse of tumor tissue *in vivo* that is most relevant for therapy monitoring. The differential response to platinum of the A2780 and CP70 explants demonstrates the unique utility of biodynamic imaging for chemoresponse testing in the relevant tissue environment. Furthermore, pretreatment with platinum of the mice *in vivo* prior to surgery had a clear effect on the BDI response on subsequent retreatment ex vivo, further demonstrating the utility of BDI for therapy monitoring under relevant environmental and tissue conditions.

CHAPTER 4. HETEROGENOUS RESPONSE TO PLATINUM IN METASTATIC
OVARIAN CANCER

4.1   Introduction

4.1.1   Multidrug resistance (MDR)

The development of drug resistance in cancer patients inhibits effective treatment

and decreases patient survival. Cisplatin and other platinum compounds have proved to

be effective at treating epithelial ovarian cancer, but have a high probability of inducing

drug resistance in treated patient cancers. In many cases, these tumors also exhibit

resistance to other standard-of-care therapies [130]. The origin of platinum resistance is

not well understood. Research shows that tumor microenvironment plays a significant

role [105, 142-144]. Since metastasis changes the microenvironment of tumor cells as

they travel to new areas of the body, metastatic tumors may also exhibit significant

changes in platinum sensitivity.

4.1.2   Tissue Structure and Mechanics

Animal tissue can be separated into four broad categories [145]. Mesenchymal

tissue is composed of fibroblast cells that form collagen fibers that make up cartilage,

bones, muscles, and blood vessels as well as other structural tissues. Epithelial cells are

specialized organ cells that make up the liver, skin, intestines, glands, etc. Haemato-

lymphoid cells comprise much of the immune system and include red and white blood

cells, lymphocites, and macrophages. Nervous system cells make up the brain, spinal

column, and nerves throughout the body. Figure 4.1 is an illustration of the how these

cells relate. Epithelial tissue is of particular importance in the study of cancer as over 90

percent of all cancer originates in the epithelium [83].
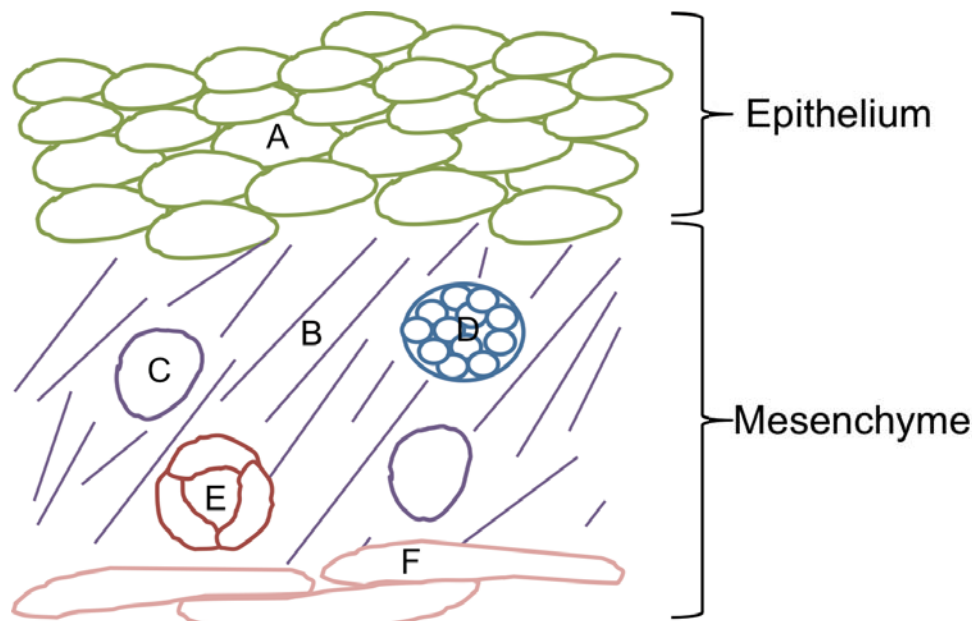
Figure 4.1. Illustration of tissue components. Epithelial cells (A) are supported by collagen fibers (B) generated by fibroblast cells (C). Running through the mesenchyme are nerve bundles (D) and blood vessels (E). Collagen fibers in regions such as the skin are supported by muscle cells (F).

4.1.3 Cancer

Cancer can be broadly defined as the invasive, proliferative growth of an aberrant

tissue. Normal tissue cells, exposed to a carcinogenic agent, mutate. Though mutation is

a normal and beneficiary process of evolution, many mutations result in dysfunction

within the cell and threaten survivability of the organism. Thus, regulatory mechanisms

induce the death of these cells. However, when a mutation suppresses or alters these

regulatory mechanisms, the cell can grow and proliferate without bound, turning into cancerous tissue that invades and overcrowds the surrounding tissue and can lead to death of the parent organism.

Cancer typically begins in the epithelium and follows three stages. During initiation, epithelial stem cells are exposed to carcinogenic agents. This exposure can be prolonged without tissue becoming cancerous. Individual cells affect the behavior of surrounding cells and the components of the interstitial environment, which gives rise to a field effect that precedes the formation of cancerous lesions and is an area of active research for early cancer detection [146].

Once a cell has mutated sufficiently to overcome limiting mechanisms, promotion leads to clonal expansion of the initiated cells within the local tissue. During this stage tumor lesions form within the surrounding epithelium, though such lesions may present little visual difference from normal epithelial cells. Promotion passes into proliferation, as the aberrant cells invade surrounding regions and penetrate into the mesenchyme.

4.1.4   Metastasis

Metastasis is the formation of cancerous bodies at some distance from the parent cells. Once cancerous cells progress beyond the epithelium where they originated, they begin to invade other organs through the mesenchyme. This can occur through direct growth of cancerous tissue, or through proliferation into the lymphatic system or the blood vessels. Once inside the lymphatic or blood vessels, cancer cells can detach from the parent tumor and be carried throughout the body.

Metastatic tumors present a mixture of parent and transplant environments. Tumor cells have genetic heritage from the parent epithelium from which they derived, but structural and chemical differences in the host location can alter expression and behavior. Thus, the phenotype of metastatic and primary tumors can vary. The primary way ovarian cancer spreads was thought to be continuous exposure of abdominal organs to free-floating tumour cells. However, there is evidence that metastasis to the peritoneal cavity may be carried through the blood [147]. The preferential host of metastatic ovarian cancer is the omentum. The omentum is a large fold of peritoneum that hangs down from the stomach and encloses the small intestines and other abdominal viscera. Nieman, et al. showed that the adipocyte-rich omentum provides a proliferative advantage and transfers fatty acids to ovarian cancer cells [148]. This chapter investigates the effect metastasis has on ovarian tumor sensitivity to cisplatin studied through biodynamic imaging.

4.2   Materials and Methods

4.2.1   Animal and Tissue Models

A2780 and SK-OV-3 (SKOV3) ovarian cancer cells were from Sigma. Xenografts were generated by Dr. Daniela Matei's laboratory through orthotopic implantation of 5×10^6 cells into the ovary of 6-7 week-old nude female BalbC mice. Xenografts formed and metastasized. Primary and metastatic tumors were harvested after 4-6 weeks. Harvested tumors were placed in ice cold media and were transported to Dr. John Turek's laboratory within 2 hours and prepared for imaging. Sample information is presented in Table 4.1.

Table 4.1. Outline of mouse experiments. Group g1 received a larger panel of drugs during testing than did other groups. Group g10 samples came from a mouse that was dying at the time of harvest. Sample was poor making data quality suspect. Response from g10 was not included in analysis.

A2780	SKOV3	Dates of experiments	Primary		Metastatic		Comments
			DMSO	Cisp	DMSO	Cisp	
	g1	2014.07.29 – 2014.08.02	5	3	7	6	3 mice, larger drug panel
g2		2015.03.03 – 2015.03.04	5	7	8	7	3 mice
	g3	2015.03.17 – 2015.03.19	7	4	6	8	3 mice
g4		2015.04.29 – 2015.04.30	6	6	8	9	2 mice
g5		2015.06.29 – 2015.06.30	7	2	6	6	4 mice
g6		2015.11.09 – 2015.11.10	10	9	4	4	1 mouse
g7		2015.11.11 – 2015.11.12	7	7	7	6	1 mouse
g8		2015.11.17 – 2015.11.18	6	7	8	7	1 mouse
	g9	2015.11.30 – 2015.12.01	8	3	7	6	1 mouse
g10		2015.12.02	4	4	2	2	1 mouse, dying, poor quality

4.2.2 Chemotherapy drugs

Cisplatin was obtained from Selleck Chemicals. Dimethyl sulfoxide (DMSO) came from Sigma-Aldrich. Cisplatin was prepared to twice the desired concentration to allow for later mixing inside the sample well. DMSO (0.1%) dissolved in growth medium was used as the negative control in all experiments. DMSO was selected because cisplatin is dissolved in DMSO before being added to growth medium to improve solubility.

4.2.3 Murine biopsies

Tumor biopsies were harvested from nude mice by Dr. Matei's lab. Biopsies were maintained at 4 °C for 5-48 hours before testing. Biopsies were sectioned using a razor blade to cut the tumor into pieces of approximately 1 mm^3 in volume. Pieces were affixed inside 96-well plates using a small drop of GLUture (Abbot Laboratories) and covered with agarose. Growth medium was added to each well. Experiments were performed immediately after plates were prepared.

4.2.4 OCI sequence

A diagram and explanation of the OCI system is shown in CHAPTER 1.5. OCI frames of each xenograft tumor section were captured in cycles every 40-48 minutes on average. Each capture sequence consisted of 15-45 seconds of travel time to allow the system to transition between tumors, followed by frame capture: 10 background frames captured at 10 frames per second (fps) with the reference beam not zero-path matched, then 50 frames at 0.5 fps and 500 frames at 25 fps with the reference beam zero-path matched.

Tumor sections were observed for 6 cycles (4.8 hours) to allow the samples to stabilize. Then half of the growth medium (~150 µL) was removed from each well and replaced with a drug at twice the intended concentration to limit disturbing the sample. Tumors were then observed for a further 12 cycles (9.6 hours).

4.2.5   Patient-derived xenografts (PDX)

Patient-derived xenograft tumors were supplied by Dr. Matei. Patient-derived xenografts are tumors cultured from biopsied patient cancer cells and grown in nude mice. Their genetic heritage is that of the derived patient cancer cells. It is unknown if and how the murine environment alters phenotypic response.

4.3   Results

4.3.1   Changes in platinum sensitivity of metastatic tumors

Samples from a single mouse group were tested over a two-day period. It was uncertain if biopsy samples would still be viable for testing after 24-48 hours post-operation. Figure 4.2 shows the distributions of initial NSD values for primary and metastatic samples for both A2780 and SKOV3 cell lines. Initial NSD values had considerable sample-to-sample variance, but there was no significant difference between the distributions for primary and metastatic samples. However, the initial condition of the sample showed no correlation with which day it was tested (Figure 4.3).
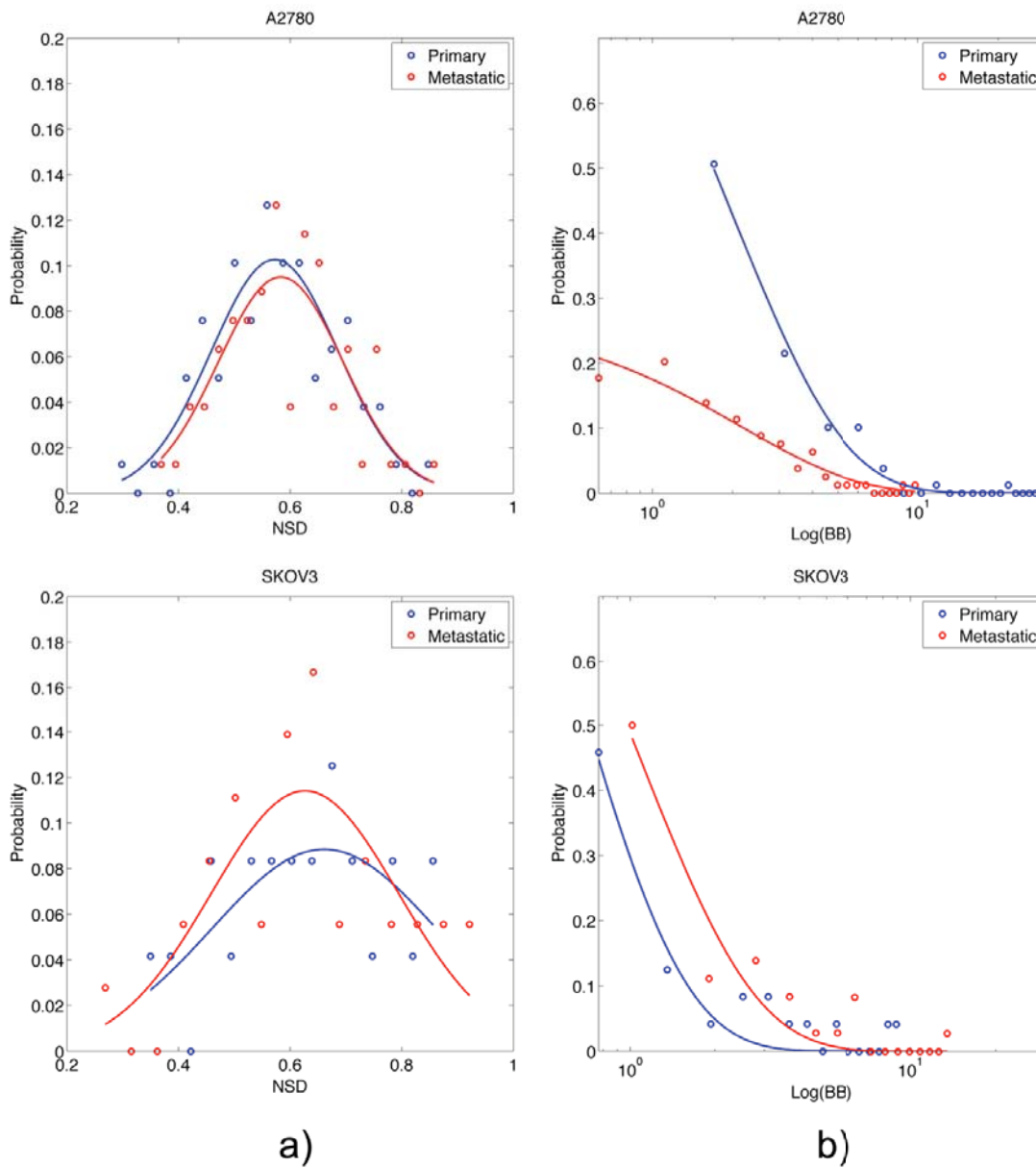
Figure 4.2. Distribution of initial a) NSD and b) backscatter brightness values of A2780 and SKOV3 biopsies.
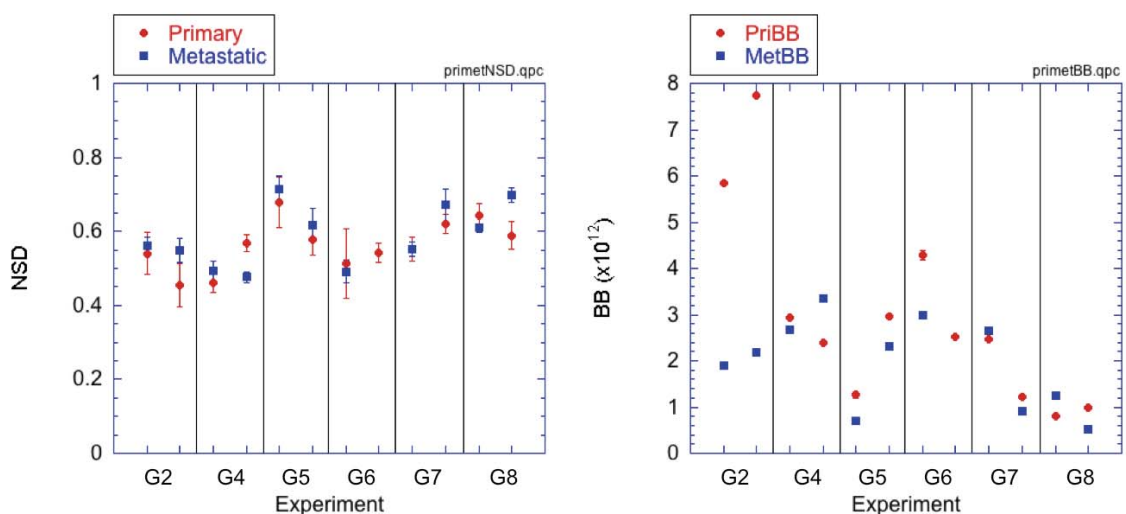
Figure 4.3. Comparison of initial sample NSD and backscatter brightness (BB) for ovarian injection biopsies. The first data point in each set corresponds to day 1 values and the second corresponds to day 2. Error bars represent standard error on the mean. There was variance in the NSD and BB from day 1 to day 2, but no systematic trend between days.

Response to cisplatin (25 μM) and to DMSO (0.1%) for each experimental group is shown in Figure 4.4. Samples exposed to the carrier (negative control) display a non-zero response that can be characterized as sample drift. The excision of samples from living hosts and subsequent transport, sample separation, and immobilization is likely to cause trauma to all samples. The response to the DMSO carrier can be considered a natural background to drug responses. The greater challenge is the wide variability of sample response among samples from the same host, that may represent spatial heterogeneity consisting of varying tissue constitution (stromal, epithelial, cancerous, etc.). This sample-to-sample variability complicates the interpretation of individual

group responses. However, response spectrograms generally demonstrated an enhancement in the low-frequency band up to 0.1 Hz for metastatic tumors over the primary tumor response.
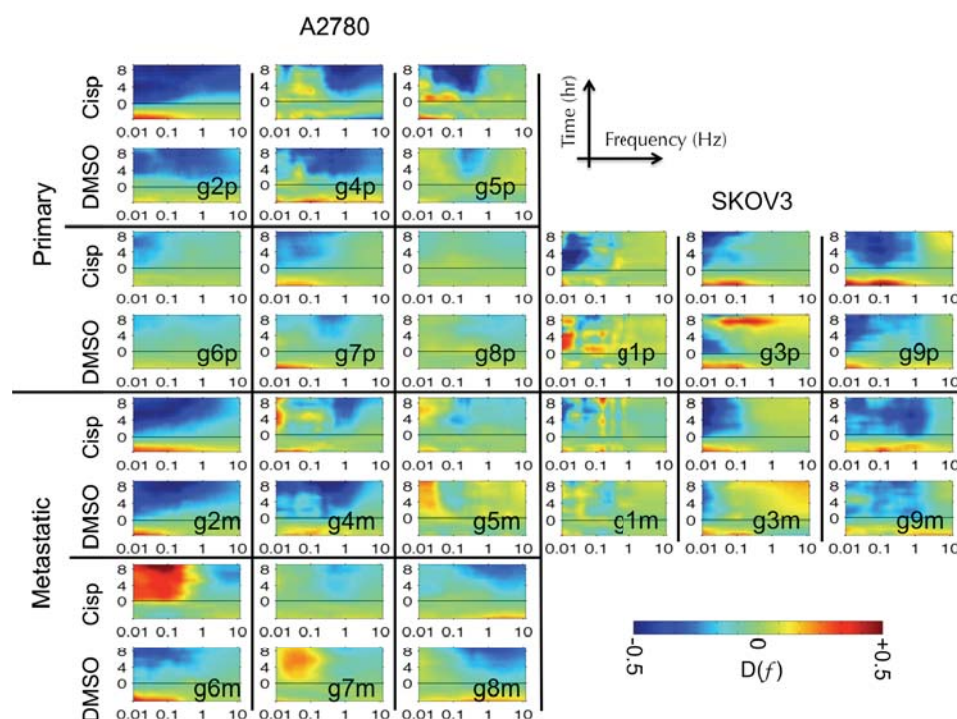
Figure 4.4. Average sample response for each experimental group. DMSO (0.1%) and cisplatin (25 μM) responses are shown for each group of samples, separated by cell line and sample type—primary or metastatic.

This enhancement is more easily seen in the average primary and metastatic responses shown in Figure 4.5. This enhancement was common for both A2780 and SKOV3 tumors, though the difference in response of A2780 tumors is stronger than for SKOV3.
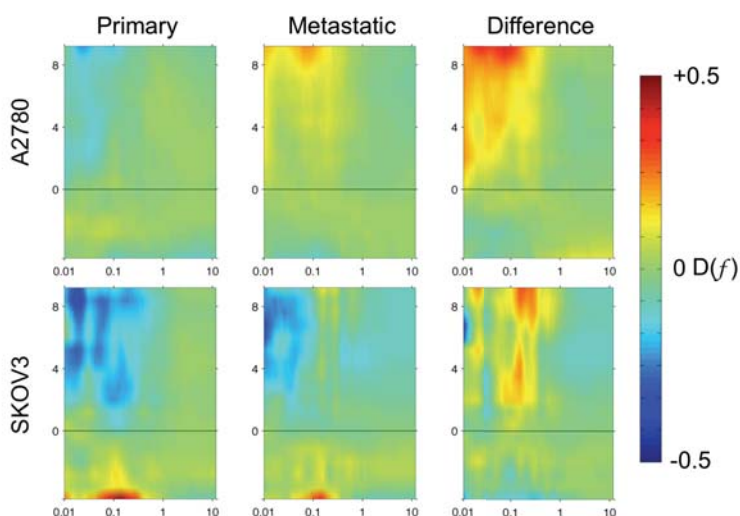
Figure 4.5. Average response to 25 μM cisplatin (DMSO subtracted). Response for primary and metastatic samples is shown for both A2780 and SKOV3 cell lines. DMSO response for each group has been subtracted prior to averaging. The difference between primary and metastatic responses is also shown.

Figure 4.6 compares the response to cisplatin of intraperitoneal (IP) and othotopically injected tumors. The more recent orthotopic A2780 tumors had weaker response to cisplatin than had the IP tumors reported in CHAPTER 3. The orthotopic SKOV3 tumors showed response to cisplatin. This was unexpected as the literature has classified SKOV3 as cisplatin-resistant. The cisplatin sensitivity may be due to genetic mutations in the established line since its sensitivity was first reported, or this may signify a change in phenotypic response due to the 3D environment.
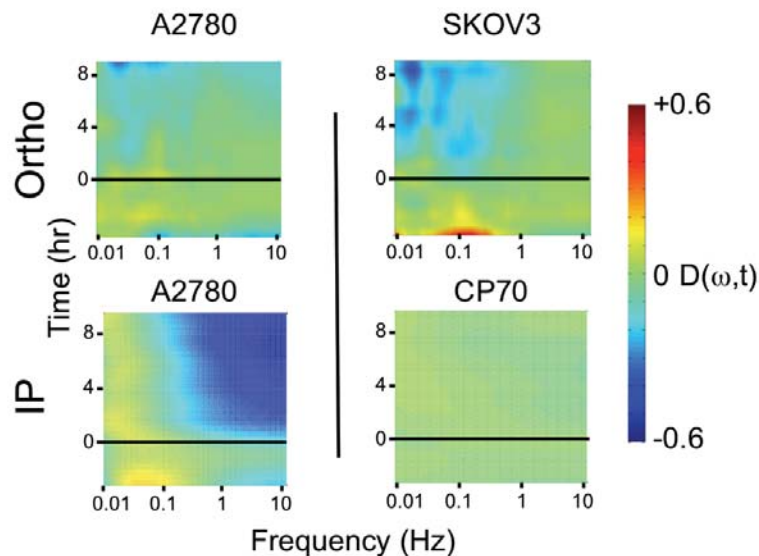
Figure 4.6. Comparison of ovarian tumor response (DMSO subtracted) to cisplatin. Intraperitoneal (IP) A2780 tumors exhibited a much stronger response to ciplatin than did the othotopically (Ortho) grown tumors. The SKOV3, which are classified in the literature as a resistant cell line, showed considerable response to cisplatin treatment.

Because tumor samples demonstrated a significant response to DMSO, it is important to account for systematic drifts in the population behavior that are not due to the application of cisplatin. Figure 4.7a shows the average response of all samples to any perturbation, DMSO or cisplatin. This response can be considered the average drift in population response as the experiment progressed through 9 hours of observation. The population drift was subtracted from each group response and the resulting average response for primary and metastatic tumors is shown in Figure 4.7b. Note that the enhancement below 0.1 Hz is still present.
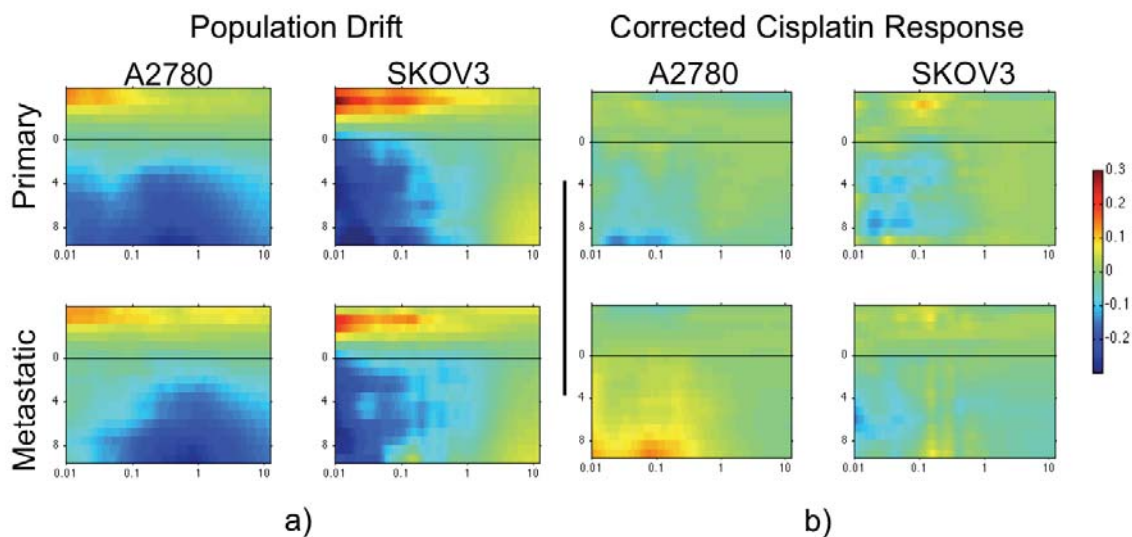
Figure 4.7. Correcting for sample population drift. a) Average response spectrograms of each population to any perturbation, DMSO or cisplatin, show drift in sample behavior due to natural degradation of the tissue. b) Spectrograms show average response for primary and metastatic tumors with the population response removed to correct for changes in sample behavior not due to application of cisplatin.

The change in logistic predictor values for each group using the response corrected for population drift maintains the trend of increased resistance in A2780 metastatic tumors (Figure 4.8). The SKOV3 tumors, however, show no strong trends in resistance change. These results are consistent with the DMSO-corrected response.
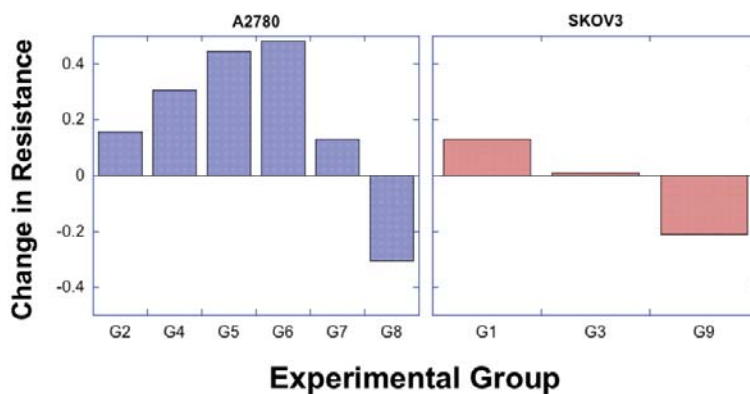
Figure 4.8. Change in resistance to platinum therapy between metastatic and primary tumors.

4.3.2 Patient-derived xenograft (PDX) response to cisplatin

Patient-derived xenografts (PDX) are an emerging *in vitro* 3D tumor model for culturing patient cancer cells in a laboratory environment. Preliminary to testing human ovarian patient biopsies, patient-derived murine-implanted tumors were assayed. Figure 4.9 shows the BDI response for one patient PDX.
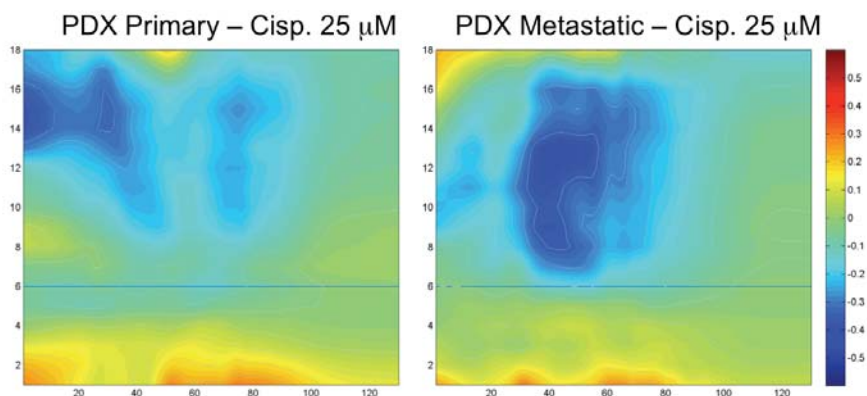
Figure 4.9. Average response spectrograms for primary and metastatic PDX tumors derived from single human patient. Metastatic samples showed stronger suppression in response to cisplatin (25 μM) than did primary samples.

The metastatic PDX for this patient showed greater suppression in the mid to low frequencies indicative of increased sensitivity to cisplatin verses the primary PDX samples. The primary sample still showed some sensitivity to cisplatin. Results correlated well with conventional sensitivity assay results supplied by Dr. Matei.

4.4   Discussion and Conclusion

Orthotopic tumor biopsies present distinct challenges over the *in vitro* tissue models our group has used in the past. These tumors present a more organic structure that includes many different cell types that are difficult to differentiate using current technologies. This led to a higher variance in sample response than was previously observed in other 3D tissue models. Current research is developing new methods to address response measurements of strongly heterogeneous tissue (see CHAPTER 5).

A2780 tumors exhibit greater change in sensitivity to cisplatin compared with SKOV3 tumors for metastatics versus primaries. Primary A2780 tumors in mouse groups 2, 4, 5, 6 and 7 showed sensitivity to cisplatin that decreased in the corresponding metastatic tumor samples. This decrease was present even when the metastatic tumors exhibited a sensitive response. Decrease in sensitivity suggests that metastatic cells may have developed better mechanisms for resisting and repairing cisplatin damage. Curiously, sample group 8 showed little response in the primary tumors. The metastatic tumors of that same group had a sensitive response. It is unclear why this particular mouse group would present an opposite trend. However, when corrected for baseline drift, neither the primary nor the metastatic tumors showed strong response.

The SKOV3 tumors, in general, showed sensitivity to cisplatin. This differs from publish cisplatin sensitivity assessed using 2D assays [149]. The change in sensitivity between primary and metastatic SKOV3 tumors in smaller than that of the A2780 tumors, suggesting that metastatic SKOV3 cells retain greater phenotypic similarity to the parent tumor cells. Both SKOV3 and A2780 metastatic tumors showed enhancement in their response below 0.1 Hz, indicating a common mechanism of cisplatin resistance.

The PDX sample had an effect opposite that shown by the established cell lines, with metastasis displaying increased sensitivity to cisplatin therapy. This result raises questions about the validity of established cell lines as accurate models for drug therapy development. Patient cancers may be more chaotic than current development protocols assume, which would be a major factor in drug failure during clinical trials. The unexpected sensitivity of SKOV3 tumors suggests that clonal variations may have entered into the established cell line that would alter their behavior from that of the original patient source. However, more PDX tumor experiments are needed to confirm these hypotheses.

CHAPTER 5. TISSUE DYNAMICS SPECTROSCOPIC IMAGING (TDSI)

5.1   Abstract

Spectrograms generated by tissue dynamic spectroscopy (TDS) indicate average cell behavior across the entire sample tissue. When tissue is strongly homogenous, the average cell behavior closely matches individual cell behavior. However, when tissue has heterogeneous structure, TDS spectrograms combine the different cellular responses, producing an average that may differ from the local tissue responses in certain regions of the sample. In patient biopsy tissue—where samples contain varying amounts of cancerous cells, normal organ cells, and structural tissues—regional differences in tissue response can be large. A method for assessing the heterogeneity of response within a sample is needed. This chapter discusses the development of tissue dynamics spectroscopic imaging (TDSI), an imaging modality that applies TDS on a voxel-by-voxel basis across the sample to map differences in regional tissue response. It also presents early work looking at regional differences in tissue response that might confound or invalidate predictions of patient outcome from tested biopsies.

5.2   Introduction

Correct identification of tissue response is critical if BDI is to achieve clinical utility. The complexity of cancer biopsies confounds current predictive capabilities of

BDI, increasing error and misdiagnosis. As shown in Figure 5.1, *ex vivo* tissue, whether it is murine xenografts or patient biopsies, is comprised of several different cell types. Cancerous cells, normal organ cells, structural components, and blood vessels are all bound together. Without employing other imaging techniques, it is often difficult for OCI, MCI, or TDS modalities to determine cell type. However, each cell type may contribute differently to the measured sample response, confounding assessments. Even different cancerous cells may respond differently with parts of the tumor exhibiting a sensitive phenotype while other parts are resistant to applied therapeutics. BDI must develop an imaging modality that can address the heterogeneity present in *ex vivo* tissue samples.
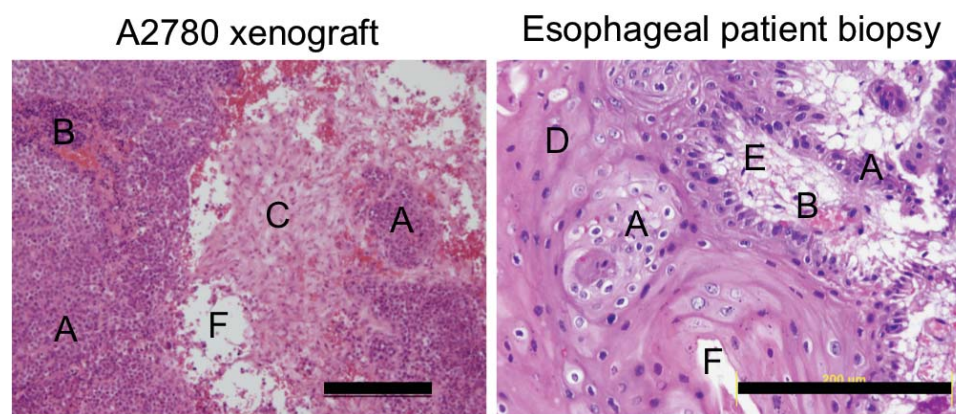
Figure 5.1. Histology images of stained biopsy tissue samples. Histology shows that biopsy samples are comprised of several different cell types and structures including: (A) cancer cells, (B) blood vessels, (C) stromal tissue, (D) normal organ cells, and (E) mucin. White regions (F) are artifacts of the staining typical of tears in the tissue. Bars are 200 μm.

To this end, tissue dynamics spectroscopic imaging (TDSI) is an extension of TDS that uses different biodynamic response features as the imaging contrast. It is a form of functional imaging [34, 47, 150] that helps detect regional differences in response behavior within a sample.

5.2.1 Early TDSI

TDSI has been developing since the start of biodynamic imaging. In early tumor spheroid experiments, Jeong, *et al.* [14] noted that MCI images of large UMR-106 spheroids showed a low-motility region in the center (Figure 5.2). This corresponded to cells in the center of the spheroid being starved for nutrients, which caused them to undergo necrosis. Jeong found that sectioning the OCI images into "shell" and "core" regions during BDI analysis resulted in spectrograms that often showed differences in tissue response between the two regions. There was, however, no standardized method for determining which parts of the image were shell regions and which parts were core region, so sectioning was chosen by the operator. Furthermore, BDI analysis algorithms only accepted circular or elliptical masks for sectioning. While working with cell lines that formed tight spheres, such as UMR-106 or HT-29, circular masks were sufficient, but once projects involved biopsied tissue or cell lines that didn't form spheres in the bioreactor, such as MIA-PaCa-2, more complicated sectioning geometries were needed. As biopsies and MIA-PaCa-2 tumor spheroids lacked the nutrient-starved central region, shell-core sectioning no longer made sense and was abandoned.
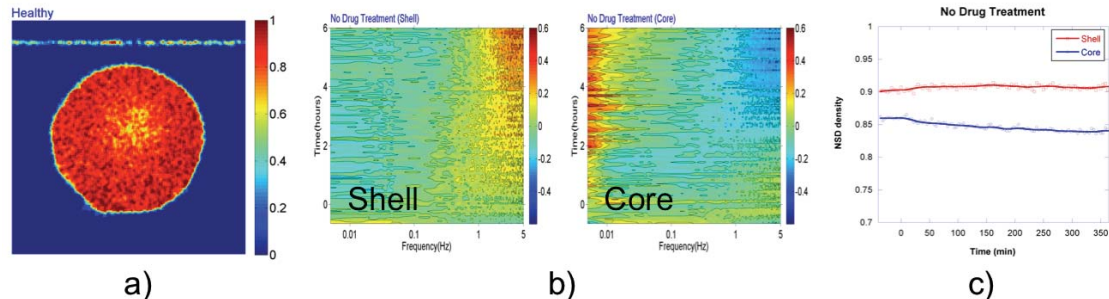
Figure 5.2. Differences in shell-core response measured by BDI. MCI images (a) of large UMR-106 tumor spheroids often exhibited central, low-motility regions. These central "core" regions showed different response to treatment (b) from the outer "shell" region of the spheroid as well as different changes in motility (c).

Several attempts at functional imaging of heterogeneous tissue have occurred since those early experiments. A2780 and A2780/CP70-GFP (CP70-GFP) cell lines showed distinctly different average motilities. When co-cultured in the same bioreactor, tumor spheroids would form as aggregates of the two cell lines with each cell type preferentially clustering with itself. This lead to spheroids with distinct regions comprised of A2780 and CP70-GFP cells. MCI images of co-cultured spheroids showed regions of high and low motility that corresponded to CP70-GFP and A2780 cell regions, respectively, as confirmed by fluorescence imaging (Figure 5.3). However, the high resistance of A2780 and CP70-GFP tumor spheroids to platinum compounds (see CHAPTER 3) made determining differences in drug response between tissue regions uncertain.
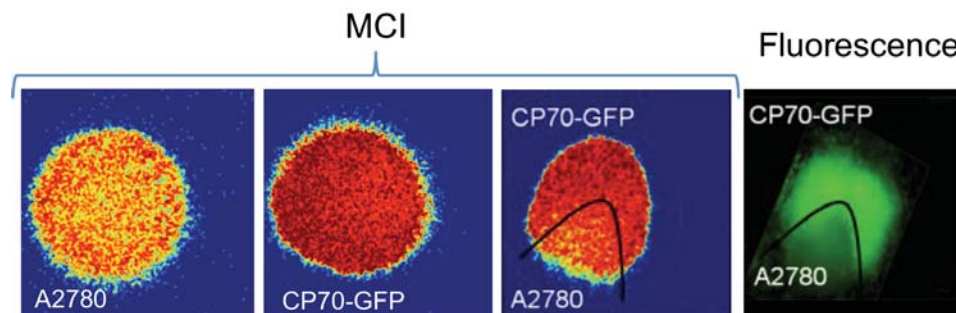
Figure 5.3. MCI and fluorescence images of A2780 and A2780/CP70-GFP co-culture spheroid. A2780 spheroids had distinctly lower motility than spheroids of A2780/CP70-GFP (CP70-GFP) cells. This difference in motility is evident in the co-cultured spheroids due to preferential segregation between the two cell lines. Motility determination of cell type in the MCI image was confirmed by fluorescence imaging.

More recently, researchers in our group generated functional images of spheroid and biopsy samples (Figure 5.4) [151]. This involved separating the OCI capture sequence into 2 pixels by 2 pixels regions and generating a response spectrogram for each region. The operator then selected a mask and threshold value based on features observed in the spectrograms to determine similarity of response. Unfortunately, this method required the operator to inspect each spectrogram individually, 15625 spectrograms for a standard 250 pixels by 250 pixels OCI image, and subjectively selecting the different features. No standard feature masks were available.
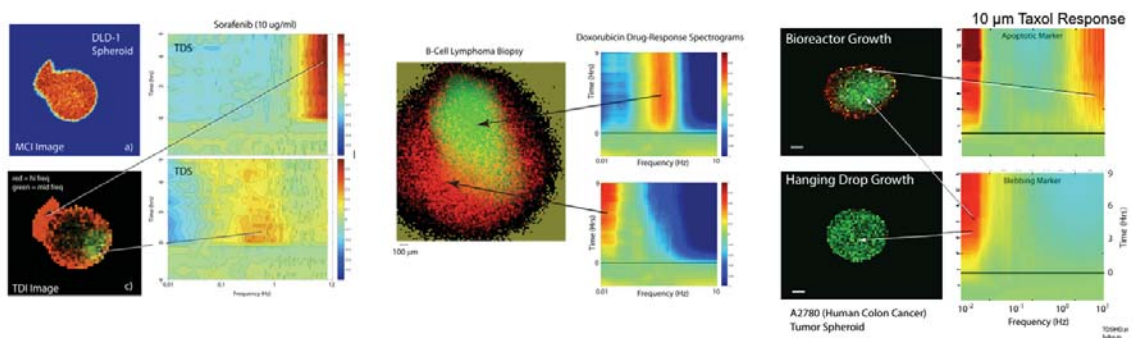
Figure 5.4. Functional images of selected spheroid and biopsy samples.

For TDSI to become a practical imaging mode, a scriptable, standardized technique was needed to select tissue response features. Feature vectors, as a way of condensing sample condition and response information, are a natural method for mapping regional responses within a tissue sample. The standardized biomarkers recently adopted into BDI analysis protocol remove operator subjectivity and allow TDSI to be part of already existing BDI sample processing.

5.3   Current Methodology

5.3.1   Micro-spectrograms

Micro-spectrograms are generated in a manner similar to traditional TDS (macro-) spectrograms (see CHAPTER 1.7), but the average spectra comprise response information from a few pixels instead of the entire OCI image. A series of OCI images is acquired and divided into regions of regular pixel size. The region size determines the granularity of the TDSI image. An imaging target can be treated as a diffraction grating with spatial period Λ. For an N pixels by N pixels CCD chip of finite dimension, the

maximum spatial frequency ν_{max} captured at the Fourier plane constrains the minimum resolvable feature,

$$\nu_{max} = {}^{1}\!/\!_{\Lambda_{min}} \qquad\qquad 5.1$$

with a frequency grating spacing on the CCD of

$$\Delta\nu = \frac{2\,\nu_{max}}{N} = \frac{2}{N\,\Lambda_{min}} \qquad\qquad 5.2$$

The field of view of the reconstructed image L relates to the grating spacing as

$$L = \frac{1}{\Delta\nu} = \frac{N\,\Lambda_{min}}{2} \qquad\qquad 5.3$$

which gives a the reconstructed image a pixel size p of

$$p = \frac{L}{N} = \frac{\Lambda_{min}}{2} \qquad\qquad 5.4$$

This means that TDSI requires a minimum pixel size of 2 by 2 averaged OCI pixels to avoid oversampling the dynamic speckle.

Once the OCI series is divided into pixel groups, normal TDS analysis occurs for each pixel during each image capture sequence in the series. For an OCI image of N by N pixels, this results in a TDSI image of N/2 by N/2 pixels with each pixel having an associated backscatter brightness, NSD, and average fluctuation spectrum at each capture time. A spectrogram for each pixel is generated by comparing the fluctuation spectrum at each time to the sample average baseline power spectrum. Note that this baseline power spectrum is averaged across the entire sample, which modifies the interpretation of the micro-spectrograms to show how tissue behavior within a TDSI pixel compares to the average untreated tissue behavior of the entire sample. Using biomarker analysis, (see

CHAPTER 1.8) the BDI output of each TDSI pixel generates a feature vector that

encapsulates the condition and response of the imaged tissue within that pixel. Figure 5.5

presents an illustration of the analysis flow.
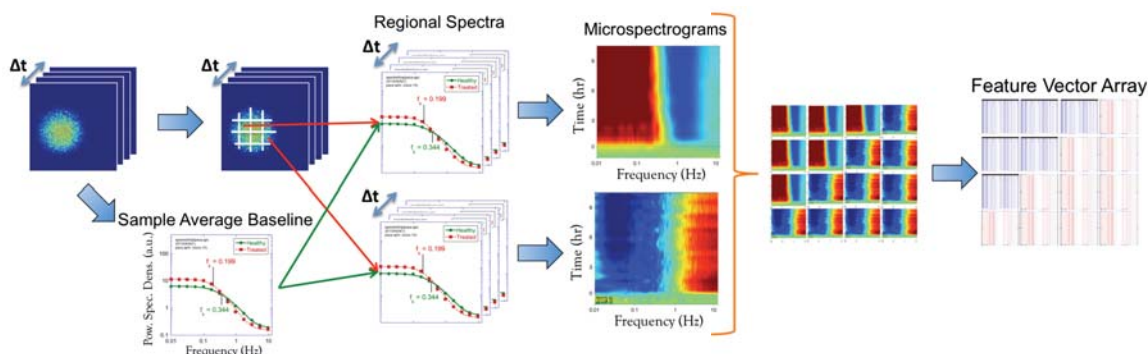
Figure 5.5. Illustration of TDSI image generation.

5.3.2   Biomarker Maps and RGMerge

Selected biomarkers are used as contrast agent to generate biomarker maps

(Figure 5.6) that show regional differences in response amplitude for that biomarker.

Individual maps are combined using a custom Matlab function called rgmerge.m that

assigns one biomarker to the red value and another biomarker to the green value in a red-

green-blue (RGB) color space. The result is an image (Figure 5.6) where the color of

each pixel indicates how well the two biomarker maps overlap and color saturation

indicates the strength of each biomarker. Pixels look more red where the green-assigned

biomarker has small values and look greener where the red-assigned biomarker has small

values. Where both biomarkers have large values the resulting pixel looks yellow, and

where both biomarkers have small values, the pixel has low color saturation and looks

black.
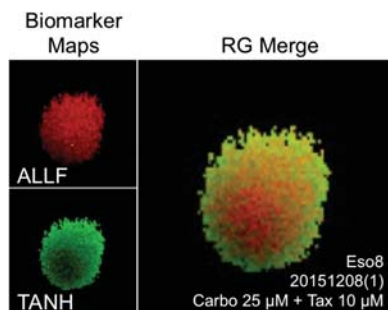
Figure 5.6. Individual and merged biomarker maps of esophageal biopsy sample responding to carboplatin (25 μM) plus taxol (10 μM) combination therapy. Maps use the values of ALLF and TANH biomarkers. The merged image shows three regions with distinct response behavior: a central red region surrounded by a yellow region where both biomarkers overlap, and a small green region in the lower left of the image.

Comparing two biomarkers of vastly different amplitudes resulted in merged TDSI images dominated by the biomarker with the largest value. However, it was desirable to preserve some measure of the relative strength of biomarker, especially those relating to features of the spectrograms. For this reason, conditional biomarker values (see CHAPTER 1.8) are scaled so that the largest negative value of each is -1 and the largest positive value is 1. Response biomarkers are scaled together so that the largest negative value of all biomarkers is -1 and the largest positive value is 1. Scaling maintains relative distance from zero so that values close to zero remain close to zero.

Because rgmerge.m uses RGB color space, all values must be positive, which divides the biomarker space into positive and negative groups. Representing the different possible combinations of positive and negative values for each pair of 82 biomarkers is challenging (Figure 5.7) and further research is required to devise a method that is both information-rich and easily understandable.
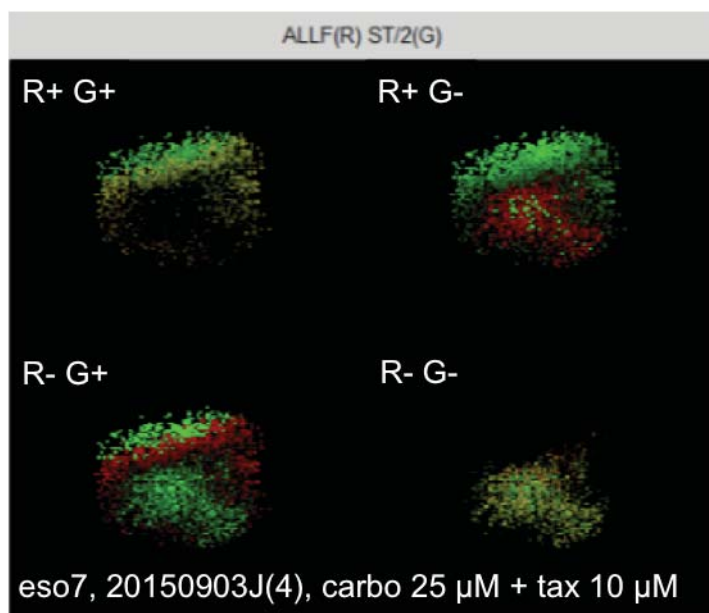
Figure 5.7. Example TDSI images of positive- and negative-value space combinations for two biomarkers. Biomarker values are from an esophageal patient biopsy sample responding to carboplatin (25 μM) plus taxol (10 μM) combination therapy.

5.4   Results

5.4.1   Heterogeneity of tissue response for a single esophageal patient

TDSI provides BDI a systematic method for visualizing the amount of heterogeneity present in a patient's tumor. Figure 5.8 shows TDSI images for positive and negative biomarker combinations of nine selected biomarkers. Color can be indicative of heterogeneous response, but because the data include positive and negative values, of particular importance are changes in shape between the different images.
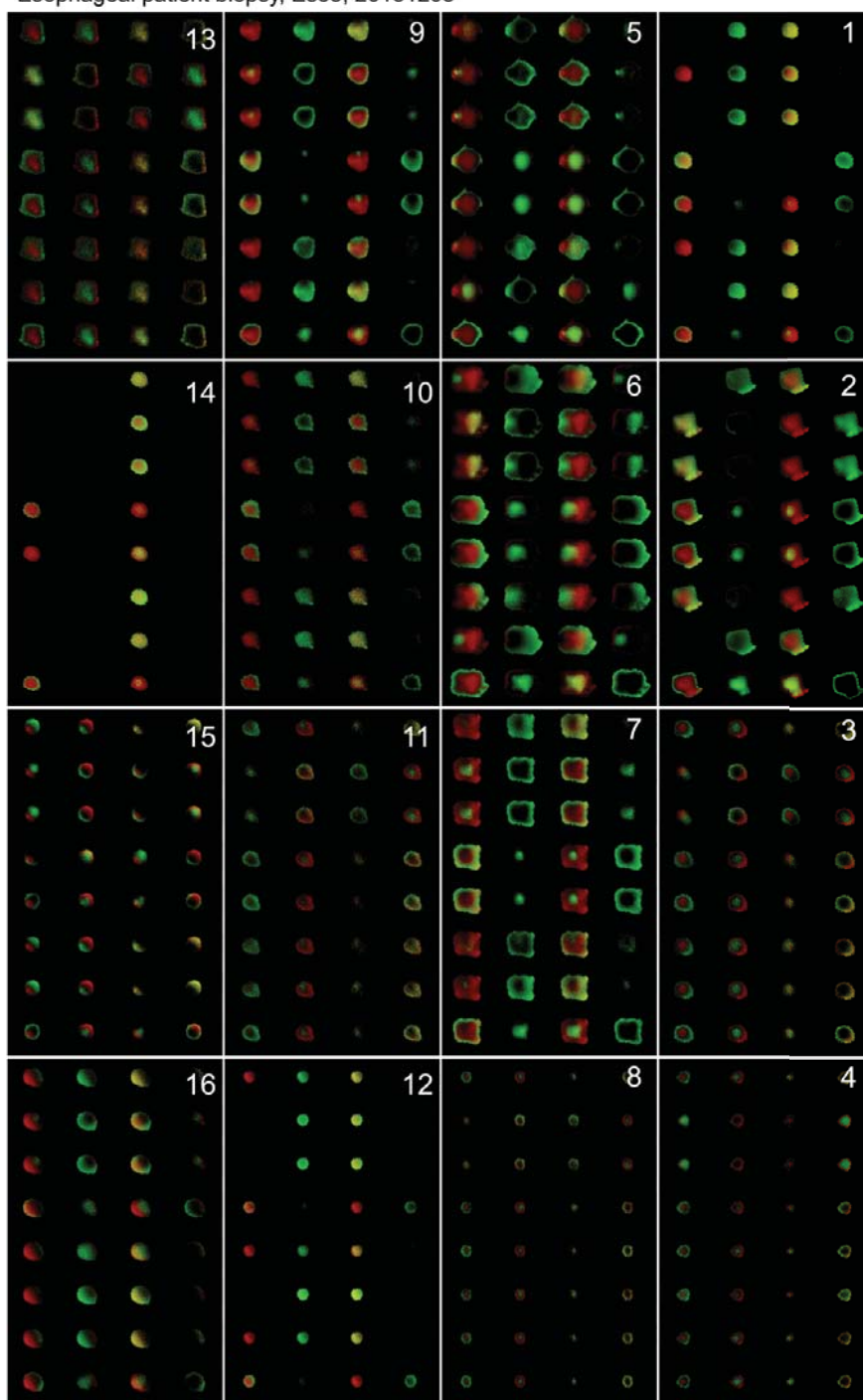
Figure 5.8. TDSI images for sample from a single esophageal biopsy patient. ALLF (red) is compared against (green, from top to bottom) ST/2, TANH, SDIP, QDIP, Q3T/2, LOF, MID, and HIF. Columns are positive- and negative-space combinations of each biomarker: (from right to left) positive red, positive green; negative red, negative green; positive red, negative green; negative red, positive green.

We can classify patient sample heterogeneity by size and distinctness of regions into strong, moderate, and weak groups. Samples 2, 5, 6, 7, 9, 13, and 15 show large, easily separable regions of different response and would be classified as strongly heterogeneous. Samples 1, 3, 10, 11, and 16 show large bands of color, but those bands tend to be harder to separate and are classified as moderately heterogeneous. The remaining samples (4, 8, 12, and 14) show overlapping biomarker masks, or they exhibited generally weaker response and would be classified as weakly heterogeneous. Though subjective, this classification indicates that 75% of this patient's samples exhibit strong to moderate heterogeneity. Image segmentation methods are needed to make a more systematic assessment.

5.4.2   Comparison of micro-spectrograms to macro-spectrogram

TDSI shows differences in response that are masked in the macro-spectrogram and other BDI output. These differences would confound response predictions and could lead to misapplication of chemotherapeutics, developments of drug-resistance, or later patient relapse. Figure 5.9 shows BDI results for one esophageal patient biopsy sample responding to cisplatin (25 μM) plus fluorouracil (5fu, 25 μM) combination therapy.
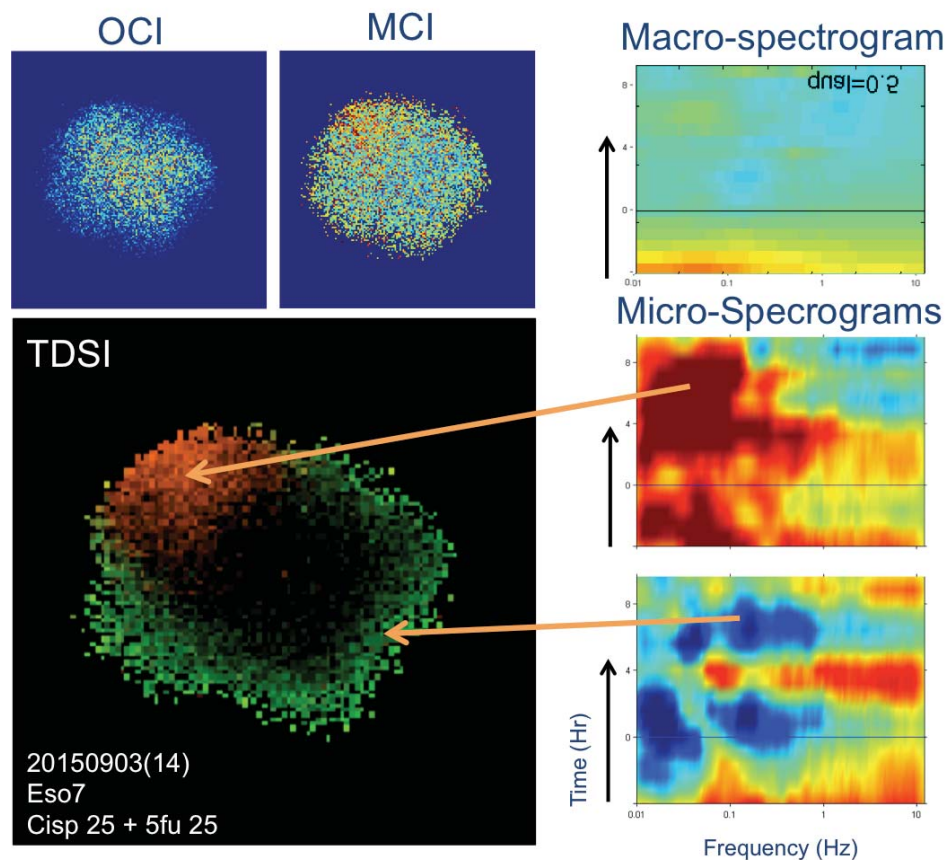
Figure 5.9. BDI results for esophageal patient biopsy sample. OCI and MCI images correspond to final observation of the sample following application of cisplatin (25 μM) plus fluorouracil (5fu, 25 μM) combination therapy. The macro-spectrogram shows mild response to therapy. The TDSI image has three regions: a central dark region, a green halo, and a red nodule in the upper left. Micro-spectrograms for the three regions indicate that the green region experienced suppression in the low frequencies in response to therapy, while the red region experienced an enhancement. The dark region (micro-spectrogram not shown) showed a response similar to that indicated by the macro-spectrogram.

The OCI image for this sample shows no distinct tissue structures and is typical of biopsy samples. The MCI image has a slight increase in motility visible in the upper right suggesting heterogeneous behavior, but the extent of the region is unclear. The macro-spectrogram for this sample shows a slight overall suppression indicative of mild response to the therapy. From the TDSI image of this sample, however, one can

determine the size of the higher-motility region at the top-left of the MCI image. TDSI also shows three regions within this sample. When the micro-spectrogram of each region was plotted, the red region showed enhancement in the low- and mid-frequencies indicative of resistance to therapy, while the outer green region had suppression in those same frequency ranges, suggesting that a portion of the sample was more strongly responsive to therapy. The central dark region had a micro-spectrogram similar to that of the macro-spectrogram. When averaged during traditional TDS analysis, the responsive and resistive regional behaviors cancel out. Therefore, while the macro-spectrogram would indicate mild response to therapy, portions of the patient's cancer may be resistant and presage relapse and the development of completely a resistive cancer strain.

5.5   Discussion and Conclusion

Improvements in TDSI calculation allow for faster image generation, systematic biomarker selection, and lower operation interaction. The analysis flow is complimentary to existing analysis methods, which saves computational time and data storage space. More research is needed, however, to find the best method for representing the information gained.

Though only one experiment's complete sample set is presented in this chapter, examples of heterogeneous response in TDSI images were not scarce among the sample sets processed so far. Continuing research will develop objective methods for assessing sample heterogeneity and quantifying the amount of heterogeneous tissue present in a

patient's biopsy. Also, the addition of traditional imaging methods would illuminate the cause of heterogeneous response and help the project determine which biomarker combinations best differentiate tissue type.

TDSI brings functional imaging to BDI analysis and opens new avenues of inquiry into how heterogeneous response may affect long-term patient survival. Issues of representation and data compression must be addressed before the technique can be broadly applied to chemotherapeutic response tests. However, initial results on esophageal patient biopsies are promising and indicate that heterogeneous structure is common and must be addressed for BDI to achieve better predictive capabilities.

LIST OF REFERENCES

LIST OF REFERENCES

1.   An R, Merrill D, Avramova L, Sturgis J, Tsiper M, Robinson JP, et al. Phenotypic Profiling of Raf Inhibitors and Mitochondrial Toxicity in 3D Tissue Using Biodynamic Imaging. Journal Of Biomolecular Screening. 2014;19(4):526-37. doi: 10.1177/1087057113516674.

2.   Nolte D, An R, Jeong K, Turek J, Caulfield H, Arsenault H. Digital Holography and Tissue Dynamics Spectroscopy: On the Road to High-Content Drug Discovery. Tribute To Joseph W Goodman. 2011;8122. doi: 10.1117/12.896618. PubMed PMID: WOS:000295774600019.

3.   Merrill D, An R, Sun H, Yakubov B, Matei D, Turek J, et al. Intracellular Doppler Signatures of Platinum Sensitivity Captured by Biodynamic Profiling in Ovarian Xenografts. Scientific Reports. 2016;6.

4.   An R, Wang C, Turek J, Machaty Z, Nolte DD. Biodynamic imaging of live porcine oocytes, zygotes and blastocysts for viability assessment in assisted reproductive technologies. Biomedical Optics Express. 2015;6(3):963-76.

5.   Nolte D, Turek J, An R. Biodynamic imaging for artificial reproductive technology. Molecular Reproduction and Development. 2015;82(7-8):500.

6.   Nolte DD, An R, Childress M, Turek J. Biodynamic 3D Imaging for Personalized Cancer Care. CLEO: 2014: Optical Society of America; 2014.

7.   Jeong K, Peng L, Turek JJ, Melloch MR, Nolte DD. Fourier-domain holographic optical coherence imaging of tumor spheroids and mouse eye. Applied Optics, Vol 44, Issue 10, pp 1798-1805. 2005. doi: doi:10.1364/AO.44.001798.

8.   D. Huang EAS, C. P. Lin, J. S. Schuman, W. G. Stinson, W. Chang, M. R. Hee, T. Flotte, K. Gregory, C. A. Puliafto, and J. G. Fujimoto, "," Science, vol. 254, pp. 1178-1181, 1991. Optical Coherence Tomography. Science. 1991;254(5035):1178-81.

9.   Fercher AF, Drexler W, Hitzenberger CK, Lasser T. Optical coherence tomography - principles and applications. Reports On Progress In Physics. 2003;66(2):239-303. PubMed PMID: ISI:000181513100004.

10.   Fujimoto JG. Optical coherence tomography for ultrahigh resolution in vivo imaging. Nature Biotechnology. 2003;21:1361-7.

11.   Schmitt JM. Optical coherence tomography (OCT): A review. *IEEE Journal of Selected Topics in Quantum Electronics*. 1999;5:1205-15.

12.   Tomlins PH, Wang RK. Theory, developments and applications of optical coherence tomography. J Phys D: Appl Phys. 2005;38(2519). doi: doi:10.1088/0022-3727/38/15/002.

13.   Jeong K, Turek JJ, Nolte DD. Volumetric motility-contrast imaging of tissue response to cytoskeletal anti-cancer drugs. Opt Express. 2007;15(21):14057-64. Epub 2007/10/17. PubMed PMID: 19550678.

14.   Jeong K, Turek JJ, Nolte DD. Speckle fluctuation spectroscopy of intracellular motion in living tissue using coherence-domain digital holography. J Biomed Opt. 2010;15(3):030514. Epub 2010/07/10. doi: 10.1117/1.3456369. PubMed PMID: 20614997.

15.   Sutherland RM. Cell and environment interactions in tumor microregions - The multicell spheroid model. Science. 1988;240(4849):177-84. doi: 10.1126/science.2451290. PubMed PMID: WOS:A1988M822900027.

16.   Kunz-Schughart LA, Freyer JP, Hofstaedter F, Ebner R. The use of 3-D cultures for high-throughput screening: The multicellular spheroid model. Journal Of Biomolecular Screening. 2004;9(4):273-85. PubMed PMID: ISI:000221980300001.

17.   Hirschhaeuser F, Menne H, Dittfeld C, West J, Mueller-Klieser W, Kunz-Schughart LA. Multicellular tumor spheroids: An underestimated tool is catching up again. Journal of Biotechnology. 2010;148(1):3-15. PubMed PMID: ISI:000280028900002.

18.   Charoen KM, Fallica B, Colson YL, Zaman MH, Grinstaff MW. Embedded multicellular spheroids as a biomimetic 3D cancer model for evaluating drug and drug-device combinations. Biomaterials. 2014;35(7):2264-71. Epub 2013/12/24. doi: 10.1016/j.biomaterials.2013.11.038. PubMed PMID: 24360576.

19.   Wax A, Yang CH, Backman V, Badizadegan K, Boone CW, Dasari RR, et al. Cellular organization and substructure measured using angle-resolved low-coherence interferometry. Biophysical Journal. 2002;82(4):2256-64. PubMed PMID: WOS:000174932400051.

20.   Strey H, Peterson M, Sackmann E. Measurement of erythrocyte membrane elasticity by flicker eigenmode decomposition. Biophys J. 1995;69(2):478-88. PubMed PMID: 8527662; PubMed Central PMCID: PMC1236273.

21.   Brazhe NA, Brazhe AR, Pavlov AN, Erokhova LA, Yusipovich AI, Maksimov GV, et al. Unraveling cell processes: Interference imaging interwoven with data analysis. Journal of Biological Physics. 2006;32(3-4):191-208. PubMed PMID: ISI:000242325600002.

22.   Suissa M, Place C, Goillot E, Freyssingeas E. Internal dynamics of a living cell nucleus investigated by dynamic light scattering. Eur Phys J E Soft Matter. 2008;26(4):435-48. Epub 2009/02/21. doi: 10.1140/epje/i2007-10346-5. PubMed PMID: 19230214.

23.   Nan XL, Sims PA, Xie XS. Organelle tracking in a living cell with microsecond time resolution and nanometer spatial precision. Chemphyschem. 2008;9(5):707-12. PubMed PMID: ISI:000255082600007.

24.   Karnaky KJ, Garretson LT, Oneil RG. Video-Enhanced Microscopy of Organelle Movement in an Intact Epithelium. Journal of Morphology. 1992;213(1):21-31. PubMed PMID: ISI:A1992JF67100003.

25.   Trinczek B, Ebneth A, Mandelkow E. Tau regulates the attachment/detachment but not the speed of motors in microtubule-dependent transport of single vesicles and organelles. Journal of Cell Science. 1999;112(14):2355-67. PubMed PMID: ISI:000081815300009.

26.   Berne BJ, Pecora R. Dynamic light scattering with applications to chemistry, biology, and physics. New York: Wiley; 1976.

27.   Suissa M, Place C, Goillot E, Freyssingeas E. Internal dynamics of a living cell nucleus investigated by dynamic light scattering. European Physical Journal E. 2008;26(4):435-48. PubMed PMID: ISI:000259821100013.

28.   Chen SH, Hallett FR. DETERMINATION OF MOTILE BEHAVIOR OF PROKARYOTIC AND EUKARYOTIC CELLS BY QUASI-ELASTIC LIGHT-SCATTERING. Quarterly Reviews of Biophysics. 1982;15(1):131-222. PubMed PMID: WOS:A1982NQ53100002.

29.   Pine DJ, Weitz DA, Chaikin PM, Herbolzheimer E. DIFFUSING-WAVE SPECTROSCOPY. Physical Review Letters. 1988;60(12):1134-7. doi: 10.1103/PhysRevLett.60.1134. PubMed PMID: WOS:A1988M522600009.

30.   Pine DJ, Weitz DA, Zhu JX, Herbolzheimer E. DIFFUSING-WAVE SPECTROSCOPY - DYNAMIC LIGHT-SCATTERING IN THE MULTIPLE-SCATTERING LIMIT. Journal De Physique. 1990;51(18):2101-27. doi: 10.1051/jphys:0199000510180210100. PubMed PMID: WOS:A1990DU78100009.

31.   Weitz DA, Zhu JX, Durian DJ, Gang H, Pine DJ. DIFFUSING-WAVE SPECTROSCOPY - THE TECHNIQUE AND SOME APPLICATIONS. Physica Scripta. 1993;T49B:610-21. doi: 10.1088/0031-8949/1993/t49b/040. PubMed PMID: WOS:A1993MM84500040.

32.   Wild JJ, Reid JM. Application of echo-ranging techniques to the determination of structure of biological tissues. Science. 1952;115(2983):226-30.

33.   Hounsfield GN. Computerized transverse axial scanning (tomography): Part 1. Description of system. The British journal of radiology. 1973;46(552):1016-22.

34.   Damadian R, Minkoff L, Goldsmith M, Stanford M, Koutcher J. Field Focusing Nuclear Magnetic Resonance (FONAR): Visualization of a Tumor in a Live Animal. Science. 1976;194(4272):1430-432.

35.   Minsky M, inventorMicroscopy Aparatus. USA 1957.

36.   Sheppard CJR, Choudhury A. IMAGE-FORMATION IN SCANNING MICROSCOPE. Optica Acta. 1977;24(10):1051-73. PubMed PMID: WOS:A1977DW22600005.

37.   Brakenhoff GJ, Blom P, Barends P. CONFOCAL SCANNING LIGHT-MICROSCOPY WITH HIGH APERTURE IMMERSION LENSES. Journal of Microscopy-Oxford. 1979;117(NOV):219-32. PubMed PMID: WOS:A1979HS23900004.

38.   Kruger RA, Liu PY, Fang YR, Appledorn CR. PHOTOACOUSTIC ULTRASOUND (PAUS) - RECONSTRUCTION TOMOGRAPHY. Medical Physics. 1995;22(10):1605-9. doi: 10.1118/1.597429. PubMed PMID: WOS:A1995TA81700005.

39.   Mandelis A. THEORY OF PHOTOTHERMAL WAVE DIFFRACTION TOMOGRAPHY VIA SPATIAL LAPLACE SPECTRAL DECOMPOSITION. Journal of Physics a-Mathematical and General. 1991;24(11):2485-505. doi: 10.1088/0305-4470/24/11/016. PubMed PMID: WOS:A1991FR40600016.

40.   Beenen A, Spanner G, Niesser R. Photoacoustic Depth-Resolved Analysis of Tissue Models. Applied Spectroscopy. 1997;51(1):51-7. Epub 57.

41.   Maslov K, Zhang HF, Hu S, Wang LV, editors. Optical-resolution confocal photoacoustic microscopy - art. no. 68561I. 9th Conference on Biomedical Thermoacoustics, Optoacoustics and Acousto-optics; 2008 2008 Jan 20-23; San Jose, CA2008.

42.   U-Thainual P, Kim D-H. Comparison between optical-resolution photoacoustic microscopy and confocal laser scanning microscopy for turbid sample imaging. Journal of Biomedical Optics. 2015;20(12). doi: 10.1117/1.jbo.20.12.121202. PubMed PMID: WOS:000368440300003.

43.   Zhou Y, Yao J, Wang LV. Tutorial on photoacoustic tomography. Journal of biomedical optics. 2016;21(6):61007-. doi: 10.1117/1.jbo.21.6.061007. PubMed PMID: MEDLINE:27086868.

44.   Stein EW, Maslov K, Wang LV. Noninvasive, in vivo imaging of blood-oxygenation dynamics within the mouse brain using photoacoustic microscopy. Journal of Biomedical Optics. 2009;14(2). doi: 10.1117/1.3095799. PubMed PMID: WOS:000266868500002.

45.   Raes F, Sobilo J, Le Mee M, Retif S, Natkunarajah S, Lerondel S, et al. High Resolution Ultrasound and Photoacoustic Imaging of Orthotopic Lung Cancer in Mice: New Perspectives for Onco-Pharmacology. Plos One. 2016;11(4). doi: 10.1371/journal.pone.0153532. PubMed PMID: WOS:000373900700078.

46.   Zhang M, Kim HS, Jin T, Yi A, Moon WK. Ultrasound-guided photoacoustic imaging for the selective detection of EGFR-expressing breast cancer and lymph node metastases. Biomedical Optics Express. 2016;7(5):1920-31. doi: 10.1364/boe.7.001920. PubMed PMID: WOS:000374745200023.

47.   Leahy M, Thompson K, Zafar H, Alexandrov S, Foley M, O'Flatharta C, et al. Functional imaging for regenerative medicine. Stem Cell Research & Therapy. 2016;7. doi: 10.1186/s13287-016-0315-2. PubMed PMID: WOS:000374645800001.

48.   Youngquist RC, Carr S, Davies DEN. OPTICAL COHERENCE-DOMAIN REFLECTOMETRY - A NEW OPTICAL EVALUATION TECHNIQUE. Optics Letters. 1987;12(3):158-60. doi: 10.1364/ol.12.000158. PubMed PMID: WOS:A1987G161000006.

49.   Jones R, Hyde SCW, Lynn MJ, Barry NP, Dainty JC, French PMW, et al. Holographic storage and high background imaging using photorefractive multiple quantum wells. Applied Physics Letters. 1996;69(13):1837-9. doi: 10.1063/1.117450. PubMed PMID: WOS:A1996VH79500006.

50.   Yu P, Mustata M, Turek JJ, French PMW, Melloch MR, Nolte DD. Holographic optical coherence imaging of tumor spheroids. Applied Physics Letters. 2003;83(3):575-7. doi: Doi 10.1063/1.1594830. PubMed PMID: ISI:000184186700057.

51.   Yu P, Mustata M, Peng LL, Turek JJ, Melloch MR, French PMW, et al. Holographic optical coherence imaging of rat osteogenic sarcoma tumor spheroids. Applied Optics. 2004;43(25):4862-73. doi: 10.1364/ao.43.004862. PubMed PMID: WOS:000223663300011.

52.	Jeong K, Peng LL, Nolte DD, Melloch MR. Fourier-domain holography in photorefractive quantum-well films. Applied Optics. 2004;43(19):3802-11. doi: 10.1364/ao.43.003802. PubMed PMID: WOS:000222427300004.

53.	Jeong K, Peng LL, Turek JJ, Melloch MR, Nolte DD. Fourier-domain holographic optical coherence imaging of tumor spheroids and mouse eye. Applied Optics. 2005;44(10):1798-805. doi: 10.1364/ao.44.001798. PubMed PMID: WOS:000228036600005.

54.	Jeong K, Turek JJ, Nolte DD. Fourier-domain digital holographic optical coherence imaging of living tissue. Appl Opt. 2007;46(22):4999-5008. Epub 2007/08/07. PubMed PMID: 17676107.

55.	Hyde SCW, Dept. of Phys. ICoS, Technol. & Med., London, UK, Jones R, Barry NP, Dainty JC, French PMW, et al. Depth-resolved holography through turbid media using photorefraction. Selected Topics in Quantum Electronics, IEEE Journal of. 1996;2(4):965-75. doi: 10.1109/2944.577323.

56.	Popescu G, Dogariu A. Dynamic light scattering in localized coherence volumes. Optics Letters. 2001;26:551-3. doi: doi:10.1364/OL.26.000551.

57.	Wax A, Yang C, Dasari RR, Feld MS. Path-length-resolved dynamic light scattering: modeling the transition from single to diffusive scattering. Appl Opt. 2001;40(24):4222-7. Epub 2008/03/25. PubMed PMID: 18360459.

58.	Boas DA, Bizheva KK, Siegel AM. Using dynamic low-coherence interferometry to image Brownian motion within highly scattering media. Opt Lett. 1998;23(5):319-21. Epub 2007/12/18. PubMed PMID: 18084498.

59.	Jüptner USW. Direct recording of holograms by a CCD target and numerical reconstruction. Applied Optics. 1994;33(2):179-81. doi: doi:10.1364/AO.33.000179.

60.	Swanson EA, Huang D, Hee MR, Fujimoto JG, Lin CP, Puliafito CA. High-speed optical coherence domain reflectometry. Opt Lett. 1992;17:151.

61.	Merrill D, An R, Turek J, Nolte D, editors. Role of cellular adhesions in tissue dynamics spectroscopy. SPIE 8942, Dynamics and Fluctuations in Biomedical Photonics XI; 2014.

62.	Nolte DD, An R, Turek J, Jeong K. Tissue dynamics spectroscopy for phenotypic profiling of drug effects in three-dimensional culture. Biomed Opt Express. 2012;3(11):2825-41. doi: 10.1364/boe.3.002825. PubMed PMID: 23162721; PubMed Central PMCID: PMC3493238.

63.	Evans J, Gratzer W, Mohandas N, Parker K, Sleep J. Fluctuations of the Red Blood Cell Membrane: Relation to Mechanical Properties and Lack of ATP Dependence. Biophys J. 2008;94(10):4134-44. doi: 10.1529/biophysj.107.117952. PubMed PMID: 18234829; PubMed Central PMCID: PMC2367166.

64.	Nan X, Sims PA, Xie XS. Organelle tracking in a living cell with microsecond time resolution and nanometer spatial precision. Chem Phys Chem. 2008;9:707-12.

65.	Nolte DD, An R, Turek J, Jeong K. Tissue dynamics spectroscopy for phenotypic profiling of drug effects in three-dimensional culture. Biomedical Optics Express. 2012;3(11):2825-41. PubMed PMID: WOS:000310644700014.

66.	Choquet D, Felsenfeld DP, Sheetz MP. Extracellular Matrix Rigidity Causes Strengthening of Integrin–Cytoskeleton Linkages. Cell. 1997;88(1):39-48. doi: 10.1016/S0092-8674(00)81856-5.

67.   Khatiwala CB, Peyton SR, Putnam AJ. Intrinsic mechanical properties of the extracellular matrix affect the behavior of pre-osteoblastic MC3T3-E1 cells. American Journal of Physiology - Cell Physiology. 2006;290(6):C1640-C50. doi: 10.1152/ajpcell.00455.2005.

68.   Cukierman E, Pankov R, Stevens DR, Yamada KM. Taking cell-matrix adhesions to the third dimension. Science. 2001;294(5547):1708-12. Epub 2001/11/27. doi: 10.1126/science.1064829. PubMed PMID: 11721053.

69.   Chen CS, Mrksich M, Huang S, Whitesides GM, Ingber DE. Geometric control of cell life and death. Science. 1997;276(5317):1425-8. PubMed PMID: ISI:A1997XB53300053.

70.   Lark AL, Livasy CA, Calvo B, Caskey L, Moore DT, Yang X, et al. Overexpression of Focal Adhesion Kinase in Primary Colorectal Carcinomas and Colorectal Liver Metastases. Clin Cancer Res. 2003;9(1):215-22.

71.   Haier J, Nasralla M, Nicolson GL. Different adhesion properties of highly and poorly metastatic HT-29 colon carcinoma cells with extracellular matrix components: role of integrin expression and cytoskeletal components. Br J Cancer. 1999;80(12):1867-74. Epub 1999/09/02. doi: 10.1038/sj.bjc.6690614. PubMed PMID: 10471033; PubMed Central PMCID: PMCPmc2374274.

72.   Madan R, Smolkin MB, Cocker R, Fayyad R, Oktay MH. Focal adhesion proteins as markers of malignant transformation and prognostic indicators in breast carcinoma. Human Pathology. 2006;37(1):9–15.

73.   Aponte M, Jiang W, Lakkis M, Li M-J, Edwards D, Albitar L, et al. Activation of Platelet-Activating Factor Receptor and Pleiotropic Effects on Tyrosine Phospho-EGFR/Src/FAK/Paxillin in Ovarian Cancer. Cancer Res. 2008;68(14):5839-48. doi: 10.1158/0008-5472.CAN-07-5771.

74.   Carellia S, Zadraa G, Vairac V, Fallenic M, Bottiglieric L, Nosottie M, et al. Up-regulation of focal adhesion kinase in non-small cell lung cancer. Lung Cancer. 2006;53(3):263–71.

75.   Chen YY, Wang ZX, Chang PA, Li JJ, Pan F, Yang L, et al. Knockdown of focal adhesion kinase reverses colon carcinoma multicellular resistance. Cancer Sci. 2009;100(9):1708-13. Epub 2009/06/09. doi: 10.1111/j.1349-7006.2009.01217.x. PubMed PMID: 19500106.

76.   Grantab R, Sivananthan S, Tannock IF. The penetration of anticancer drugs through tumor tissue as a function of cellular adhesion and packing density of tumor cells. Cancer Res. 2006;66(2):1033-9. Epub 2006/01/21. doi: 10.1158/0008-5472.can-05-3077. PubMed PMID: 16424039.

77.   Kunz-Schughart LA, Freyer JP, Hofstaedter F, Ebner R. The Use of 3-D Cultures for High-Throughput Screening: The Multicellular Spheroid Model. J Biomol Screen. 2004;9(4):273-85. doi: 10.1177/1087057104265040.

78.   Merrill D, An R, Turek J, Nolte DD. Digital holography of intracellular dynamics to probe tissue physiology. Applied Optics. 2015;54(1):A89-97. Epub 2015/05/15. doi: 10.1364/ao.54.000a89. PubMed PMID: 25967027; PubMed Central PMCID: PMCPMC4668827.

79.   Trainer DL, Kline T, McCabe FL, Faucette LF, Feild J, Chaikin M, et al. Biological characterization and oncogene expression in human colorectal carcinoma cell lines. Int J Cancer. 1988;41(2):287-96. Epub 1988/02/15. PubMed PMID: 3338874.

80.   Deer EL, Gonzalez-Hernandez J, Coursen JD, Shea JE, Ngatia J, Scaife CL, et al. Phenotype and Genotype of Pancreatic Cancer Cell Lines. Pancreas. 2010;39(4):425-35. doi: 10.1097/MPA.0b013e3181c15963. PubMed PMID: 20418756; PubMed Central PMCID: PMC2860631.

81.   Cohen E, Ophir I, Shaul YB. Induced differentiation in HT29, a human colon adenocarcinoma cell line. J Cell Sci. 1999.

82.   Ujihara Y, Miyazaki H, Wada S. Morphological study of fibroblasts treated with cytochalasin D and colchicine using a confocal laser scanning microscopy. J Physiol Sci. 2008;58(7):499-506. Epub 2008/10/22. doi: 10.2170/physiolsci.RP007708. PubMed PMID: 18928641.

83.   Society AC. Cancer Facts and Figures 20132013 June 2014. Available from: http://www.cancer.org/acs/groups/content/@epidemiologysurveilance/documents/document/acspc-036845.pdf.

84.   Boylan KLM, Skubitz KM, Skubitz APN. Subgroups of Ovarian Carinoma: Identification Using Differential Gene Expression - Springer. In: Hayat MA, editor. Methods of Cancer Diagnosis, Therapy and Prognosis. 6: Springer Science and Business Media; 2010.

85.   Boisen MM, Lesnock JL, Richard SD, Beriwal S, Kelley JL, Zorn KK, et al. Second-line Intraperitoneal Platinum-based Therapy Leads to an Increase in Second-line Progression-free Survival for Epithelial Ovarian Cancer. International Journal of Gynecological Cancer. 2016;26(4):626-31. doi: 10.1097/igc.0000000000000667. PubMed PMID: WOS:000377146600005.

86.   Petrillo M, De Iaco P, Cianci S, Perrone M, Costantini B, Ronsini C, et al. Long-Term Survival for Platinum-Sensitive Recurrent Ovarian Cancer Patients Treated with Secondary Cytoreductive Surgery Plus Hyperthermic Intraperitoneal Chemotherapy (HIPEC). Annals of Surgical Oncology. 2016;23(5):1660-5. doi: 10.1245/s10434-015-5050-x. PubMed PMID: WOS:000373311600039.

87.   Kornblith P, Wells A, Gabrin MJ, Piwowar J, Chattopadhyay A, George LD, et al. In vitro responses of ovarian cancers to platinums and taxanes. Anticancer Res. 2003;23(1B):543-8. Epub 2003/04/12. PubMed PMID: 12680143.

88.   Andreotti PE, Cree IA, Kurbacher CM, Hartmann DM, Linder D, Harel G, et al. Chemosensitivity testing of human tumors using a microplate adenosine triphosphate luminescence assay: clinical correlation for cisplatin resistance of ovarian carcinoma. Cancer Res. 1995;55(22):5276-82. Epub 1995/11/15. PubMed PMID: 7585588.

89.   Neubauer H, Stefanova M, Solomayer E, Meisner C, Zwirner M, Wallwiener D, et al. Predicting resistance to platinum-containing chemotherapy with the ATP tumor chemosensitivity assay in primary ovarian cancer. Anticancer Res. 2008;28(2A):949-55. Epub 2008/05/30. PubMed PMID: 18507041.

90.   Markman M. Counterpoint: chemosensitivity assays for recurrent ovarian cancer. J Natl Compr Canc Netw. 2011;9(1):121-4. Epub 2011/01/15. PubMed PMID: 21233248.

91. Herzog TJ, Krivak TC, Fader AN, Coleman RL. Chemosensitivity testing with ChemoFx and overall survival in primary ovarian cancer. Am J Obstet Gynecol. 2010;203(1):68 e1-6. Epub 2010/03/17. doi: 10.1016/j.ajog.2010.01.059. PubMed PMID: 20227055.

92. Cree IA. Chemosensitivity and chemoresistance testing in ovarian cancer. Curr Opin Obstet Gynecol. 2009;21(1):39-43. Epub 2009/01/07. doi: 10.1097/GCO.0b013e32832210ff. PubMed PMID: 19125002.

93. Cody NAL, Zietarska M, Filali-Mouhim A, Provencher DM, Mes-Masson AM, Tonin PN. Influence of monolayer, spheroid, and tumor growth conditions on chromosome 3 gene expression in tumorigenic epithelial ovarian cancer cell lines. BMC medical genomics. 2008;1:34. Epub 2008/08/09. doi: 10.1186/1755-8794-1-34. PubMed PMID: ISI:000272683900001; PubMed Central PMCID: PMC2519080.

94. Chang TT, Hughes-Fulford M. Monolayer and Spheroid Culture of Human Liver Hepatocellular Carcinoma Cell Line Cells Demonstrate Distinct Global Gene Expression Patterns and Functional Phenotypes. Tissue Engineering Part A. 2009;15(3):559-67. PubMed PMID: ISI:000263913900011.

95. Gaedtke L, Thoenes L, Culmsee C, Mayer B, Wagner E. Proteomic analysis reveals differences in protein expression in spheroid versus monolayer cultures of low-passage colon carcinoma cells. Journal of Proteome Research. 2007;6(11):4111-8. PubMed PMID: ISI:000250718700006.

96. Barbone D, Yang TM, Morgan JR, Gaudino G, Broaddus VC. Mammalian target of rapamycin contributes to the acquired apoptotic resistance of human mesothelioma multicellular spheroids. Journal Of Biological Chemistry. 2008;283(19):13021-30. PubMed PMID: ISI:000255499800039.

97. Howes AL, Chiang GG, Lang ES, Ho CB, Powis G, Vuori K, et al. The phosphatidylinositol 3-kinase inhibitor, PX-866, is a potent inhibitor of cancer cell motility and growth in three-dimensional cultures. Molecular Cancer Therapeutics. 2007;6(9):2505-14. PubMed PMID: ISI:000249716200015.

98. Frankel A, Man S, Elliott P, Adams J, Kerbel RS. Lack of multicellular drug resistance observed in human ovarian and prostate carcinoma treated with the proteasome inhibitor PS-341. Clinical Cancer Research. 2000;6(9):3719-28. PubMed PMID: ISI:000089224600049.

99. Poland J, Sinha P, Siegert A, Schnolzer M, Korf U, Hauptmann S. Comparison of protein expression profiles between monolayer and spheroid cell culture of HT-29 cells revealed fragmentation of CK18 in three-dimensional cell culture. Electrophoresis. 2002;23(7-8):1174-84. PubMed PMID: ISI:000175436200026.

100. Wang N, Butler JP, Ingber DE. Mechanotransduction Across The Cell-Surface And Through The Cytoskeleton. Science. 1993;260(5111):1124-7. PubMed PMID: ISI:A1993LC94200029.

101. Ingber DE. Cellular mechanotransduction: putting all the pieces together again. Faseb Journal. 2006;20(7):811-27. PubMed PMID: ISI:000240157700003.

102. Serebriiskii I, Castello-Cros R, Lamb A, Golemis EA, Cukierman E. Fibroblast-derived 3D matrix differentially regulates the growth and drug-responsiveness of human cancer cells. Matrix Biology. 2008;27(6):573-85. PubMed PMID: ISI:000259028800008.

103.   David L, Dulong V, Le Cerf D, Cazin L, Lamacz M, Vannier JP. Hyaluronan hydrogel: An appropriate three-dimensional model for evaluation of anticancer drug sensitivity. Acta Biomaterialia. 2008;4(2):256-63. PubMed PMID: ISI:000254069200005.

104.   Frankel A, Buckman R, Kerbel RS. Abrogation of taxol-induced G(2)-M arrest and apoptosis in human ovarian cancer cells grown as multicellular tumor spheroids. Cancer Res. 1997;57(12):2388-93. PubMed PMID: ISI:A1997XD80000017.

105.   Hazlehurst LA, Landowski TH, Dalton WS. Role of the tumor microenvironment in mediating de novo resistance to drugs and physiological mediators of cell death. Oncogene. 2003;22(47):7396-402. PubMed PMID: ISI:000186112500012.

106.   Keller PJ, Pampaloni F, Stelzer EHK. Life sciences require the third dimension. Current Opinion In Cell Biology. 2006;18(1):117-24. PubMed PMID: ISI:000235242700018.

107.   Pampaloni F, Reynaud EG, Stelzer EHK. The third dimension bridges the gap between cell culture and live tissue. Nature Reviews Molecular Cell Biology. 2007;8(10):839-45. PubMed PMID: ISI:000249642900016.

108.   Dardousis K, Voolstra C, Roengvoraphoj M, Sekandarzad A, Mesghenna S, Winkler J, et al. Identification of differentially expressed genes involved in the formation of multicellular tumor spheroids by HT-29 colon carcinoma cells. Molecular Therapy. 2007;15(1):94-102. PubMed PMID: ISI:000244404700019.

109.   Friedrich J, Seidel C, Ebner R, Kunz-Schughart LA. Spheroid-based drug screen: considerations and practical approach. Nature Protocols. 2009;4(3):309-24. PubMed PMID: ISI:000265782000004.

110.   Tavassoli FA, Cook CB, Pestaner JP. A Comparison of 2 Comercially Available In Vitro Chemosensitivity Assays. Oncology. 1995;52(5):413-8. PubMed PMID: WOS:A1995RR39700012.

111.   Jeong K, Turek JJ, Nolte DD. Speckle fluctuation spectroscopy of intracellular motion in living tissue using coherence-domain digital holography. Journal of Biomedical Optics. 2010;15(3):030514. PubMed PMID: ISI:000280642900010.

112.   Nolte DD, An R, Turek J, Jeong K. Holographic tissue dynamics spectroscopy. Journal of Biomedical Optics. 2011;16(8):087004-13. doi: 10.1117/1.3615970. PubMed PMID: WOS:000295441500031.

113.   Nolte DD, An R, Turek J, Jeong K. Tissue Dynamics Spectroscopy for Three-Dimensional Tissue-Based Drug Screening. Jala. 2011;16(6):431-42. doi: 10.1016/j.jala.2011.05.002. PubMed PMID: WOS:000297189800005.

114.   Salvador M, Prauzner J, Kober S, Meerholz K, Turek JJ, Jeong K, et al. Three-dimensional holographic imaging of living tissue using a highly sensitive photorefractive polymer device. Optics Express. 2009;17(14):11834-49. PubMed PMID: ISI:000267761200062.

115.   Jeong K, Turek JJ, Melloch MR, Nolte DD. Multiple-scattering speckle in holographic optical coherence imaging. Appl Phys B-Lasers O. 2009;95(3):617-25. doi: Doi 10.1007/S00340-009-3561-5. PubMed PMID: ISI:000266073000034.

116.   Salvador M, Prauzner J, Kober S, Meerholz K, Jeong K, Nolte DD. Depth-resolved holographic optical coherence imaging using a high-sensitivity photorefractive polymer device. Appl Phys Lett. 2008;93(23). PubMed PMID: ISI:000261699700014.

117.   Jeong K, Turek JJ, Nolte DD. Imaging Motility Contrast in Digital Holography of Tissue Response to Cytoskeletal Anti-cancer Drugs,. Optics Express. 2007;**15**:14057-64.

118.   Jeong K, Turek JJ, Nolte DD. Fourier-Domain Digital Holographic Optical Coherence Imaging of Living Tissue. Appl Opt. 2007;46:4999-5008.

119.   Anglesio MS, Wiegand KC, Melnyk N, Chow C, Salamanca C, Prentice LM, et al. Type-Specific Cell Line Models for Type-Specific Ovarian Cancer Research. PLoS ONE. 2013;8(9):1-13.

120.   Auersperg N. The origin of ovarian cancers--hypotheses and controversies. Front Biosci (Schol Ed). 2013;5:709-19. Epub 2013/01/02. PubMed PMID: 23277080.

121.   Köbel M, Kalloger SE, Boyd N, McKinney S, Mehl E, Palmer C, et al. Ovarian Carcinoma Subtypes Are Different Diseases: Implications for Biomarker Studies. PLoS Medicine. 2008;5(12). PubMed PMID: 35907690.

122.   Crum CP, Drapkin R, Kindelberger D, Medeiros F, Miron A, Lee Y. Lessons from BRCA: The Tubal Fimbria Emerges as an Origin for Pelvic Serous Cancer. 2007. doi: 10.3121/cmr.2007.702.

123.   Murdoch WJ, Martinchick JF. Oxidative Damage to DNA of Ovarian Surface Epithelial Cells Affected by Ovulation: Carcinogenic Implication and Chemoprevention. 2004.

124.   Gadducci A, Cosio S, Gargini A, Genazzani AR. Sex-steroid hormones, gonadotropin and ovarian carcinogenesis: a review of epidemiological and experimental data. Gynecol Endocrinol. 2004;19(4):216-28.

125.   Fleming JS, Beaugié CR, Haviv I, Chenevix-Trench G, Tan OL. Incessant ovulation, inflammation and epithelial ovarian carcinogenesis: revisiting old hypotheses. Mol Cell Endocrinol. 2006;247(1-2):4-21.

126.   Capen CC. Mechanisms of Hormone-Mediated Carcinogenesis of the Ovary. Toxicologic Pathology Jul/Aug2004 Supplement 2. 2004;32:1. doi: 10.1080/01926230490462075. PubMed PMID: 14264301.

127.   Trimble EL, Birrer MJ, Hoskins WJ, Marth C, Petryshyn R, Quinn M, et al. Current academic clinical trials in ovarian cancer: Gynecologic Cancer Intergroup and US National Cancer Institute Clinical Trials Planning Meeting, May 2009. Int J Gynecol Cancer. 2010;20(7):1290-8. Epub 2010/12/15. doi: 10.1111/IGC.0b013e3181ee1c01. PubMed PMID: 21151709; PubMed Central PMCID: PMC2998994.

128.   Nature. Integrated genomic analyses of ovarian carcinoma. Nature. 2011;474(7353):609-15. Epub 2011/07/02. doi: 10.1038/nature10166. PubMed PMID: 21720365; PubMed Central PMCID: PMC3163504.

129.   Ledermann JA, Marth C, Carey MS, Birrer M, Bowtell DD, Kaye S, et al. Role of molecular agents and targeted therapy in clinical trials for women with ovarian cancer. Int J Gynecol Cancer. 2011;21(4):763-70. Epub 2011/05/06. doi: 10.1097/IGC.0b013e31821b2669. PubMed PMID: 21543938.

130.   Behrens BC, Hamilton TC, Masuda H, Grotzinger KR, Whang-Peng J, Louie KG, et al. Characterization of a cis-diamminedichloroplatinum(II)-resistant human ovarian cancer cell line and its use in evaluation of platinum analogues. Cancer Res. 1987;47(2):414-8. Epub 1987/01/15. PubMed PMID: 3539322.

131.   A2780cis Cell Line human ovarian carcinoma | Sigma-Aldrich 2014. Available from:
http://www.sigmaaldrich.com/catalog/product/sigma/93112517?lang=en&region=US.
132.   Armstrong DK, Bundy B, Wenzel L, Huang HQ, Baergen R, Lele S, et al. Intraperitoneal cisplatin and paclitaxel in ovarian cancer. N Engl J Med. 2006;354(1):34-43. Epub 2006/01/06. doi: 10.1056/NEJMoa052985. PubMed PMID: 16394300.
133.   Klopp AH, Eifel PJ. Platinum-based chemotherapy for concurrent chemoradiation. Chemoradiotherapy for Cervical Cancer in 2010: Springer Science and Business Media, LLC; 2010.
134.   Wu C, Wangpaichitr M, Feun L, Kuo MT, Robles C, Lampidis T, et al. Overcoming cisplatin resistance by mTOR inhibitor in lung cancer. Molecular Cancer. 2005;4(1):25. doi: info:pmid/16033649.
135.   Burger AM, Double JA, Newell DR. Inhibition of telomerase activity by cisplatin in human testicular cancer cells. 1997;33(4):638–44.
136.   Platinum, Gold, and Other Metal Chemotherapeutic Agents. Lippard SJ, editor: American Chemical Society; 1983.
137.   Siddik ZH. Cisplatin: mode of cytotoxic action and molecular basis of resistance. Oncogene. 2003;22(47):7265-79. doi: doi:10.1038/sj.onc.1206933.
138.   Basu A, Krishnamurthy S. Cellular Responses to Cisplatin-Induced DNA Damage. Journal of Nucleic Acids. 2010;2010(2010). Epub 28 June 2010.
139.   Anderson K, Lawson KA, Simmons-Menchaca M, Sun L, Sanders BG, Kline K. Alpha-TEA plus cisplatin reduces human cisplatin-resistant ovarian cancer cell tumor burden and metastasis. Exp Biol Med. 2004;229(11):1169-76.
140.   Zhong H, De Marzo AM, Laughner E, Lim M, Hilton DA, Zagzag D, et al. Overexpression of hypoxia-inducible factor 1alpha in common human cancers and their metastases. Cancer Res. 1999;59(22):5830-5. Epub 1999/12/03. PubMed PMID: 10582706.
141.   Nolte D, An R, Turek J, Jeong K. Tissue dynamics spectroscopy for phenotypic profiling of drug effects in three-dimensional culture. Biomedical Optics Express. 2012;3(11):2825-41. PubMed PMID: WOS:000310644700014.
142.   Hansen JM, Coleman RL, Sood AK. Targeting the tumour microenvironment in ovarian cancer. European Journal of Cancer. 2016;56:131-43. doi: 10.1016/j.ejca.2015.12.016. PubMed PMID: WOS:000371778400017.
143.   Sung P-L, Jan Y-H, Lin S-C, Huang C-C, Lin H, Wen K-C, et al. Periostin in tumor microenvironment is associated with poor prognosis and platinum resistance in epithelial ovarian carcinoma. Oncotarget. 2016;7(4):4036-47. PubMed PMID: WOS:000369952400030.
144.   Wang S, Blois A, El Rayes T, Liu JF, Hirsch MS, Gravdal K, et al. Development of a prosaposin-derived therapeutic cyclic peptide that targets ovarian cancer via the tumor microenvironment. Science Translational Medicine. 2016;8(329). doi: 10.1126/scitranslmed.aad5653. PubMed PMID: WOS:000372079400006.
145.   Knowles M, Selby P. Introduction to the Cellular and Molecular Biology of Cancer. 4th edition ed: Oxford University Press; 2005.

146.   Acar O, Ozkurt E, Demir G, Sarac H, Alkan C, Esen T, et al. Determining the origin of synchronous multifocal bladder cancer by exome sequencing. Bmc Cancer. 2015;15. doi: 10.1186/s12885-015-1859-8. PubMed PMID: WOS:000365270800002.

147.   Pradeep S, Kim SW, Wu SY, Nishimura M, Chaluvally-Raghavan P, Miyake T, et al. Hematogenous Metastasis of Ovarian Cancer: Rethinking Mode of Spread. Cancer Cell.   2014;26(1):77-91.   doi: 10.1016/j.ccr.2014.05.002.   PubMed   PMID: WOS:000339305200013.

148.   Nieman KM, Kenny HA, Penicka CV, Ladanyi A, Buell-Gutbrod R, Zillhardt MR, et al. Adipocytes promote ovarian cancer metastasis and provide energy for rapid tumor growth. Nature Medicine. 2011;17(11):1498-U207. doi: 10.1038/nm.2492. PubMed PMID: WOS:000296779300042.

149.   Hill BT, Whelan RDH, Gibby EM, Sheer D, Hosking LK, Shellard SA, et al. ESTABLISHMENT AND CHARACTERIZATION OF 3 NEW HUMAN OVARIAN-CARCINOMA CELL-LINES AND INITIAL EVALUATION OF THEIR POTENTIAL IN EXPERIMENTAL CHEMOTHERAPY STUDIES. International Journal of Cancer. 1987;39(2):219-25.   doi: 10.1002/ijc.2910390216.   PubMed   PMID: WOS:A1987F979800015.

150.   Ogawa S, Lee TM, Kay AR, Tank DW. Brain magnetic resonance imaging with contrast dependent on blood oxygenation. Proc Natl Acad Sci U S A. 1990;87(24):9868.

151.   An R. Biodynamic imaging of living tissue. West Lafayette: Purdue University; 2014.

152.   Adiseshaiah PP, Clogston JD, McLeland CB, Rodriguez J, Potter TM, Neun B, et al. Synergistic combination therapy with nanoliposomal C6-ceramide and vinblastine is associated with autophagy dysfunction in hepatocarcinoma and colorectal cancer models. Cancer Let. 2013;337(2):254-65.

153.   Kang W, DiPaola RS, Vazquez A. Inference of synergy/antagonism between anticancer drugs from the pooled analysis of clinical trials. BMC Medical Research Methodology. 2013;13(77). Epub 12 June 2013.

154.   Cardoso AA, Jiang Y, Luo M, Reed AM, Shahda S, He Y, et al. APE1/Ref-1 regulates STAT3 transcriptional activity and APE1/Ref-1-STAT3 dual-targeting effectively inhibits pancreatic cancer cell survival. PLoS One. 2012;7(10):e47462. Epub 2012/10/25. doi: 10.1371/journal.pone.0047462. PubMed PMID: 23094050; PubMed Central PMCID: PMCPmc3477158.

APPENDICES

Appendix A   Biodynamic Study of Synergistic Effects in Pancreatic Tissue

Synergistic effects play a critical role in the viability of potential cancer treatments because they potentially increase the effectiveness of the treatment while limiting the ill effect to the patient. Several studies in recent years have investigated different synergies, including between different chemotherapeutic drugs [152, 153], between chemotherapeutic drugs and different cancer treatments, and between different cancer treatments [18].

The research group of Dr. Melissa Fishel at the Indiana School of Medicine looked at synergistic effect of redox disruption with STAT3 blockade as a dual-targeted therapy for treating pancreatic ductal adenocarcinoma (PDAC) [154]. They showed that STAT3 is regulated by the redox function of the APE1/Ref-1 endonuclease and that the redox inhibitor E3330 blocked DNA binding of STAT3. In cell culture assays, dual-targeted therapy using E3330 and the STAT selective inhibitor STATTIC synergized to inhibit growth and spread of PDAC cells with a 3-fold increase in inhibition over mono-therapies of either E3330 or STATTIC. However, because 2D cell cultures differ from 3D tissue in both genetic expression and cellular environment, testing of this novel dual-targeted therapy in 3D tissue models was needed. BDI is a natural response assay for testing combined STAT3/redox inhibition in 3D tissue.

Cell cultures: MIA PaCa-2 cells were from American Type Culture Collection (ATCC) Manassas, VA. Cells were cultured in DMEM at 37 °C in a humidified CO_2 incubator. All growth media contain 10% fetal calf serum (Atlanta Biologicals), penicillin (100 IU), and streptomycin (100 μg/mL).

Stat-inhibiting drugs: STATTIC and E3330 were provided by Dr. Mark Kelley, Indiana University School of Medicine.

Sample preparation and imaging: The preparation and imaging methods for both tumor spheroid and cell suspension samples was the same as described in CHAPTER 2, with the following deviation: for tumor spheroids, 550 frames were captured at 25 frames per second instead of 500 frames. This did not change the data analysis or workflow, however, as only 500 frames were used.

Sample rejection protocol: Experiments exhibited several failure modes that caused samples to be rejected from the analysis. Samples would lose coherence-gaiting due to fringe washout, or would shift position due to immobilization failure. These modes showed strong changes in MCI compared with successful experiments (see Figure A.1a-c). Some samples showed erratic jumps in NSD without loss of coherence or immobilization (See Figure A.1d-e). These modes were systematic failures that invalidated sample results. A few samples demonstrated an unusually strong response to STATTIC, either alone or in combination with E3330. These pathological cases were marked by a strong decrease in normalized standard deviation of the speckle intensity and by strong shifts in the tissue response spectrograms (See Figure A.1f-g). It was not possible *a priori* to determine when a sample would have a pathological response. The reason for such a response is unknown. These samples were not included in the combinatorial response calculations described below. An entire experiment was rejected when a majority of individual samples were rejected.
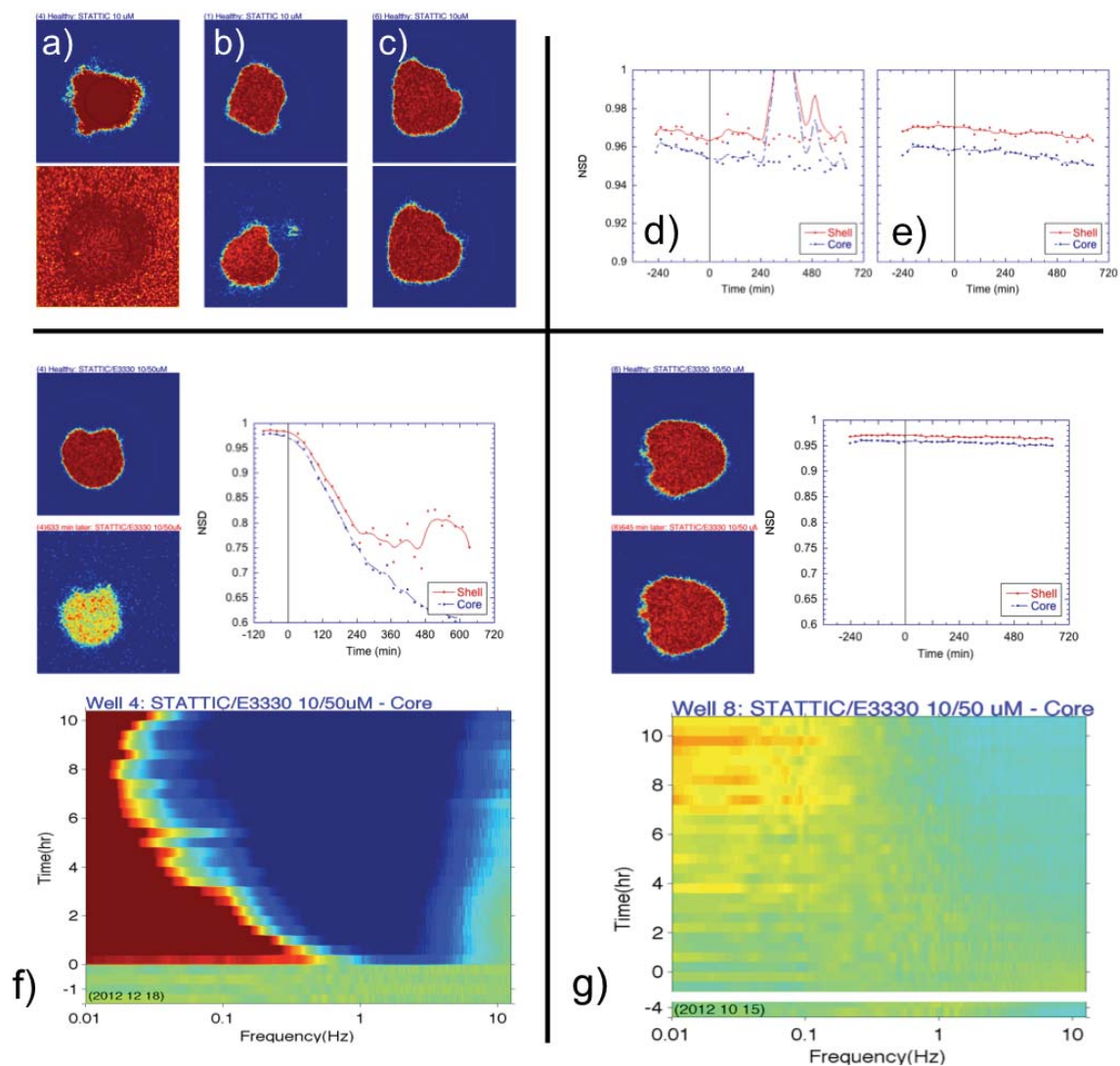
Figure A.1. Examples of accepted and rejected samples. Individual samples were rejected because of coherence-gate loss (a) or immobilization failure (b) after adding drug. Acceptable MCI behavior is shown in (c). Some samples showed normal acceptable MCI, but had erratic jumps in NSD (d). Acceptable NSD behavior is shown in (e). Some samples exhibited pathological response (f) marked by clear changes in sample motility contrast, large decrease in NSD, and abnormally large change in power spectral density (spectrogram). Non-pathological behavior is shown in (g).

Results: To study the combinatorial effects of kinase inhibitors on pancreatic cancer

PaCa-2, we used BDI to see how the STAT-inhibitor STATTIC and the APE1-inhibitor

E3330 combined produced a greater effect on PaCa-2 than the drugs separately. Drug

controls were applied separately and in combination and tumor response was compared

against negative controls (1.25 mM DMSO and growth medium). Individual sample

responses are shown in Figure A.2. The average tumor response to each control is shown
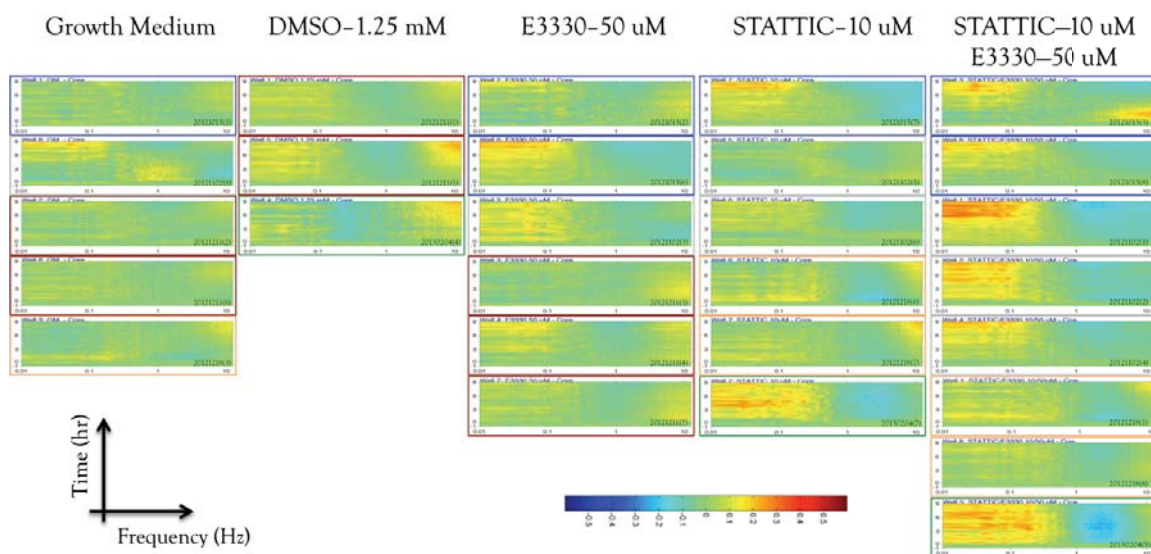
in Figure A.3.

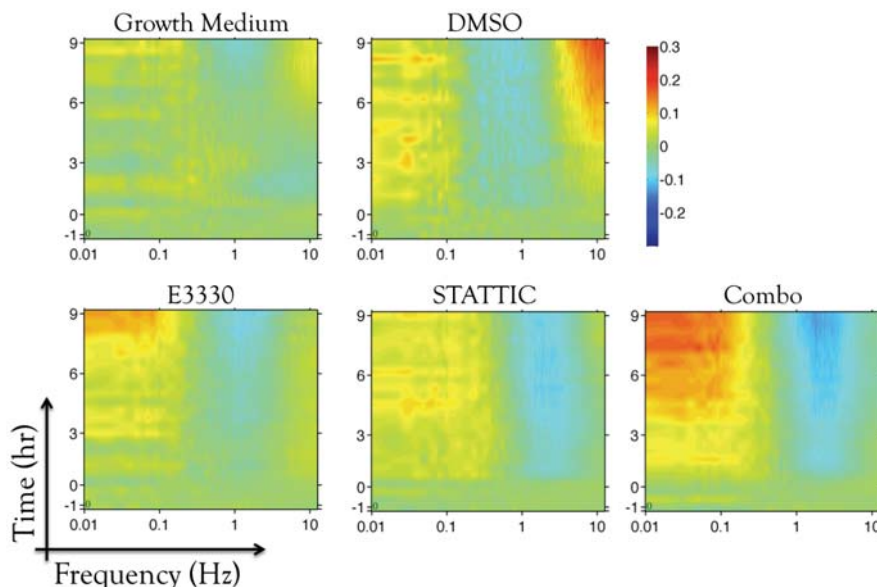Figure A.2. Individual samples response spectrograms.

Figure A.3. Combinatorial averaged spectrograms. Spectrograms show average PaCa-2 tumor response to the STAT-inhibitor drugs E3330, STATTIC, and their combination. Individual response spectrograms were calculated for each sample with the average negative control (DMSO) response of each data set subtracted from each sample in that set. Then the average response spectrogram over all data sets for each control was calculated.

There is a visible enhancement of motion up to 0.5 Hz due to the addition of E3330 and/or STATTIC. This enhancement is greater than any response to the DMSO in which both E3330 and STATTIC were dissolved. The average low-frequency enhancement was calculated beginning after 3.5 hours, which was the estimated half-max time of the response change. The results can be seen in Figure A.4.
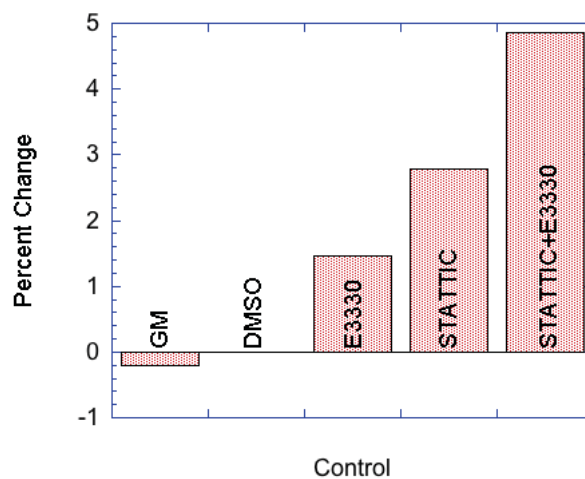
Figure A.4. Percent change in low-frequency tumor response relative to DMSO. Shows the average change in power spectral density between 0 and 9 hours after a drug was applied.

Discussion and Conclusion: Biodynamic imaging and analysis showed an

enhanced effect in the combination therapy relative to the individual therapies. However,

the measured enhancement was not more than the sum of the individual effects of

STATTIC and E3330, suggesting that the combination effects were additive and did not

have any particular synergy when applied to 3D culture models.

The cause of pathological response is unknown. Several samples from at least

two experimental sample groups exhibited an overwhelming sensitivity to applied

therapy. However, no experimental group showed pathological response in all samples

indicating that this was a biological effect and not an artifact of the BDI system, nor due

to operator error. Even more intriguing was the fact that pathological behavior was not

isolated to the combination therapies, but also occurred in samples that received the

mono-therapies. More systematic investigation is needed before the cause of this

hypersensitivity can be determined.

.

Appendix B   Assessing response to therapy for esophageal cancer patients using biodynamic imaging

Patient biopsies: Esophageal patient biopsies were obtained from Indiana University Hospital. Harvested tumors were placed in ice-cold media and were transported to John Turek's laboratory within 2 hours and prepared for imaging. Half the biopsy was immediately prepared while the other half was maintained at 4 °C for up to 36 hours before testing. Biopsies were sectioned using a razor blade to cut the tumor into pieces of approximately 1 mm^3 in volume. Pieces were affixed inside 96-well plates using a small drop of GLUture (Abbot Laboratories) and covered with agarose. Growth medium was added to each well. Experiments were performed immediately after plates were prepared.

Chemotherapy drugs: Cisplatin, carboplatin, fluorouracil (5-FU), and paclitaxel (taxol) were obtained from Selleck Chemicals. Dimethyl sulfoxide (DMSO) came from Sigma-Aldrich. Drugs were prepared to twice the desired concentration to allow for later mixing inside the sample well. Drug concentrations were as follows: 25 μM for cisplatin, carboplatin, and 5-FU; 10 μM for taxol. DMSO dissolved in growth medium was used as the negative control in all experiments. DMSO was selected since it is the carrier for the other drugs before being added to growth medium to improve solubility.

OCI sequence: A diagram and explanation of the OCI system is found in CHAPTER 1.5. OCI frames of each tumor section were captured in cycles every 40-48 minutes on average. Each capture sequence consisted of 15-45 seconds travel time to allow the system to transition between tumors, followed by frame capture: 10 background frames captured at 10 frames per second (fps) with the reference beam not zero-path matched, then 50 frames at 0.5 fps and 500 frames at 25 fps with the reference beam zero-path

matched. Tumor sections were observed for 6 cycles (4.8 hours) to allow the samples to stabilize. Then half of the growth medium (~150 µL) was removed from each well and replaced with a drug at twice the intended concentration to limit disturbing the sample. Tumors were then observed for a further 12 cycles (9.6 hours).

Results: Figure B.1 shows average patient response to the mono- and combination therapies for esophageal patients 1-6. Patients were designated as responsive or non-responsive to therapy based on average therapy response spectrogram. The response biomarkers were then clustered based on similarity within each population (**Error! Reference source not found.**Figure B.2).
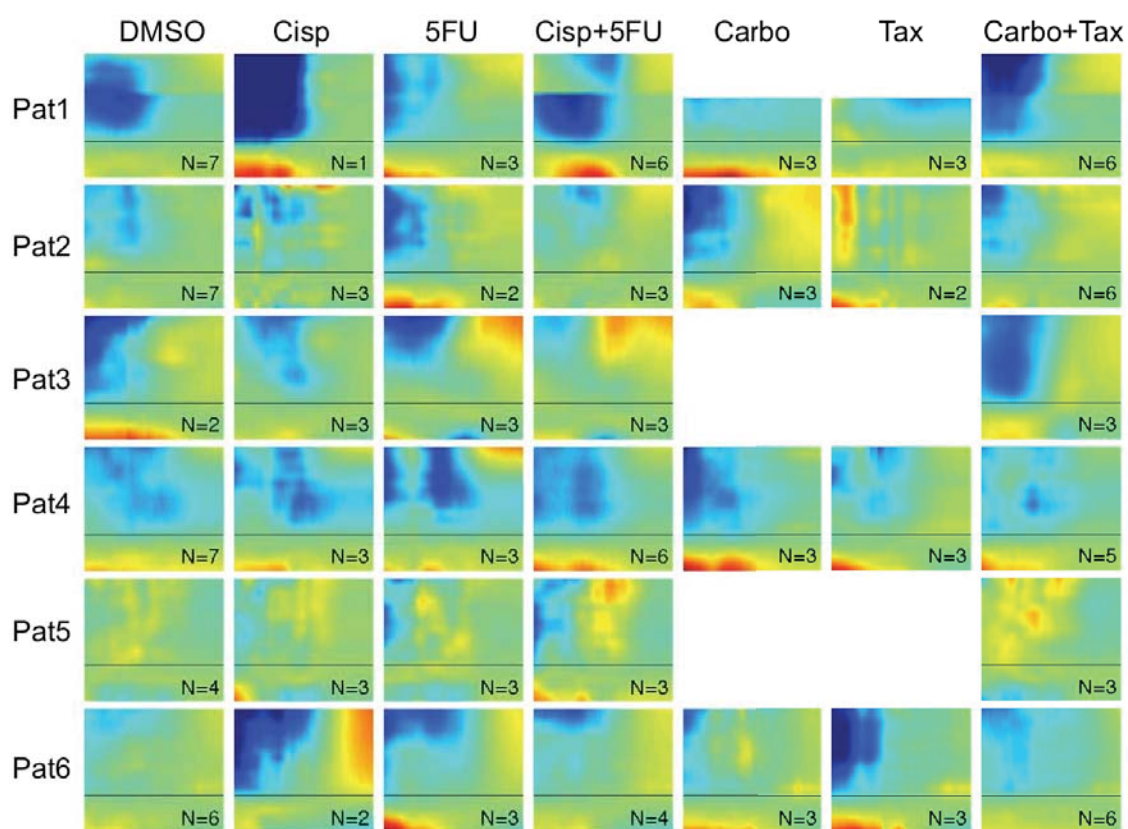

Figure B.1. Average response spectrograms for esophageal patients (#1-6). The number of replicates for each drug is indicated
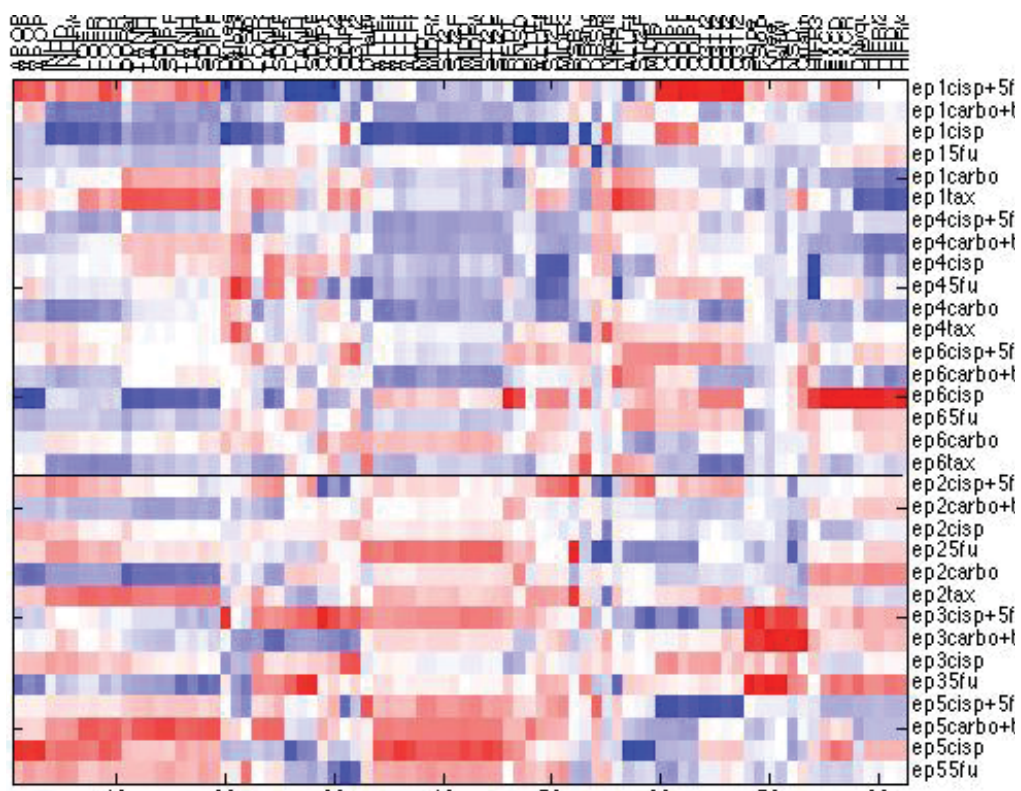
Figure B.2. Clustered feature vectors for the esophageal patients. (#1-6)

VITA

VITA

Daniel Merrill was born to Kenneth and Dinah Merrill in 1982 in Pueblo,

Colorado. He graduated from high school in 2000 as salutatorian of his graduating class.

Daniel completed a two-year proselytizing and service mission in São Paulo, Brazil for

the Church of Jesus Christ of Latter-day Saints in 2004, after which he began his

undergraduate studies at Brigham Young University in Provo, Utah. As an undergraduate,

he worked with Dr. Dallin Durfee to build a high-powered, stable laser system and to

develop a new laboratory course covering contemporary physics topics. Daniel

graduated with his bachelor of science in Physics in 2009, with a minor in Mathematics.

While an undergraduate, he also met and married his wife, Lilon, and they had two

daughters.

In August 2009, Daniel began graduate studies in Physics at Purdue University.

Early in his graduate career, Daniel was privileged to teach undergraduate courses

covering a wide range of topics, where he discovered he had a passion for teaching and

curriculum development. In 2013, he received Purdue's Committee for the Education of

Teaching Assistants (CETA) Teaching Award. Daniel joined Dr. David Nolte's research

group in August 2011 and began work related to biodynamic imaging. During his

research he has authored or co-authored five papers, and given numerous talks and poster

presentations. He and his wife have also given birth to three more daughters who have

filled his life with joy. Daniel will graduate with a combined M.S. and Ph.D. in 2016,

after which he will begin a teaching position at Indiana State University in the Autumn

PUBLICATIONS

PUBLICATIONS

1. Daniel Merrill, Hao Sun, Bakhtiyor Yakubov, Daniela Matei, John Turek and David Nolte, "Heterogeneous response to platinum in metastatic ovarian cancer detectable by biodynamic imaging," Poster Presentation, American Association for Cancer Research Annual Meeting, New Orleans, Louisiana. (4/18/2016)

2. Hao Sun, Daniel Merrill, John Turek, David Nolte, "Biodynamic profiling of three-dimensional tissue growth techniques," Proc. SPIE 9707, Dynamics and Fluctuations in Biomedical Photonics XIII, 97070S (17 March 2016)

3. Daniel Merrill, Ran An, Hao Sun, Bakhtiyor Yakubov, Daniela Matei, John Turek and David Nolte, "Intracellular Doppler Signatures of Platinum Sensitivity Captured by Biodynamic Profiling in Ovarian Xenografts," Nat. Sci. Rep. 6, 18821 (2016)

4. Daniel Merrill, Ran An, John Turek, and David Nolte, "Digital holography of intracellular dynamics to probe tissue physiology," Appl. Opt. 54, A89-A97 (2015).

5. Ran An, Daniel Merrill, Larisa Avramova, Jennifer Sturgis, Maria Tsiper, J. Paul Robinson, John Turek, and David D. Nolte, "Phenotypic Profiling of Raf Inhibitors and Mitochondrial Toxicity in 3D Tissue Using Biodynamic Imaging," J Biomol Screen. Apr 19(4), 526-37 (2014).

6. Daniel Merrill, Ran An, John Turek, and David Nolte, "Role of cellular adhesions in tissue dynamics spectroscopy," Proc. SPIE 8942, Dynamics and Fluctuations in Biomedical Photonics XI, 89420W (26 February 2014)